A MEASUREMENT OF THE NEUTRON ELECTRIC FORM FACTOR AT VERY LARGE MOMENTUM TRANSFER USING POLARIZED ELECTRONS SCATTERING FROM A POLARIZED HELIUM-3 TARGET

Aidan M. Kelleher
Alexandria, Virginia, USA

Bachelor of Arts, St. John's College, 1997
Master of Science, The College of William and Mary, 2003

A Dissertation presented to the Graduate Faculty
of the College of William and Mary in Candidacy for the Degree of
Doctor of Philosophy

Department of Physics

The College of William and Mary
February 2010

APPROVAL PAGE

This dissertation is submitted in partial fulfillment
of
the requirements for the degree of

Doctor of Philosophy

_____

Aidan M. Kelleher

Approved by the Committee, December 2009

_____

Committee Chair
Todd D. Averett
The College of William and Mary

_____

Professor Charles Perdrisat
The College of William and Mary

_____

Professor Carl E. Carlson
The College of William and Mary

_____

Professor David Armstrong
The College of William and Mary

_____

Doctor Bogdan Wojtsekhowski
Thomas Jefferson National Accelerator Facility

ABSTRACT

Knowledge of the electric and magnetic elastic form factors of the nucleon is essential for an understanding of nucleon structure. Of the form factors, the electric form factor of the neutron has been measured over the smallest range in Q^2 and with the lowest precision. Jefferson Lab experiment 02-013 used a novel new polarized ^{3}He target to nearly double the range of momentum transfer in which the neutron form factor has been studied and to measure it with much higher precision. Polarized electrons were scattered off this target, and both the scattered electron and neutron were detected. G_E^n was measured to be $0.0242 \pm 0.0020(\mathrm{stat}) \pm 0.0061(\mathrm{sys})$ and $0.0247 \pm 0.0029(\mathrm{stat}) \pm 0.0031(\mathrm{sys})$ at $Q^2 = 1.7 \text{ and } 2.5\ \mathrm{GeV}^2$, respectively.

TABLE OF CONTENTS

DEDICATION

I present this dissertation in memory of my grandfathers, Stanley Silun and Kenneth Kelleher.

ACKNOWLEDGMENTS

I could not have completed this document without the support, insight and guidance of my advisor, Prof. Todd D. Averett.

Special thanks are also due to the committee: Prof. David Armstrong, Prof. Carl Carlson, Prof. Charles Perdrisat and Dr. Bogdan Wojsetkowski. Without their insight on this document and their input over the years, this would have been impossible.

Nuclear physics is a collaborative field. There would be no data to write about without the help of the other members of the collaboration. First of all, the spokespeople: Dr. Bogdan Wojsetkowski, Prof. Gordon Cates, Prof. Nilanga Liyanage, Dr. Bodo Reitz, and Dr. Kathy McCormick. Nor would these data exist without the work of the students, post-docs, designers and technicians. In particular, I would like to thank Dr. Seamus Riordan, Dr. Robert Feuerbach, Brandon Craver, Jonathon Miller, Sergey Abrahamyan, Neil Thompson, Dr. Ameya Kolarkar, Alan Gavalya, Joyce Miller, Susan Esp and the rest of the E02-013 collaboration. Very special thanks are due to Sabine Fuchs and Ed Folts. Prof. Averett taught me many things about polarized ^{3}He targets; the rest I learned from Dr. Jian-Ping Chen and Jaideep Singh.

For most of my time in graduate school, I lived in Williamsburg, nearly 30 minutes from Jefferson Lab (barring traffic). In order to be available at all times during the experiment, I needed to base myself closer to the lab. John and Joann Gardner provided me with a bed, food, encouragement and the world's most comfortable chair.

One cannot finish graduate school without starting graduate school. For that I have several people to thank. First of all, I have to thank Prof. Marc Sher for guiding me through the pre-requisites and the application to graduate school. While applying to graduate school, I was working for Bill Royall at Royall & Company in Richmond, Virginia. Even though he had nothing to gain from it, Bill Royall allowed me to work a flexible schedule to take classes at Virginia Commonwealth. While taking pre-requisites at William & Mary, I worked for Prof. Roy Champion. I have to thank him, and Dr. Wendy Vogan, for taking me into the lab and introducing me to physics research.

My interest in physics was not created in a vacuum. I must give special thanks to my 7th and 8th grade science teacher, Mrs. Mary Pat Schlickenmaier. It was in her class that I first thought I would want to study physics, and it was through her encouragement and understanding that I thought it might be possible. Similarly, I must thank Mrs. Janet Marmura for her algebra class. Not only was I uninterested in math before her class, I wasn't any good at it. When I showed promise, she took the time to encourage that promise.

The only year in which I felt completely lost in high school was the year before I met Mr. Ronald Umbeck. As mathematics is the solid grounding for physics, my time with Mr. Umbeck was the foundation for my studies beyond his classroom. In addition to Algebra-II, Pre-Calculus, and Calculus, Mr. Umbeck was the coach for the "It's Academic" quiz-show team, which I did well on, and the competition math team, which I did not do well on. I must also thank Mr. Umbeck for not giving up on a student who almost never did his homework.

I did not pursue graduate school immediately after recieving my degree from St. John's College. In making my decision to return to school, I recalled specific encouraging conversations with Mr. Cordell Yee.

Graduate school is a marathon, and I was only able to complete it through the support of friends and family. In particular, old friends that treated me like family: Sean Flaherty, Tim Winslow, Damon and Meg Kovelsky, Taylor Hudnall, Jeannie Wilson and Cate Bottiglione. And, of course, family that are like friends: Mom and Dad, Megan, Karen and Michael.

From "touch" football games to intramural hockey to poker games and innumerable cups of coffee, I count myself lucky to share the graduate school experience with many wonderful people, including: Dan Pechkis, Vince Sulkosky, Brian Hahn, Pete Harris, Joe Katich, Stephen Coleman, Nate Phillips, Kelly Kluttz, and Bryan and Michelle Moffit.

When I decided to begin graduate school, I was encouraged by a friend that threw her support behind me so much that she entered graduate school herself. Special thanks are due to Laura Spess for years of friendship and encouragement.

Finally, no list of acknowledgements would be complete without thanking the friend that stood by me in every possible way. From telling me when I was a jerk, to coming with me to Japan, to watching my dog during my experiment, to telling me when I wasn't a jerk, I have come to depend entirely upon Anna Gardner.

LIST OF TABLES

LIST OF FIGURES

Figure Page

A MEASUREMENT OF THE NEUTRON ELECTRIC FORM FACTOR AT VERY LARGE MOMENTUM TRANSFER USING POLARIZED ELECTRONS SCATTERING FROM A POLARIZED HELIUM-3 TARGET

CHAPTER 1

Introduction

Jefferson Lab experiment 02-013 was a measurement of the neutron electric form factor at $Q^2 = 1.4,\ 1.7,\ 2.5,$ and $3.4\ \mathrm{GeV}^2$. The form factor was measured by scattering polarized electrons from a polarized ^{3}He target, and detecting both the scattered electron and neutron.

Knowledge of the neutron elastic electric form factor $G_E^n(Q^2)$ is essential for an understanding of nucleon structure. In simplest terms, the Fourier transform (in the Breit or "brick wall" frame) of G_E^n gives the charge density of the neutron. Recent measurements on the proton show that the ratio of the electric form factor for the proton G_E^p to the magnetic form factor G_M^p declines sharply as the square of the 4-momentum transfer, Q^2, increases. Therefore, the electric and magnetic form factors (of the proton) behave differently above $Q^2 \approx 1$ (GeV/c)^2. Presently, there is scant data on the behavior of G_E^n above this Q^2 value.

The form factors are key ingredients of tomographic images developed through the framework of Generalized Parton Distributions (GPDs). GPDs are universal functions that supersede both the well known parton distribution functions (observed via deep inelastic scattering) and form factors (observed via elastic electron scattering). GPDs allow

for the calculation of a wide class of hard exclusive reactions [1]. Form factor results are used to constrain the GPD models [2, 3]. Information about G_E^n is important to constrain the electric GPD E, which presently has a large uncertainty at momentum transfers where quark degrees of freedom become dominant [4].

1.1 Experimental Method

The historic method of measuring form factors is the Rosenbluth separation, which requires measuring the cross section for eN scattering at a number of different electron scattering angles for a given Q^2 [5]. The method is exceedingly difficult for the extraction of G_E^n, especially at high momentum transfer. The main complications are the dominance of the magnetic form factor, the lack of suitable free neutron targets, the large contributions from the proton from nuclear targets (such as ^{2}H and ^{3}He), and final state interactions. The uncertainty on results for G_E^n from elastic e-d scattering is large, and consistent with both $G_E^n = 0$ and the so-called Galster parametrization [6].

In 1984, Blankleider and Woloshyn suggested an alternative method of measuring the ratio of electric and magnetic form factors using ^{3}He for scattering polarized electrons off polarized neutrons [7]. In the last 20 years, a dozen experiments have used the double polarized techniques [5].

The double polarized spin asymmetry is dependent upon the ratio G_E^n/G_M^n via

$$A_{\rm phys} = \left[\sin\theta^* \cos\phi^* A_\perp + \cos\theta^* A_\parallel\right] hP_bP_t \tag{1.1}$$

where

$$A_\perp = -\frac{G_E^n}{G_M^n} \cdot \frac{2\sqrt{\tau(\tau+1)}\tan(\theta/2)}{(G_E^n/G_M^n)^2 + (\tau + 2\tau(1+\tau)\tan^2(\theta/2))} \tag{1.2}$$

and

$$A_\parallel = -\frac{2\tau\sqrt{1+\tau+(1+\tau)^2\tan^2(\theta/2)}\tan(\theta/2)}{(G_E^n/G_M^n)^2 + (\tau + 2\tau(1+\tau)\tan^2(\theta/2))}. \tag{1.3}$$

The variables are defined for the lab frame: P_b, P_t, and h are the beam polarization, target polarization, and incident electron helicity, respectively; θ^* is the lab polar angle and ϕ^* is the azimuthal angle of the target polarization with respect to the axis of the momentum transfer and scattering plane; θ is the electron scattering angle with respect to the electron beam direction; and $\tau = Q^2/4m_N^2$ is the square of the momentum transfer scaled by the nucleon mass squared.

In this experiment, the target spin was nominally aligned perpendicularly to the momentum transfer. This separates the perpendicular asymmetry $A_\perp$ from the longitudinal asymmetry $A_\parallel$, and the perpendicular asymmetry is measured. In our kinematics, $(G_E^n/G_M^n)^2$ is small compared to the second term of the denominator of Eq. 1.2; therefore, G_E^n/G_M^n is nearly proportional to $A_\perp$. Due to the large acceptance of the electron spectrometer and the neutron arm, there are small, non-zero contributions from longitudinal asymmetry that will need to be taken into account.

1.2 Experimental Overview

This experiment, E02-013 [8], measures the asymmetry $A_\perp$ in the semi-exclusive quasi-elastic reaction $\overrightarrow{^3\mathrm{He}}(\vec{e}, e'n)$, where both the final state electron and neutron were detected. The dominant source of error for our measurement is the statistical accuracy. To improve statistical accuracy in a finite amount of time, the rate of detected particles must be maximized. This was achieved by optimizing the beam energy and spectrometer angle, and by adjusting the beam current, the detector acceptance, and the target thickness.

The maximum beam current was limited by the rate at which the data can be recorded and the durability of the target. For a given beam current, the statistical accuracy can be improved by increasing the acceptance of the detector. However, an increase in the acceptance of the detector can also limit the precision of the experiment by introducing an uncertainty in the scattering angle of the electron.

In a fixed target electron scattering experiment, the target is chosen to maximize the likelihood that the incoming electron will scatter from a particle within the target and be detected in the spectrometer. This is done by increasing both the target density and length. For a polarized target, the desire is to maximize the likelihood of the electron scattering from a polarized particle. The designed thickness of the target is determined so that polarization, durability, and stability are maximized, and multiple scattering is minimized.

The combination of a high pressure (10 atm), highly polarized (50%) ^{3}He target and a large acceptance, open geometry spectrometer, BigBite, provides a better combination of statistical and systematic uncertainty than previous double-polarized G_E^n experiments [5]. BigBite is a non-focusing dipole magnet with an acceptance of 76 msr over a 40 cm target. The electrons were detected with a detector stack consisting of 15 planes of wire chambers, a scintillator plane, and a lead glass calorimeter. During production data-taking, the wire chambers operated at a total rate of 20 MHz per plane. The calorimeter was used to trigger on electrons with energy greater than 600 MeV to reach an acceptable trigger rate of 2 kHz.

To maximize the size of the asymmetry and to suppress the inelastic contributions, the scattered neutron was detected. The measurement of the neutron momentum provides information about the missing momentum, which controls the size of the correction due to final state interactions. Detection of the neutron for this experiment was accomplished by means of a large time-of-flight spectrometer. The spectrometer was built to match the acceptance of the BigBite spectrometer, with an active frontal-area area of 8 m^2 made up of 244 neutron bars and 196 veto counters. A time-of-flight resolution of better than 0.5 ns was achieved in this experiment.

1.3 ^{3}He Targets

The principle of spin-exchange optical pumping (SEOP) has been developed in the last 25 years [9]. Circularly polarized laser light excites the $5S_{1/2} \rightarrow 5P_{1/2}$ transition of an alkali metal in a magnetic field, quickly polarizing all of the alkali atoms. Polarization is then transferred from the alkali metal atoms to the ^{3}He nuclei by means of a hyperfine-like interaction between the outer electron of the alkali and the ^{3}He nucleus.

This experiment was the first to harness an important advance in the field of SEOP, the so-called hybrid method of SEOP (HySEOP). Traditionally, the alkali metal described above has been a pure metal (typically Rb). Using a mixture of Rb and K resulted in a decreased time to reach maximum polarization and, for this experiment, a continuously-pumped in-beam polarization of over 50%. Experiments using a pure Rb SEOP were performed with in-beam polarization of approximately 40%. Because of the way target polarization contributes to the statistical uncertainty, the improvement in target polarization was equivalent to receiving over 50% more beamtime.

The spin-exchange efficiency for ^{3}He-K is, under idealized conditions, an order of magnitude greater than that for ^{3}He-Rb [10]. However, there remain technical difficulties to pumping K directly for these polarized gas targets. Rather, a mixture of Rb and K is used, and the Rb is directly optically pumped. The spin exchange cross section for Rb and K is extremely large (compared to *e.g.*, the Rb-^{3}He cross section) and as a result, the K and Rb have nearly equal spin polarizations [11]. The combination of the higher spin efficiency between K and ^{3}He and the very large spin transfer cross section results in a very fast time to reach maximum polarization ("spin-up" time) [12]. This more efficient hybrid spin-exchange optical pumping also provides an overall higher polarization [13].

1.4 Analytical Methods

The data were collected over two months. Nearly two billion coincident triggers were recorded from electron scattering from the production target. The Hall A Analyzer, Podd [14], was used to extract quasi-elastically scattered electron-neutron events.

These events were selected by cuts on the invariant mass, the time-of-flight, and the missing perpendicular momentum. Once these events were selected, further refinement is made. The accidental random background was estimated by observing an unphysical region in time (*i.e.* events that appear to move faster than light, so cannot be coincident events). This background was then subtracted from the selected neutrons.

The operation of a SEOP target requires the presence of a small quantity of nitrogen in the target (Sec. 4.1.1). This unpolarized nitrogen effectively dilutes the polarized signal. A correction factor can be determined by comparing the yield from a pure nitrogen target cell to the yield from the production target cell containing helium and nitrogen.

A further dilution can occur because of mostly unpolarized protons detected as neutrons. This is corrected through an understanding of proton-neutron conversion, which can be obtained through a study of events from different targets. In addition, if the scattered neutron interacts with the rest of the ^{3}He nucleus before being detected, an understanding of such an interaction with the final state requires input from theoretical models.

Finally, all detectors have a finite acceptance. A proper determination of the kinematics requires the correct averaging of events over these acceptances. Once these kinematic factors are determined, the form factor can be extracted from the data.

CHAPTER 2

Theoretical Basis

The development of quantum electro-dynamics (QED) provided a useful framework for describing the electromagnetic interactions of relativistic particles. Relativistic field theories can proceed from first principles to the description of the interactions of point-like particles with intrinsic spin.

However, interactions with particles that have an internal structure are more complicated. As early as 1933, measurements of the proton magnetic moment indicated that nucleons may have an internal structure [15]. However, as of this writing in 2009, no satisfactory complete description of the nucleon's internal structure exists. The goal of this experiment is to provide experimental input to the theoretical description of this structure.

2.1 Point Particle

Following the excellent description in *Quarks & Leptons* by F. Halzen and A.D. Martin [16], the simplest physical case study of the electromagnetic interactions of relativistic particles is the scattering of elementary, charged, spin-$\frac{1}{2}$ particles.

The proper description for this sort of interaction is the Dirac equation. In general,

its form is

$$H\psi = (\vec{\alpha}\cdot\mathbf{P} + \beta m)\,\psi, \tag{2.1}$$

where $\mathbf{P}$ is the momentum 3-vector for the particle, m is the mass of the particle, H is the Hamiltonian operator and ψ is the wavefunction. β and α_i are determined by satisfying the relativistic energy-momentum equation:

$$H^2\psi = \left(\mathbf{P}^2 + m^2\right)\psi. \tag{2.2}$$

Specifically, this implies that α_1, α_2, α_3, β all anti-commute with each other, and $\alpha_1^2 = \alpha_2^2 = \alpha_3^2 = \beta^2 = 1$. These requirements are satisfied by 4×4 matrices defined for different representations. In the Dirac-Pauli representation, the matrices can be written using the Pauli matrices and the identity matrix,

$$\vec{\alpha} = \begin{pmatrix} 0 & \vec{\sigma} \\ \vec{\sigma} & 0 \end{pmatrix}, \qquad \beta = \begin{pmatrix} I & 0 \\ 0 & -I \end{pmatrix} \tag{2.3}$$

where I is the 2×2 identity matrix, and $\vec{\sigma}$ are the Pauli matrices:

$$\sigma_1 = \begin{pmatrix} 0 & 1 \\ 1 & 0 \end{pmatrix}, \qquad \sigma_2 = \begin{pmatrix} 0 & -i \\ i & 0 \end{pmatrix}, \qquad \sigma_3 = \begin{pmatrix} 1 & 0 \\ 0 & -1 \end{pmatrix}. \tag{2.4}$$

In covariant form, The Dirac equation is written

$$(i\gamma^\mu\partial_\mu - m)\,\psi = 0, \tag{2.5}$$

where ψ is the wavefunction, ∂_μ is the 4-dimensional derivative operator $\left(\frac{d}{dt}, \nabla\right)$, m is the particle's mass, and γ^μ are the four Dirac matrices,

$$\gamma^\mu \equiv (\beta, \beta\vec{\alpha})\,. \tag{2.6}$$

This definition, and the implications of the energy-momentum requirement (Eq. 2.2), can be used to show that these matrices satisfy the anti-commutation relation:

$$\gamma^\mu\gamma^\nu + \gamma^\mu\gamma^\nu = 2g^{\mu\nu}, \tag{2.7}$$

where $g^{\mu\nu}$ is the the four dimensional metric tensor. Since $\gamma^0 = \beta$, this implies that $\gamma^{0\dagger} = \gamma^0$ and $(\gamma^0)^2 = I$.

2.1.1 Electromagnetic Current

By introducing the adjoint relationship,

$$\bar{\psi} \equiv \psi^{\dagger}\gamma^{0}, \tag{2.8}$$

the adjoint Dirac equation can be written:

$$i\partial_{\mu}\bar{\psi}\gamma^{\mu} + m\bar{\psi} = 0 \tag{2.9}$$

Multiplying the covariant form of the Dirac equation (Eq. 2.5) on the left by $\bar{\psi}$ and the adjoint form of the Dirac equation (Eq. 2.9) on the right by ψ and adding:

$$\bar{\psi}\gamma^{\mu}\partial_{\mu}\psi + \left(\partial_{\mu}\bar{\psi}\right)\gamma^{\mu}\psi = \partial_{\mu}\left(\bar{\psi}\gamma^{\mu}\psi\right) = 0. \tag{2.10}$$

This is suggestive of a continuity equation, $\partial_{\mu}j^{\mu} = 0$, where

$$j^{\mu} = \bar{\psi}\gamma^{\mu}\psi. \tag{2.11}$$

This is a general probability current, $j^{\mu} = (\rho, \mathbf{j})$. The introduction of charge allows one to consider j^{μ} as the electron current density:

$$j^{\mu} = -e\bar{\psi}\gamma^{\mu}\psi \tag{2.12}$$

The simplest physical example of this scattering is $e^{-}e^{-}$ scattering, referred to as Møller scattering (see Fig. 2.1). The transition amplitude written in terms of the electromagnetic current is

$$T_{fi} = -i\int j^{(1)}_{\mu}(x)\left(\frac{1}{q^{2}}\right)j^{\mu}_{(2)}(x)d^{4}x, \tag{2.13}$$

where $q = p_A - p_C$, or the energy-momentum 4-vector transferred to the other electron.

2.1.2 Particles with Structure

In the case of point-like particles, these interactions are calculable from first principles. The internal structure of a more complex particle introduces additional terms. The

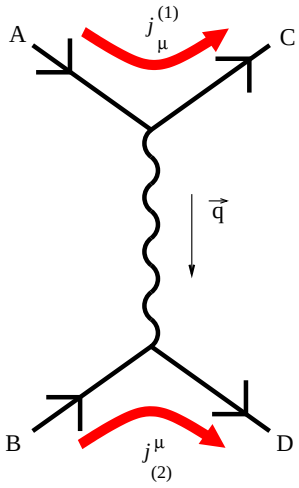

FIG. 2.1: **Møller Scattering.** Feynman diagram for Møller scattering. Incoming electrons are A and B; outgoing electrons are C and D. The current from A to C is $j_\mu^{(1)}$

transition amplitude for electron scattering from a proton is

$$T_{fi} = -i \int j_\mu \left(\frac{1}{q^2}\right) J^\mu d^4x, \tag{2.14}$$

where j^μ is defined as before, and J^μ is the electromagnetic current for the proton. The additional structure of the proton must be reprsented in the current. This current cannot be written as $\bar{\psi}\gamma^\mu\psi$. Instead, γ^μ must be replaced with a term indicating the additional structure. The most general Lorentz four-vector that conserves parity is:

$$J^\mu = \bar{\psi}\left[F_1(q^2)\gamma^\mu + \frac{\kappa}{2M}F_2(q^2)i\sigma^{\mu\nu}q_\nu\right]\psi \tag{2.15}$$

where κ is the anomalous magnetic moment, $\sigma^{\mu\nu} = \frac{i}{2}\left(\gamma^\mu\gamma^\nu - \gamma^\nu\gamma^\mu\right)$, M is the mass of the nucleon, and q is the transferred 4-momentum. F_1 and F_2 are two independent form factors.

2.2 Form Factors

The electromagnetic structure of the nucleon is described by two form factors, F_1 and F_2, also called Dirac and Pauli form factors, respectively. These two form factors are

used to parametrize the world ignorance of the nucleon. They are constrained by their values as $q \to 0$:

$$F_1^p(q^2 = 0) = 1, \qquad F_1^n(q^2 = 0) = 0 \tag{2.16}$$

$$F_2^p(q^2 = 0) = 1, \qquad F_2^n(q^2 = 0) = 1 \tag{2.17}$$

In the case of $q^2 = 0$, the expression for the current (Eq. 2.15) recovers its expected value. For the proton, the equation for a positively charged point particle is recovered; for the neutron, one recovers neutral point particle with a magnetic moment.

Using this current, the differential cross section for electron-nucleon scattering can be written

$$\frac{d\sigma}{d\Omega}\Big|_{\text{lab}} = \left(\frac{\alpha^2}{4E^2 \sin^4 \frac{\theta}{2}}\right) \frac{E'}{E} \left[\left(F_1^2 - \frac{\kappa^2 q^2}{4M^2} F_2^2\right) \cos^2 \frac{\theta}{2} - \frac{q^2}{2M^2} \left(F_1 + \kappa F_2\right)^2 \sin^2 \frac{\theta}{2}\right], \tag{2.18}$$

which is often referred to as the Rosenbluth formula. In this formula, E and E' are the incoming and outgoing electron energies, respectively, θ is the electron scattering angle with respect to the incoming electron, and α is the fine structure constant. Again, a structureless charged particle would have $F_1 = 1$ and $\kappa = 0$, in which case the Rosenbluth formula becomes:

$$\frac{d\sigma}{d\Omega}\Big|_{\text{lab}} = \frac{d\sigma}{d\Omega}\Big|_{\text{Mott}} \frac{E'}{E} \left[1 - 2\tau \tan^2 \frac{\theta}{2}\right], \tag{2.19}$$

where $\tau \equiv -\frac{q^2}{4M^2}$ and

$$\frac{d\sigma}{d\Omega}\Big|_{\text{Mott}} = \left(\frac{\alpha^2 \cos^2 \frac{\theta}{2}}{4E^2 \sin^4 \frac{\theta}{2}}\right) \tag{2.20}$$

is the Mott cross section.

2.2.1 Sachs Form Factors

The form factors F_1 and F_2 cannot be cleanly separated experimentally in the Rosenbluth equation. However, the form factors can be recast into linear combinations of the

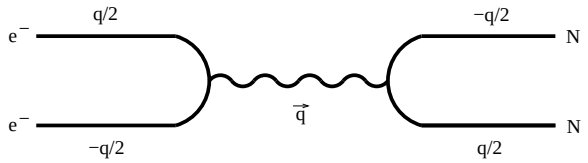

FIG. 2.2: **Breit Frame.** In the Breit, or brick wall frame, there is no energy transfer and the magnitude of the initial and final momenta are equal.

two:

$$G_E \equiv F_1 + \frac{\kappa q^2}{4M^2} F_2 \tag{2.21}$$

$$G_M \equiv F_1 + \kappa F_2 \tag{2.22}$$

These new form factors, respectively referred to as the electric and magnetic Sachs form factors, allow the Rosenbluth equation to be written:

$$\frac{d\sigma}{d\Omega}\Big|_{\text{lab}} = \left(\frac{d\sigma}{d\Omega}\right)_{\text{Mott}} \frac{E'}{E} \left(\frac{G_E^2 + \tau G_M^2}{1+\tau} + 2\tau G_M^2 \tan^2\frac{\theta}{2}\right) \tag{2.23}$$

which allows the experimental separation of G_E and G_M by measuring the cross section for a constant value of Q^2 while varying θ.

2.2.2 Physical Interpretation and the Breit Frame

These four form factors, G_M^p, G_M^n, G_E^p, and G_E^n, are collectively referred to as the Sachs form factors and can be related to the charge and magnetization distributions of the nucleons by means of a Fourier transformation in the Breit (or "brick wall") frame.

The Breit frame is the frame defined by the $\mathbf{p}_i = -\mathbf{p}_f$: the incoming and outgoing three-momenta are equal, but in opposite directions. In this frame, there is no energy transfer and the electron reacts as if it had bounced off a brick wall (see Fig. 2.2). The incoming momentum of the nucleon is $\mathbf{q}_B/2$ and the final momentum is $-\mathbf{q}_B/2$, which means that the four momentum squared $Q^2 = |\mathbf{q}_B|^2$ (where $Q^2 = -q^2$).

This transformation is hampered by the fact that the Breit frame is not physical, as there is a different Breit frame for every value of four-momentum transfer. As the four-momentum increases, the frame begins to move at relativistic speeds with respect to the lab frame, which affects the kinematics and interpretation of the structure [5].

Kelly Prescription

Unfortunately, some would argue that the transformation into such a non-physical frame of reference makes such measurements useless in determining the charge and magnetization distributions. A recently developed model helps to resolve these issues by performing the non-trivial transformation prescription [17, 18].

The prescription follows the method of relativistic inversion from Mitra and Kumari [19], which involves starting with a spherical charge and magnetization density in the nucleon rest frame, normalized to the static properties of the nucleon:

$$\int_0^\infty dr\ r^2 \rho_{ch}(r) = Z, \tag{2.24}$$

$$\int_0^\infty dr\ r^2 \rho_m(r) = 1, \tag{2.25}$$

where $Z = 0(1)$ is the charge for the neutron (proton). These densities are then transformed through a Fourier-Bessel transformation into "intrinsic" form factors:

$$\tilde{\rho}(k) = \int_0^\infty dr\ r^2 j_0(kr)\rho(r). \tag{2.26}$$

If these intrinsic form factors could be determined from the data, then a simple Fourier transform would convert them into the charge and magnetization densities. Simply substituting $\tilde{\rho}_{ch}(k) \rightarrow G_E(Q^2)$ produces unphysical cusps at the origin and hard cores. A proper treatment of the relativistic boost is required to account for the transformation of a composite system.

The synthesis of various models produces the prescription:

$$\tilde{\rho}_{ch} = G_E(Q^2)(1+\tau)^{\lambda_E} \quad (2.27)$$

$$\mu\tilde{\rho}_m = G_M(Q^2)(1+\tau)^{\lambda_M} \quad (2.28)$$

The factor $(1+\tau)$ is the Lorentz boost. The differences between the models are in the λs. For example, Ji determined $\lambda_E = 0$ and $\lambda_M = 1$ in the soliton model [20]; the difference arises from the difference in the transformation of scalar (charge) and vector (magnetization) quantities.

Kelly uses $\lambda_E = \lambda_M = 2$, as it preserves the scaling relation at large Q^2 as determined from pQCD (see Sec. 2.3.2) [17]. The charge density of the neutron resulting from this prescription can be seen in Fig. 2.3.

2.2.3 Previous Measurements

Previous methods of measuring the nucleon form factors fall into two main categories. First, is the Rosenbluth method, which requires a measurement of the eN cross-section. The other broad class of measurements make use of polarization observables. These measurements include the method of double polarization, used for this experiment. Previous measurements and theoretical curves are provided as Figs. 2.4, 2.5, 2.6, and 2.7.

Rosenbluth

In the Rosenbluth equation, 2.23, a separation of G_E^2 and G_M^2 can be obtained for any Q^2 by varying the incident beam energy and the scattering angle so that θ_e and τ vary while Q^2 remains a constant.

Due to the lack of free-neutron targets, measurements of the neutron form factors are performed on complex nuclei. The simplest of these is the deuteron. The deuteron is sufficiently complex to require recasting the form factors in terms of the charge, quadruple, and dipole magnetic distributions. These form factors are G_C, G_Q, and G_D. The

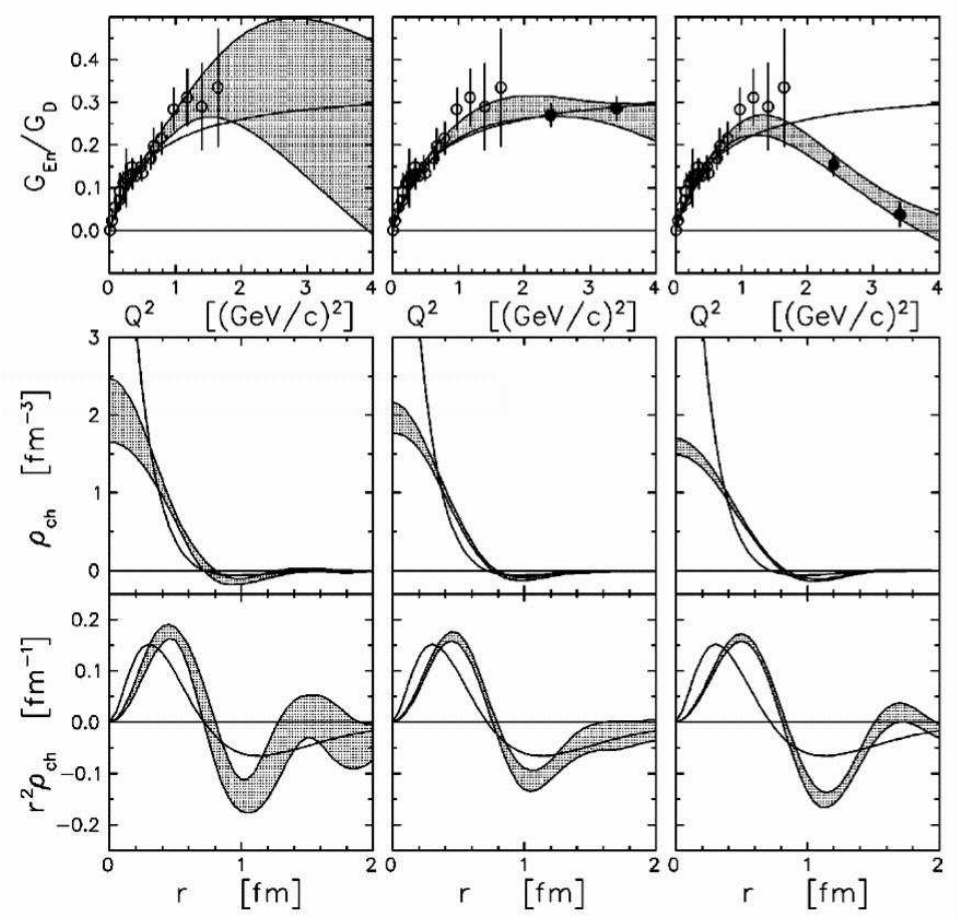

FIG. 2.3: **Kelly Neutron Charge Density.** The electric charge density of the neutron determined from the form factor G_E^n [17]. The first column uses the world data and its uncertainty prior to E02-013. The second column uses the projected uncertainty for E02-013, assuming that G_E^n will follow the Galster fit. The third column uses the projected uncertainty for E02-013, assuming that G_E^n is smaller than Galster at $Q^2 < 2$ (GeV/c)^2.

Rosenbluth equation for electron-deuterium elastic scattering can then be written [21]:

$$\frac{d\sigma}{d\Omega} = \frac{d\sigma}{d\Omega}\Big|_{\rm Mott} \left(A(Q^2) + B(Q^2) \tan^2 \frac{\theta_e}{2} \right), \tag{2.29}$$

where $A(Q^2) = G_C^2(Q^2) + \frac{8}{9}G_Q^2(Q^2) + \frac{2}{3}\eta(1+\eta)G_M^2$ and $B(Q^2) = \frac{3}{4}\eta(1+\eta)^2 G_M^2(Q^2)$, with η taking the place of τ from the expressions for the free nucleon: $\eta = Q^2/4M_D$, where M_D is the mass of the deuteron. The deuteron form factors are related to the neutron and proton form factors and the Fourier transforms of combinations of the S and D-state wave functions of the deuteron [5]

$$\begin{aligned} G_C &= G_E^S C_E, \\ G_Q &= G_E^S C_Q, \text{ and} \\ G_M &= \frac{M_D}{M_p}\left(G_M^S C_S + \frac{1}{2} G_E^S C_L \right). \end{aligned}$$

The isoscalar electric and magnetic form factors, $G_{E,M}^S$ is defined in terms of the neutron and proton form factors,

$$G_{\rm E,M}^S \equiv G_{E,M}^n + G_{E,M}^p. \tag{2.30}$$

An early functional form for the neutron electric form factor from a Rosenbluth measurement arose from a measurement at DESY in 1971 [6]. As a result of this experiment and many others [5], as well as the Feshbach-Lomon wave function [22], a fit was performed. The result was the well-known Galster parametrization:

$$G_E^n(Q^2) = -\frac{\mu_n \tau}{1 + 5.6\tau} G_E^p(Q^2), \tag{2.31}$$

where μ_n is the neutron magnetic moment. In most cases, estimates of G_E^n that quote the Galster parametrization replace G_E^p with the dipole form,

$$G_D = \frac{1}{\left(1 + \frac{Q^2}{0.71 {\rm GeV}^2}\right)^2}. \tag{2.32}$$

The dipole form shows very close agreement with G_E^p at $Q^2 < 1$ GeV^2 [5].

The Rosenbluth method is more useful at lower Q^2 values, particularly for the neutron. At higher Q^2, G_M becomes dominant to the point where such a separation becomes quite impractical. For the neutron, the overall electrical neutrality means that the electric form factor is very small. Early experimental measurements were unable to distinguish between $G_E^n = 0$ and the Galster parametrization [5].

Polarization Transfer

Originally proposed by Akhiezer [23, 24], the use of polarized observables has lead to much greater precision in the measurement of nucleon form factors. These measurements require a polarized electron beam and either a polarized nucleon or recoil polarimetry.

The derivation of the form factors given earlier in this work assumes a sum over the spin degrees of freedom. If the spin states are not summed, the polarization components can be written in terms of the polarization components P_x and P_z, and the form factors G_E and G_M:

$$I_0 P_x = -2\sqrt{\tau(1+\tau)} G_E G_M \tan\frac{\theta}{2} \tag{2.33}$$

$$I_0 P_z = \frac{1}{M}(E+E')\sqrt{\tau(1+\tau)} G_M^2 \tan^2\frac{\theta}{2} \tag{2.34}$$

where

$$I_0 = G_E^2(Q^2) + \tau G_M^2(Q^2)\left(1 + 2(1+\tau)\tan^2\frac{\theta}{2}\right), \tag{2.35}$$

z is the direction of momentum transfer, and x is perpendicular to z, but is confined to the electron scattering plane.

Therefore, the ratio G_E/G_M can be written in terms of these transverse and longitudinal polarizations,

$$\frac{G_E}{G_M} = -\frac{P_x}{P_z}\frac{(E+E')}{2M}\tan\frac{\theta}{2}. \tag{2.36}$$

Double Polarized Method

Raskin and Donnelly [25, 26] developed a formalism for double polarized experiments that allows the measurement of the ratio G_E/G_M using the scattering of polarized electrons from a polarized target. This method requires the measurement of an asymmetry. For our experiment, polarized ^{3}He is a suitable stand-in for a neutron target, as described in Chapter 4, specifically Sec. 4.1.

In the Born approximation, the polarized cross section can be written as the sum of two parts: the unpolarized cross section Σ, and a polarized part Δ, which depends on the electron's helicity. The total helicity-dependent cross section can therefore be written:

$$\sigma_h = \Sigma + h\Delta, \tag{2.37}$$

where $h = \pm 1$ indicates the electron helicity. The asymmetry is therefore defined:

$$A_N = \frac{\sigma_+ - \sigma_-}{\sigma_+ + \sigma_-} = \frac{\Delta}{\Sigma} \tag{2.38}$$

The denominator, Σ is the unpolarized cross section, given by Eq. 2.23. The polarized part is given by:

$$\Delta = -2\sigma_{\text{Mott}}\sqrt{\frac{\tau}{1+\tau}}\tan\frac{\theta}{2}\left[\sqrt{\tau\left(1+(1+\tau)\tan^2\frac{\theta}{2}\right)}\cos\theta^* G_M^2 + \sin\theta^*\cos\phi^* G_M G_E\right], \tag{2.39}$$

where θ^* and ϕ^* are the angles of target polarization with respect to the axis of the momentum transfer and the electron scattering plane, and θ^* is the polar and ϕ^* is azimuthal angle. By aligning the target spin perpendicular to the momentum transfer in the scattering plane of the electron, the perpendicular asymmetry is isolated:

$$A_\perp = -\frac{G_E}{G_M}\cdot\frac{2\sqrt{\tau(\tau+1)}\tan\frac{\theta}{2}}{(G_E/G_M)^2 + (\tau + 2\tau(1+\tau)\tan^2\frac{\theta}{2})} \tag{2.40}$$

In practice, the finite acceptance of physical detectors also measures a small contribution

from the longitudinal asymmetry:

$$A_{\|} = -\frac{2\tau\sqrt{1+\tau+(1+\tau)^2\tan^2\frac{\theta}{2}}\tan\frac{\theta}{2}}{(G_E/G_M)^2+(\tau+2\tau(1+\tau)\tan^2\frac{\theta}{2})} \tag{2.41}$$

2.3 Neutron Models

2.3.1 Dipole

Perhaps the simplest parametrization possible comes about from modeling the charge or magnetization of the nucleon as a decaying exponential with a maximum at the center. If the charge distribution is written

$$\rho_{\mathrm{m,ch}}(r) = \frac{m^3}{8\pi}e^{-mr}, \tag{2.42}$$

the corresponding form factor is

$$G_D = \left(1+\frac{Q^2}{m^2}\right)^{-2}. \tag{2.43}$$

This is the dipole form of the form factor attributed to Hofstadter and Wilson [27]. In the case of magnetic form factors, the dipole must be scaled by the magnetic moments of the proton and neutron, μ_p and μ_n:

$$\frac{G_M^p(Q^2)}{\mu_p} = \frac{G_M^n}{\mu_n} = \left(1+\frac{Q^2}{0.71\mathrm{GeV}^2}\right)^{-2} \tag{2.44}$$

where the $m^2 = 0.71\ \mathrm{GeV}^2$ is determined from proton form factor data [28].

For low values of Q^2, the dipole is also a good fit to the magnetic form factor data. However, for values of $Q^2 \gtrsim 1\ \mathrm{GeV}^2$ values of G_E^p decrease very quickly with respect to the dipole form factor. This behavior is only seen in the high-precision form factor data taken from polarization observables, and is not seen in Rosenbluth method measurements above $1\ \mathrm{GeV}^2$ [5].

Galster

The dipole form cannot be used for the neutron form factor because $G_E^n(Q^2 = 0) = 0$ and $G_D(Q^2 = 0) = 1$. The parametrization from the 1971 Rosenbluth measurement at DESY, referred to as the Galster parametrization, has the correct behavior at $Q^2 = 0$. Recall Eq. 2.31, replacing G_E^p with G_D,

$$G_E^n(Q^2) = -\frac{\mu_n \tau}{1 + 5.6\tau} G_D(Q^2).$$

This form still remains a remarkably successful parametrization, although the original parameters have been generalized. The generalized version,

$$G_E^n(Q^2) = \frac{a_G \tau}{1 + b_G \tau} G_D, \tag{2.45}$$

where $a_G = 1.73$, is constrained by the root mean square charge radius of the neutron as measured by thermal neutron scattering. This leaves b_G as a free parameter. Fits to data have determined $b_G = 4.59$ [29].

Kelly Neutron Electric Form Factor Parameterization

In his determination of the charge and magnetization densities of the nucleons from form factor data [17], Kelly expanded the form factors in a Fourier-Bessel expansion. Soon after he followed up with a simpler parametrization [18],

$$G(Q^2) \approx \frac{\sum_{k=0}^{n} a_k \tau^k}{1 + \sum_{k=1}^{n+2} b_k \tau^k}, \tag{2.46}$$

for the form factors: G_E^p, G_M^p, and G_M^n. The degree of the denominator is greater than the degree of the numerator to ensure $G \propto Q^{-4}$ for large Q^2. Using $n = 1$ and $a_k = 1$, only four additional parameters (a_1, b_1, b_2, and b_3) are required to achieve good agreement with the data [18].

For G_E^n, he proposed the generalized Galster parametrization in Eq. 2.45. The values for a_G and b_G, which are considerably different from the Galster parametrization, as well

Version	a_G	b_G	$\langle r_n^2 \rangle$ (fm^2)
Galster [6]	1	5.6	-0.112
Friedrich [29]	1.73	4.59	-0.115
Kelly [17]	1.70	3.30	-0.112

TABLE 2.1: **Comparison of Various Galster Parameters.** The different parameters used in Eq. 2.45; the root mean square charge radius values are determined by thermal neutron scattering.

as the corresponding root mean squared charge radius for these models are included in Table 2.1. The charge radius is negative, indicating the charge distribution is positively charged at the center, and negatively charged at larger radii. This distribution is consistent with the simple description of a neutron as a proton surrounded by a negative pion cloud.

2.3.2 QCD

Quantum Chromodynamics (QCD) is the theory of the strong interaction and in principle can be used to calculate G_E^n. However, perturbative calculations in QCD involve expansions in the strong coupling constant. This coupling constant, α_S, changes with the momentum transfer of the reaction. For low Q^2 reactions, the coupling constant becomes larger than unity and perturbative calculations do not converge.

pQCD

The measurements of G_E^n by E02-013 are at energies that approach the practical use of perturbative QCD (pQCD). According to Belitsky, Ji, and Yuan [30], the dominant contribution to a calculation of $F_2(Q^2)$ comes from configurations in which the quarks in the initial state carry zero orbital angular momentum, and the quarks in the final state carry one unit of angular momentum (or vice versa). In this model the ratio of F_2/F_1 reproduces the logarithmic scaling seen in the polarization transfer measurements of G_E^P

[31, 32].

$$\frac{F_2(Q^2)}{F_1(Q^2)} \approx \frac{\log^2\left(\frac{Q^2}{\Lambda^2}\right)}{Q^2} \tag{2.47}$$

where Λ is a soft scale related to the size of the nucleon, ranging between 200 and 400 MeV.

2.3.3 Vector Meson Dominance

The vector meson dominance model describes the electromagnetic interaction with hadrons. In this model, the virtual photon first transforms into an intermediate vector meson before interacting with the hadron. Vector mesons have the same quantum numbers as the photon. The lowest lying mesons with vector quantum numbers are $\rho(770)$, $\omega(782)$, and $\phi(1020)$. These mesons are prominent resonances in $e^+e^- \rightarrow$ hadrons, and one can speculate that these resonances should feature prominently in $eN \rightarrow eN$ reactions at low energy.

Early vector meson fits have proven quite successful, including predicting the roughly linear decrease of the proton G_E^p/G_M^p ratio [5]. They continue to be successful for fits to form factor data [33].

2.3.4 Constituent Quark Model

The constituent quark model predates QCD. There is not a single constituent quark model, but many variations on this theme. What these theories share is a model of the nucleon as the ground state of a quantum-mechanical three-quark system in a confining potential.

Although these models are quite successful in describing the spectrum and structure of low-lying baryons, they do not satisfy all symmetry properties of the QCD Lagrangian. In the massless quark limit, the QCD Lagrangian is invariant under $SU(2)_L \times SU(2)_R$ rotations of left and right handed quarks in flavor space. In nature, this chiral symmetry is

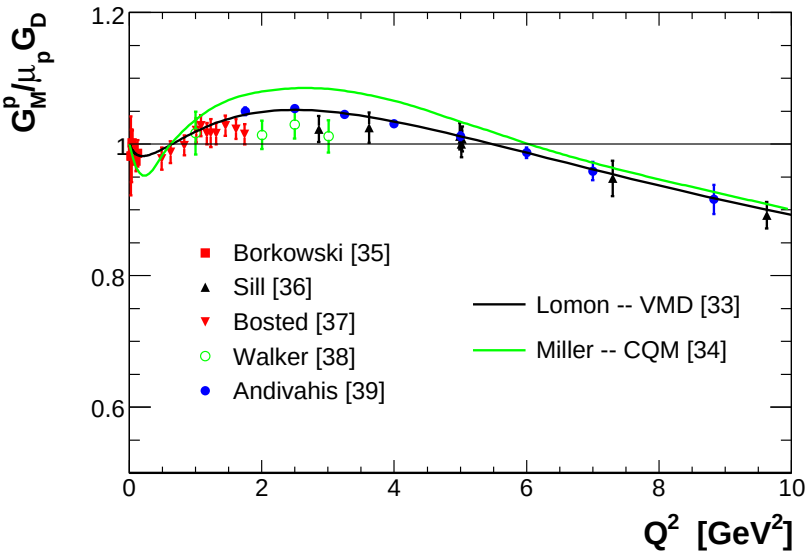

FIG. 2.4: G_M^p **World Data and Theoretical Curves.** Experimental measurements of G_M^p, scaled by the dipole. Theoretical curves representing vector meson dominance and constituent quark models have been included.

spontaneously broken, giving rise to Goldstone bosons (three, in the case of two flavors). These are the pions, which acquire mass through the explicit breaking of the symmetry by the current quark masses [5].

The constituent quark models are improved by the addition of a pion degree of freedom. Miller recently calculated the form factors using a "cloudy-bag model", so-called because it combines the constituent quark "bag model" with the pion cloud [34].

2.3.5 Generalized Parton Distributions

Generalized Parton Distributions (GPDs) are universal functions containing nucleon structure information. They are generalizations of the parton distribution functions derived from deep inelastic scattering. They are constrained by the electromagnetic form factors [2, 3].

The GPDs H, E, $\tilde{H}$, and $\tilde{E}$ depend on the following variables: x, the fraction of the nucleon momentum carried by the struck quark; ξ, the skewness, or longitudinal momen-

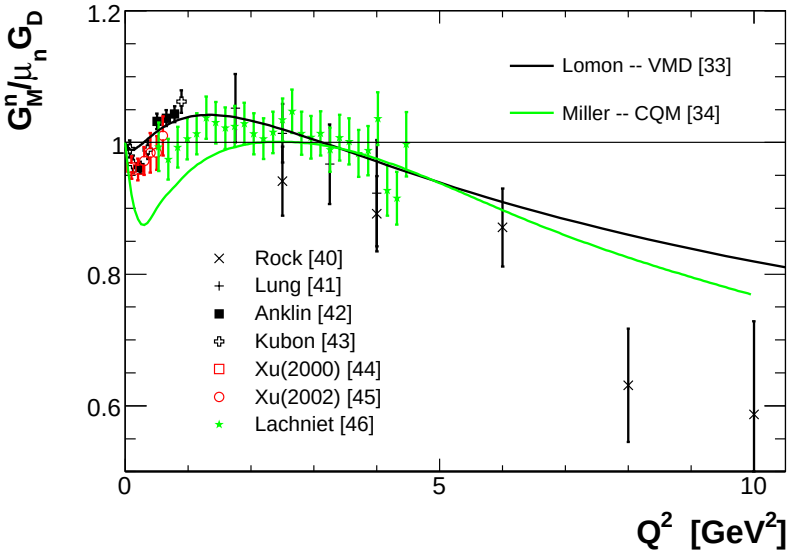

FIG. 2.5: G_M^n **World Data and Theoretical Curves.** Plot of theoretical interpretations with selected data scaled to the dipole approximation.

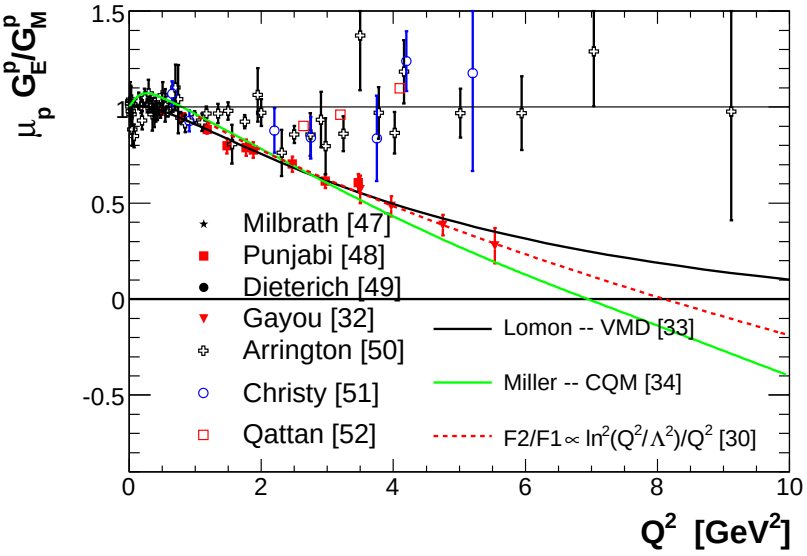

FIG. 2.6: G_E^p **World Data and Theoretical Curves.** Plot of selected data. A plot of the predicted pQCD scaling is included, scaled to fit polarization data.

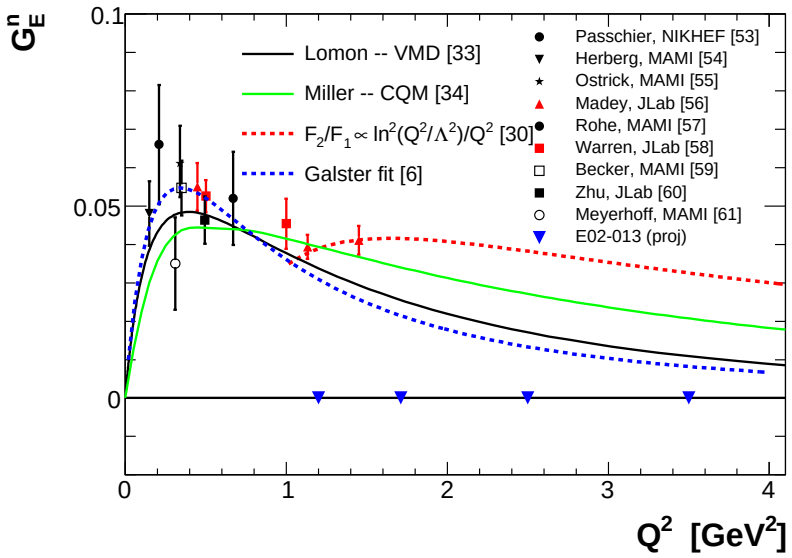

FIG. 2.7: G_E^n **World Data and Theoretical Curves.** Plot of theoretical interpretations with polarization observable data and the location of data taken for this experiment.

tum asymmetry; and t the momentum transfer to the target nucleon [3]. Unlike the other models of the nucleon listed here, GPDs are not currently used to calculate form factors. Rather, the form factors serve as constraints on the various GPDs. At $\xi = 0$, the F_1 form factors can be written in terms of the GPD H for the valence quarks

$$F_1^p(t) = \int_0^1 dx \left(\frac{2}{3} H_{\rm v}^u(x,t,\xi) - \frac{1}{3} H_{\rm v}^d(x,t,\xi) \right) \quad (2.48)$$

$$F_1^n(t) = \int_0^1 dx \left(\frac{2}{3} H_{\rm v}^d(x,t,\xi) - \frac{1}{3} H_{\rm v}^u(x,t,\xi) \right). \quad (2.49)$$

Similarly, the F_2 form factors can be written in terms of the GPD E

$$F_2^p(t) = \int_0^1 dx \left(\frac{2}{3} E_{\rm v}^u(x,t,\xi) - \frac{1}{3} E_{\rm v}^d(x,t,\xi) \right) \quad (2.50)$$

$$F_2^n(t) = \int_0^1 dx \left(\frac{2}{3} E_{\rm v}^d(x,t,\xi) - \frac{1}{3} E_{\rm v}^u(x,t,\xi) \right). \quad (2.51)$$

A quark flavor separation of these GPDs when constrained in some models requires a measurement of G_E^n at high t.

These GPDs can then be used to calculate a variety of nucleon properties [1], and may give insight into the contribution to the spin of the nucleon from quark orbital angular

momentum [20]. Recent calculations using the GPD's have provided insight into the transverse distribution of partons within the nucleon [62, 2]. GPDs using form factor input have also provided new methods of calculating the charge distributions of nucleons [63, 64, 65] without resorting to the Breit frame transformations.

CHAPTER 3

Experimental Overview

The experiment, Jefferson Lab E02-013, was a measurement of the double polarized asymmetry of the reaction $^3\overrightarrow{\mathrm{He}}(\vec{e}, e'n)X$. The double polarized asymmetry was measured using a polarized electron beam and a polarized ^{3}He target. The semi-exclusive coincidence events were detected through a combination of a large non-focusing dipole spectrometer with multiple wire drift chambers (MWDC) in coincidence with a large time of flight spectrometer. A schematic of the experiment setup can be seen in Fig. 3.1.

Data were collected from February 28, 2006 until May 10, 2006. These data were taken at four kinematic settings corresponding to $Q^2 = 1.4,\ 1.7,\ 2.5$, and $3.4\ \mathrm{GeV}^2$. The experimental parameters for the results presented here are listed in Table 3.1.

3.1 Coordinate Systems

Four different systems were employed for E02-013 (see Fig. 3.2). Each had its own coordinate system: the standard lab coordinate system (for the polarized beam), the electron optics coordinate system, the electron detector coordinate system, and the neutron detector coordinate system.

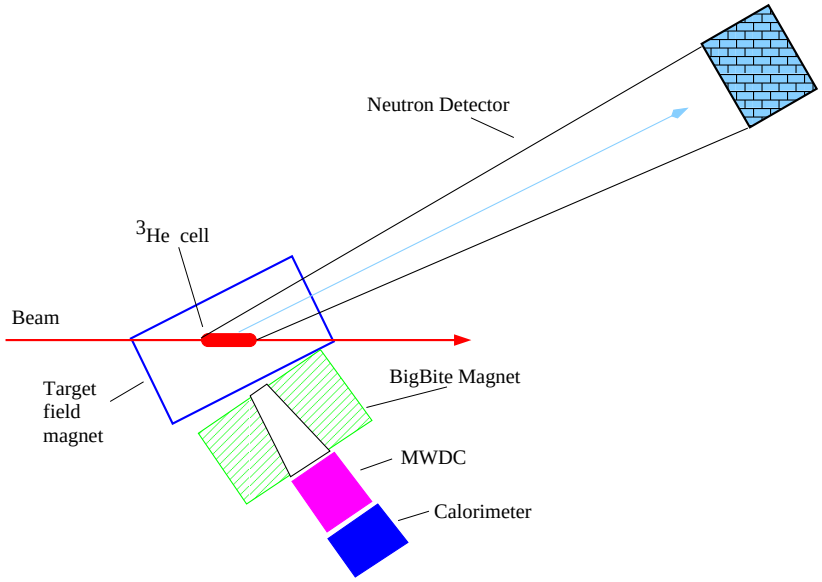

FIG. 3.1: **Overhead View of Experimental Set-Up.** Configuration of experimental pieces as they were arranged in Hall A for E02-013.

Kinematic Setting	4	2	3
Q^2 (GeV^2)	1.7	2.5	3.4
Dates	May 5 - May 10	Mar 10 - Mar 21 Apr 17 - Apr 24	Mar 21 - Apr 17 Apr 24 - May 5
$\mathrm{E_{beam}}$ (GeV)	2.079	2.640	3.291
$\langle\theta_e\rangle$ $(^\circ)$	51.6	51.6	51.6
$\langle\theta_n\rangle$ $(^\circ)$	33.8	29.2	24.9
Neutron TOF distance (m)	33.8	29.2	24.9
$\langle P_e\rangle$ $(\%)$	85.2	85.0	82.9
$\langle P_{\mathrm{He}}\rangle$ $(\%)$	48.5	45.2	47.7
$\mathrm{Q_{beam}}$ (C)	2.2	3.5	11.4

TABLE 3.1: **Kinematic Settings.**Kinematic settings and parameters for data taken in E02-013. Kinematic

The standard lab coordinate system has its origin at the center of the target. The z-axis is defined by the nominal direction of momentum of the electron beam, y is defined against gravity (positive y is "up"), and x is defined as to the left when looking in the direction of positive z. They form a right- handed coordinate system.

The electron optics coordinate system (Sec. 3.4.3) has its origin at the intersection of the BigBite central ray with the lab z axis. Positive x is in the direction of gravity (*i.e.*, "down"), z is parallel to the hall floor and in the direction of the BigBite central ray, and y forms a right-handed coordinate system.

The electron detector coordinate system origin is determined by the center of the first plane of the drift chambers. The z axis is normal to that first plane, and the nominal direction of particles. It is at an angle with the lab x-z plane equal to the pitch of the drift chamber stack ($\approx 10^{\circ}$). The x axis is perpendicular to the direction of the wires in the X wire plane (see Sec. 3.4.2, and especially Fig. 3.12). The y axis is defined to form a right-handed coordinate system [67].

The neutron detector coordinate system is defined with x opposite gravity (*i.e.*, "down"). The direction z is normal to the scintillator plane, and y is defined to form a right handed coordinate system. The neutron detector is a wall of scintillator bars (Sec. 3.5.1), the x and z are therefore roughly determined by the particular scintillator bar in which the hit occurs. The y position is reconstructed through timing within the bar.

3.2 Electron Beam

E02-013 used the CEBAF high polarization electron beam, routinely reaching polarization in excess of 80%. The facility consists of a polarized electron source, an injector, two linear accelerators (linacs), two sets of recirculating magnetic arcs and a beam switchyard. The facility is capable of delivering a continuous, polarized electron beam to three experimental halls simultaneously. Because of the unique construction, electrons may

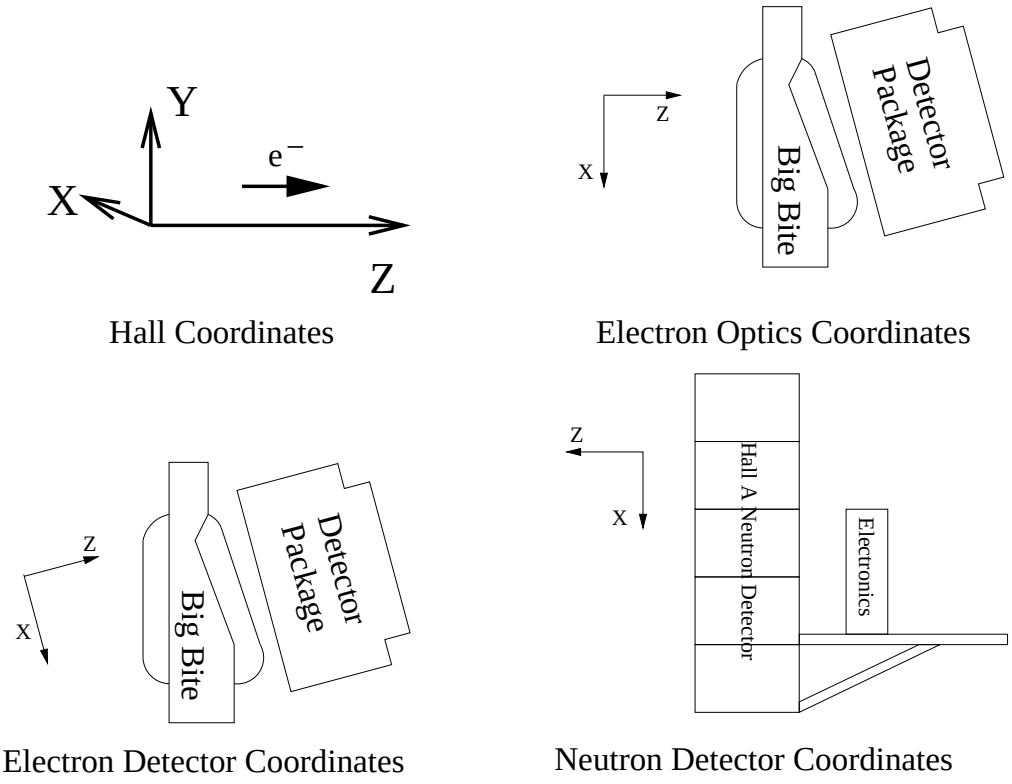

FIG. 3.2: **E02-013 Coordinate Systems.** Coordinate systems used in the analysis of data taken for E02-013.

pass through the accelerator up to five times before delivery into the hall, picking up a maximum of 1.2 GeV per pass. Each hall may have electrons of different energy, so long as they are integer multiples of the energy from a single pass (600 to 1200 MeV).

Polarized electrons are released from a strained GaAs cathode when it is struck with a circularly polarized laser beam. Rapid changes in laser polarization occurring every 33.3 ms, as detailed in Sec. 3.2.1, are accomplished by a Pockels cell. Systematic effects due to beam helicity can be isolated by inserting a half-wave plate to reverse the helicity of the beam.

These initial polarized electrons are initially accelerated to an energy of 100 keV. They are injected into the accelerator by passing through two superconducting accelerator cavities, referred to as a quarter-cryomodule. They are injected into the beam with an energy of 45 MeV. From there, they pass through 20 cryomodules (made of eight cavities each), accelerating to up to 600 MeV before passing through the first recirculating arc. The electrons then pass through another 20 cryomodules before either entering another recirculating arc to bring them back to the injector point or entering one of three experimental halls [68].

3.2.1 Beam Helicity

Properly forming the asymmetry required precise knowledge of the beam helicity. E02-013 used the delayed timing mode which was also used by the parity violating asymmetry experiment G0 [69].

The helicity signal takes a quad structure: $+\ -\ \ -\ +$, or $-\ +\ +\ -$. The time between helicity flips is 33.3 ms (so that each quad is 133.3 ms). To accommodate the Pockels cell changing and settling, the helicity information is not recorded for 0.5 ms after each helicity change. As a result, 1.5% of the events have an unknown helicity (denoted as helicity = 0).

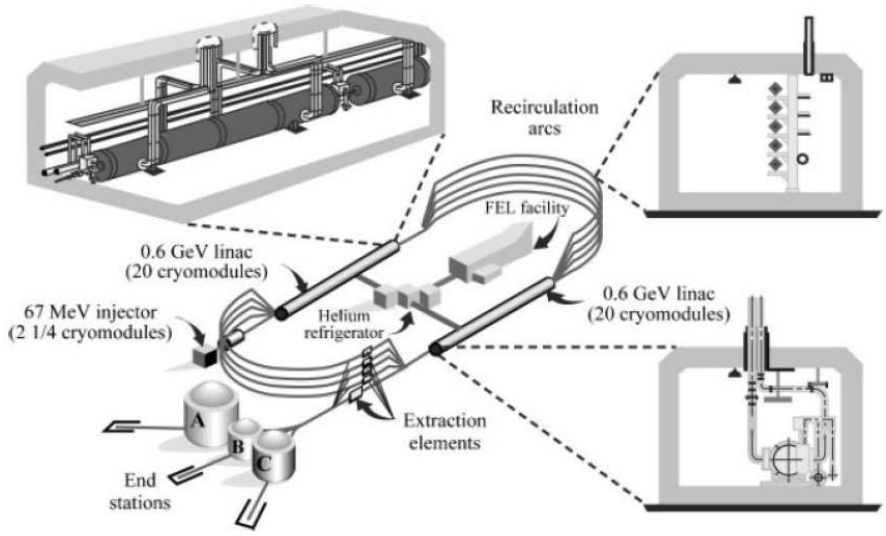

FIG. 3.3: **Diagram of CEBAF.** The Continuous Electron Beam Accelerator Facility provides the polarized electron beam to Hall A.

Four signals are used to decode the beam helicity: the Master Pulse Signal (MPS), a 30 Hz pulse used as a gate for the helicity; the quartet trigger (QRT), which indicates the beginning of a new helicity quad; the helicity signal and the 105 kHz clock. In general, only the first three are required (as seen in Fig. 3.4). However, if the helicity of the electron is missed due to, for example, DAQ deadtime, the 105 kHz clock signal can be used to determine an event's position in the helicity sequence as well as the position in the quad structure. Information from the first three signals (MPS, QRT, and helicity) is provided from a single read-out. The 105 kHz clock is read from three different scalers. The decoding program requires two matched scalers.

Beam Charge Asymmetry

The beam charge asymmetry, or asymmetry in electron helicity, is summarized in Table 3.2. Overall, the beam asymmetry is quite small. On a run-by-run basis, the asymmetry could have been as large as 0.2%, although an asymmetry of 10^{-5} is more typical.

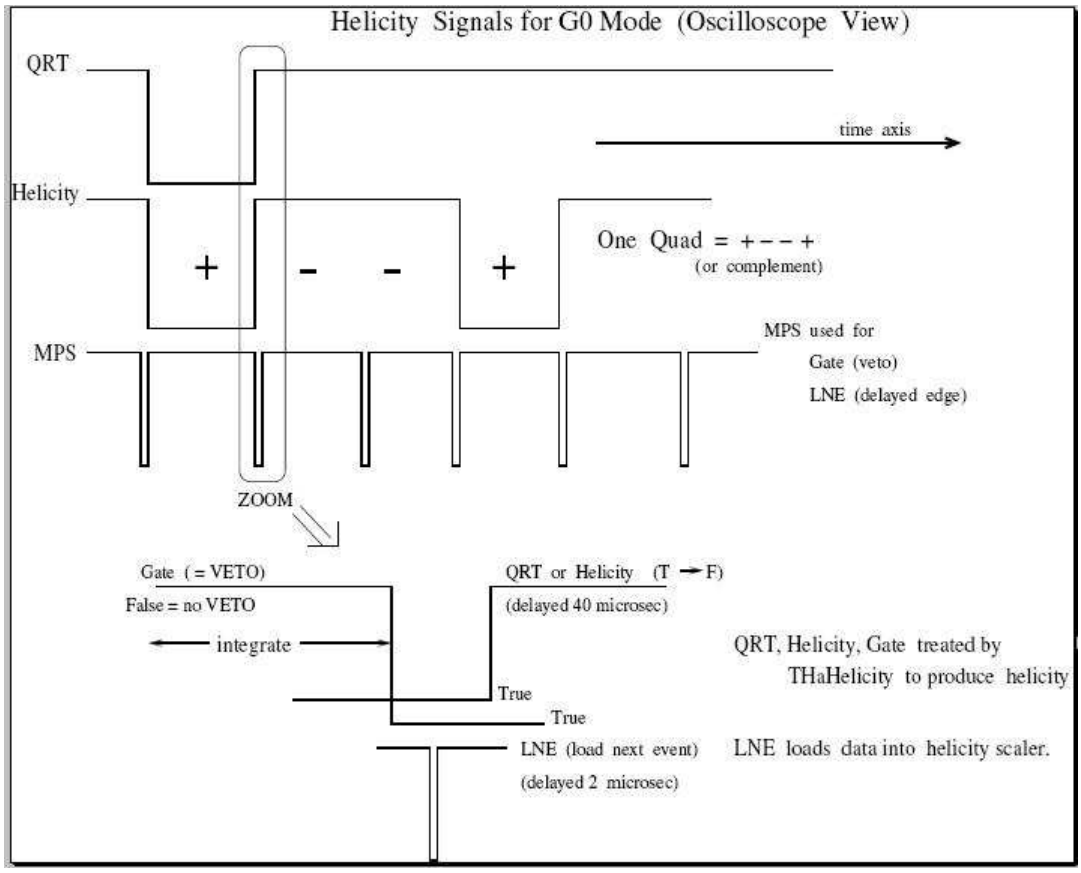

FIG. 3.4: **Helicity Decoding.** Three electronic signals are used to relate the helicity of the electrons to the time of the interactions.

Q^2	Mean Asymmetry	Median Asymmetry	Maximum Asymmetry
1.7 GeV^2	4.45×10^{-5}	2.59×10^{-5}	8.86×10^{-4}
2.5 GeV^2	8.35×10^{-5}	2.44×10^{-5}	7.68×10^{-3}

TABLE 3.2: **Beam Charge Asymmetry.** The beam charge asymmetry for each run was calculated from the beam current monitors. The mean, median and maximum of the absolute value of these asymmetries are presented.

This small value of beam charge asymmetry when compared to the physical asymmetry of the experiment implies that any helicity correlated false asymmetries must be small.

3.2.2 Beam Position and Raster

Two beam position monitors (BPM) provided information about the location of the beam within the beamline. These monitors are located 2.215 m and 7.517 m upstream from the target. The BPMs are calibrated through a HARP scan. HARP measurements are invasive measurements in which a sensing wire is moved into the beam to determine its location. These would be sufficient for an unrastered electron beam. However, it is necessary to raster the beam to prevent damage to the target cell, which is made of glass. Rastering the beam also protects the end window of the beamline, made thinner for this experiment to reduce background electron scattering.

The raster is achieved by applying quickly changing magnetic fields to slightly change the direction of the beam. Raster sizes of 2 mm $\times$ 2 mm at the target are typical, and the raster dipoles are located 23 m before the target. The raster is created by a triangular waveform applied to two air-core dipole magnets. The result is a uniform rectangular distribution, as seen in Fig. 3.5.

The frequency of the raster is 50 kHz, much higher than the band for the BPMs. Therefore, event-by-event knowledge of the beam position from the BPMs in regions where the raster changes directions (*i.e.*, the edges and corners of the rectangular pattern)

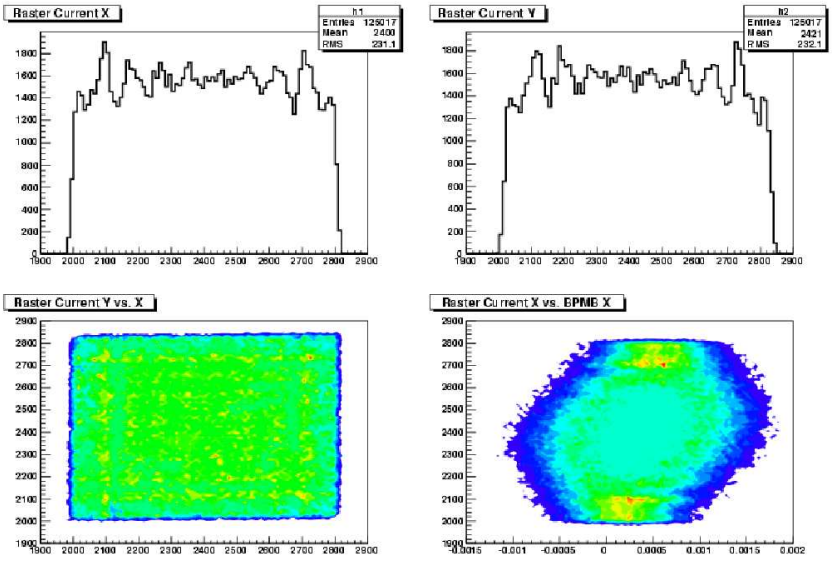

FIG. 3.5: **Raster vs. Beam Current.** Plot of raster versus beam current using data taken on the carbon foil target, Run 3356

is compromised. However, the precise vertex of the event can be determined by combining information from the raster current, the BPMs, and spectrometer data calibrated to optics foils.

The BPMs themselves need to be calibrated against an absolute measure of the beam position. This is done by a HARP measurement. For E02-013, the HARP scans could not be performed without the raster (due to concern over damaging the beamline end window), which required an experiment-specific calibration [70].

3.2.3 Beam Polarization

The beam polarization was measured six times during the experiment by using Møller scattering. This technique is based on the cross section of Møller scattering $(\vec{e^-} + \vec{e^-} \rightarrow e^- + e^-)$. This cross section depends on the beam and target polarizations. The Møller polarimeter uses a thin, magnetically-saturated ferromagnetic foil. This results in an average electron polarization in the target foil of approximately 8%. The foil can be tilted at angles

Date	Pol(%)
Feb 28, 2006	-88.43 ± 0.08
Mar 4, 2006	$+87.81 \pm 0.10$
Mar 9, 2006	-85.05 ± 0.08
Mar 25, 2006	-81.65 ± 0.09
May 10, 2006	-85.27 ± 0.06
May 12, 2006	$+84.77 \pm 0.20$

TABLE 3.3: **Møller Measurements.** Beam polarization measurements obtained through Møller scattering. The systematic uncertainty of 2% is not included.

20-160° to the beam, so that the effective target polarization is $P_{\text{target}} = P_{\text{foil}} \cdot \cos\theta_{\text{target}}$. A beam/target asymmetry is measured, and the beam polarization is obtained by:

$$P_Z^{\text{beam}} = \frac{N_+ - N_-}{N_+ + N_-} \cdot \frac{1}{P^{\text{foil}}} \cdot \cos\theta_{\text{target}} \cdot \langle A_{ZZ} \rangle \tag{3.1}$$

where $\langle A_{ZZ} \rangle$ is the average analyzing power, which depends solely on the center of mass angle scattering. This value was obtained from a Monte Carlo calculation of the spectrometer acceptance. The Møller measurements are invasive and require dedicated beam time. The results can be found in Table 3.3.

The Hall A Compton polarimeter was also used for the highest beam energy kinematics ($Q^2 = 2.5$ and $3.5\ \text{GeV}^2$). This was not used for measurements at $Q^2 = 1.4$ and $1.7\ \text{GeV}^2$ because the precision is very low for lower beam energies. The Compton polarimeter is a non-invasive measurement, and polarization measurements can be taken at the same time as the production data. In the Compton measurement, a polarized photon beam scatters from the polarized electron beam. This results in an asymmetry that is related to the beam and target polarization. The equation for the electron polarization is:

$$P_e = \frac{A_{\text{exp}}}{P_\gamma A_{\text{th}}} \tag{3.2}$$

where P_e and P_γ are the electron and photon beam polarizations, respectively. A_{th} is the theoretical asymmetry which is which is calculable from quantum electro-dynamics, and

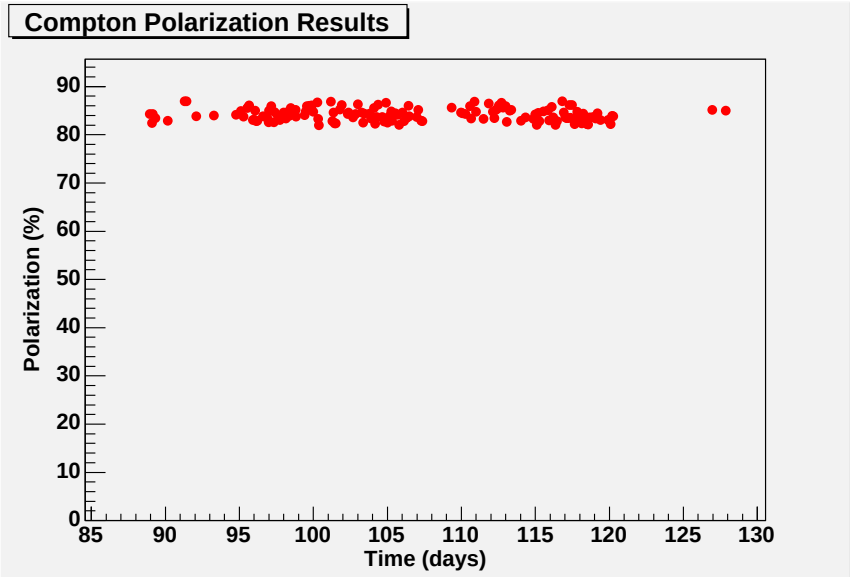

FIG. 3.6: **Compton Polarization.** Polarization for $Q^2 = 2.5$ and 3.5 GeV^2 kinematics as reported by the Hall A Compton Polarimeter. Systematic errors of 3% are not included.

A_{exp} is the measured asymmetry. To measure the Compton asymmetry, the electron beam is diverted through a chicane consisting of 4 dipole magnets. In the chicane, the beam intersects an optical cavity, where it interacts with polarized laser light. The back-scattered photons are detected by the photon detector, and the electron beam is directed from the photon detector by the chicane dipoles. Since the scattered electrons lose energy due to their interaction, the scattered electrons can be detected separately to reduce background. The complete results were provided [71]. A summary plot can be seen as Fig. 3.6. Statistical errors for the Compton measurements were typically between 1% and 2.5%; the systemmatic error is 3%.

3.2.4 Beam Energy

Information on the beam energy is obtained from the so-called “Tiefenback” method, which is a calculation based on a measurement of the deflection of a charged particle through a magnetic field. The Tiefenback measurement continuously monitors the beam

energy by using the relationship between the field integral value and the current setpoint in the eight dipoles that direct the beam into experimental Hall A [72]. Corrections to the measuresment are then applied by using the BPMs and the magnetic transfer functions along the Hall A beamline. The measurement has been calibrated against the invasive ARC measurement, which uses the same principle of beam deflection. The energy value obtained by the Tiefenback method is known to a relative accuracy of 5×10^{-4}, in agreement with invasive measurements not used during the present experimental run.

3.3 Target

This experiment used a polarized ^{3}He target. Polarized ^{3}He targets have successfully served as substitutes for free-neutron targets in a variety of electron scattering experiments at Jefferson Lab (see 4.1).

Details of the method of polarization, polarimetry, and the rest of the target system can be found in Chapter 4.

3.3.1 Direction of Magnetic Field

Extracting the proper ratio $\Lambda = G_E^n/G_M^n$ requires precise knowledge of the direction of the polarization. This can be clearly seen in the cosine dependence of θ^* on the measured asymmetry. A Monte Carlo simulation was performed and the uncertainty in G_E^n due to the uncertainty on θ^* was calculated to be as high as 1.6%/mrad, for the $Q^2 = 3.5\ \mathrm{GeV}^2$ point. Therefore, the angle of polarization must be known to better than 2 mrad to keep the contribution to the uncertainty on G_E^n small, relative to the statistical uncertainty.

To reach this required precision, a special compass was designed and built. The compass consists of a permanent magnet on a frictionless air bearing. The airflow required

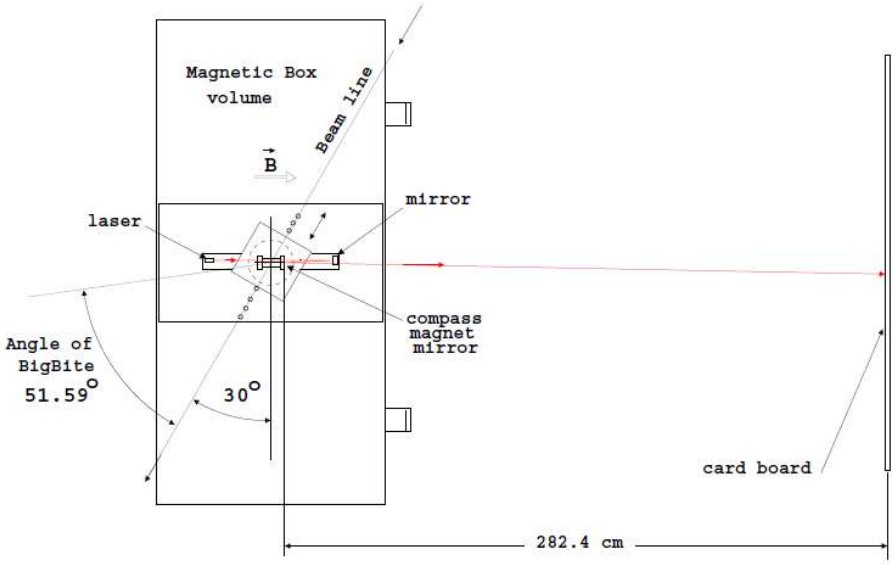

FIG. 3.7: **Diagram of Field Measurement Technique.** The combination of a laser and a magnet on an air bearing allowed measurements of the magnetic field along the length of the target cell.

for this bearing did produce a rotation, which was measured and taken into account. The magnetization axis and geometrical axis of the magnet were not coincident, but a rotation of the magnet allowed this effect to be removed from the final measurement. The compass direction was determined by using a laser pointer. The laser pointer was fixed in position, and shone on a mirror attached to the permanent magnet needle. The reproducibility of the laser pointer position was accomplished by first shining the light on a fixed reference mirror (Fig. 3.7 and 3.8). The light was reflected onto a screen. The deflection of the light (with a total path length of approximately 6 m) allowed the magnetic field direction to be determined within $2\ \mathrm{mrad}$. These measurements were repeated by moving the compass along the beamline. In addition, vertical spacers were added and removed. In this way, the field direction along the entire length of the cell was mapped, and contributions from the field above and below the beamline were calculated.

The results are plotted in Fig. 3.9. The accuracy was $2\ \mathrm{mrad}$. Along the length of the cell the field direction varies between 118.4° and 117.8°. The minimum occurs at the

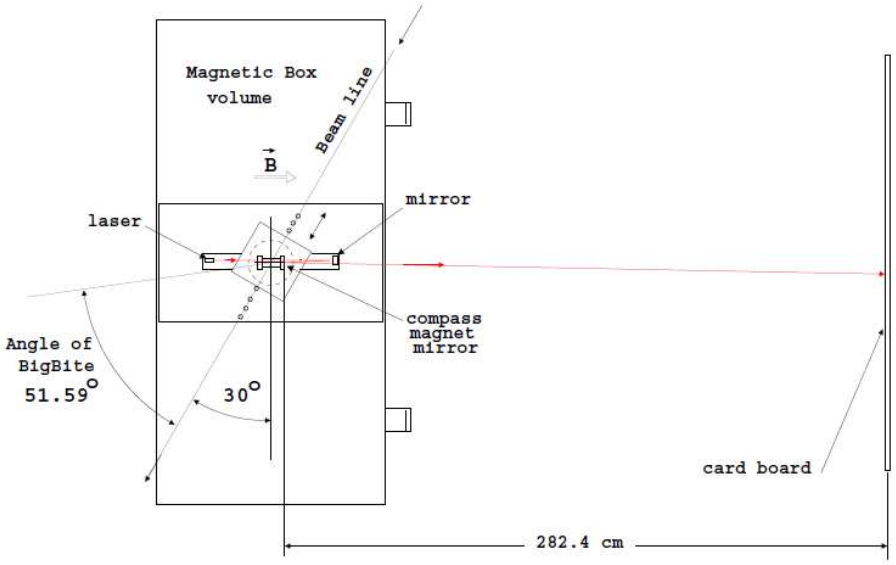

FIG. 3.8: **Diagram of Compass Calibration.** Calibration of the system was accomplished by use of a surveyed reference mirror.

center of the target cell.

3.4 Electron Spectrometer

The electron arm consists of a large non-focusing dipole magnet (called BigBite) and a set of detectors. The set of detectors consists of three multiple wire drift chambers, a segmented, two-layer electromagnetic calorimeter (consisting of a pre-shower and a shower counter), and a thin scintillator plane (Fig. 3.10)

The spectrometer magnet is called BigBite [73] because it has a large momentum and spatial acceptance. For the configuration used for E02-013, the average acceptance was 76 msr over the 40 cm length of the target, with an electron momentum acceptance of 0.6-1.8 GeV/c. The field integral was approximately 1 T·m. Even with the larger momentum acceptance, a momentum resolution of $\frac{\delta p}{p} = 1\%$ was achieved.

The tracking detector consists of three separate horizontal drift chambers spaced approximately 35 cm apart. The drift chambers are the first set of detectors after the

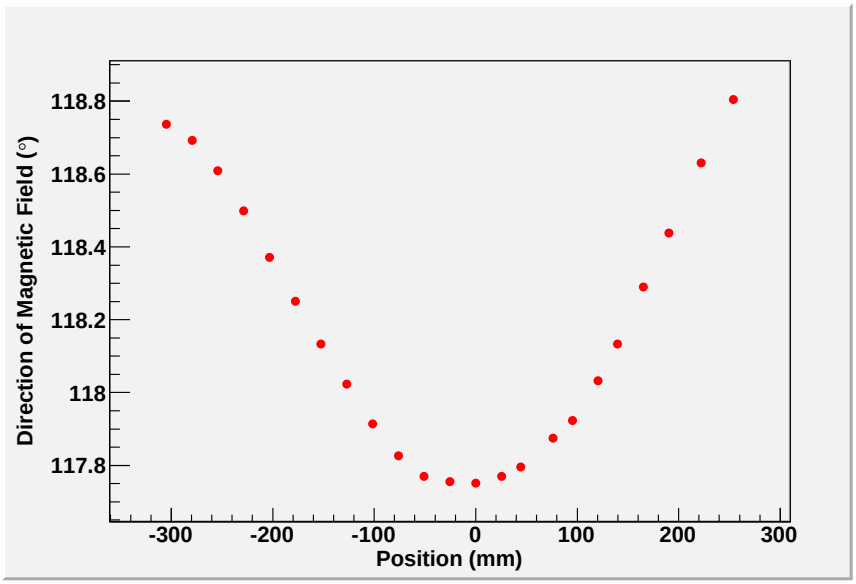

FIG. 3.9: **Results of Compass Measurement.** Results of the compass measurement show a variation of 0.6° along the length of the target cell (± 200 mm).

magnet. The maximum drift distance was 5 mm, which allows high rate capability. The drift chambers have the highest spatial resolution (200 μm) of the detectors used in this experiment. Tracking information was derived primarily from these drift chambers, which operate in a virtually field-free region.

The trigger was formed by using a 600 MeV threshold for the calorimeter signal. This high threshold lead to an acceptable nominal trigger rate of 2 kHz. The calorimeter was split into two planes, labeled the pre-shower and the shower. The pre-shower consisted of 54 blocks of 34×8.5 cm^2 blocks of lead glass, arranged in two columns and 27 rows (Fig. 3.11). The shower was made of 189 blocks of 8.5×8.5 cm^2 blocks of lead glass. The sum of photo-multiplier tube (PMT) signals in the calorimeter was used to form the trigger.

The timing plane was made of 13 plastic scintillator panels forming a plane 220×64 cm^2. These were used as high precision timing detectors (resolution of 300ps), and were operated with lower threshold. To prevent being overwhelmed by high rates, the

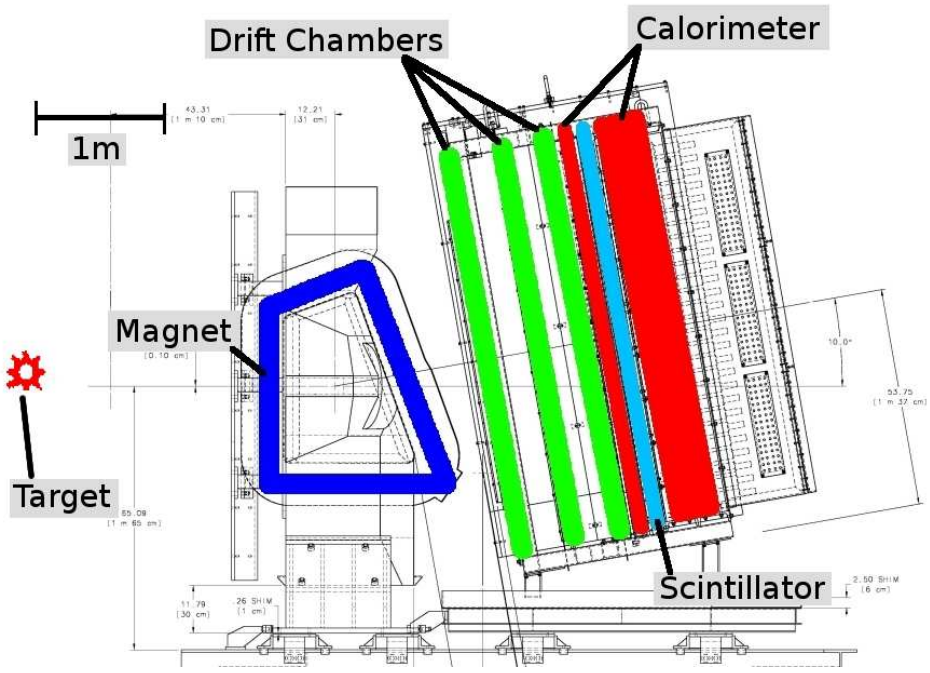

FIG. 3.10: **BigBite Schematic.** Schematic of the detector package used to detect quasi-elastic electrons from E02-013.

paddles were protected from direct view of the target by placing them behind the pre-shower.

Knowledge of the position of the detector was crucial for a proper reconstruction of the scattering angle. In addition to the survey performed by the Jefferson Lab alignment group, a survey was performed by the collaboration [74].

3.4.1 BigBite Magnet

Researchers at NIKHEF built a large non-focusing dipole magnet to serve as a large momentum and angular acceptance spectrometer, BigBite [73]. The magnet was built to take advantage of the full thickness of storage cell targets that were typically 40 cm long. This non-focusing design serves as a compromise between high-resolution focusing dipole spectrometers, which choose resolution over acceptance; and non-magnetic spectrometers, which have resolutions no better than 10% for electrons of energy less than 1

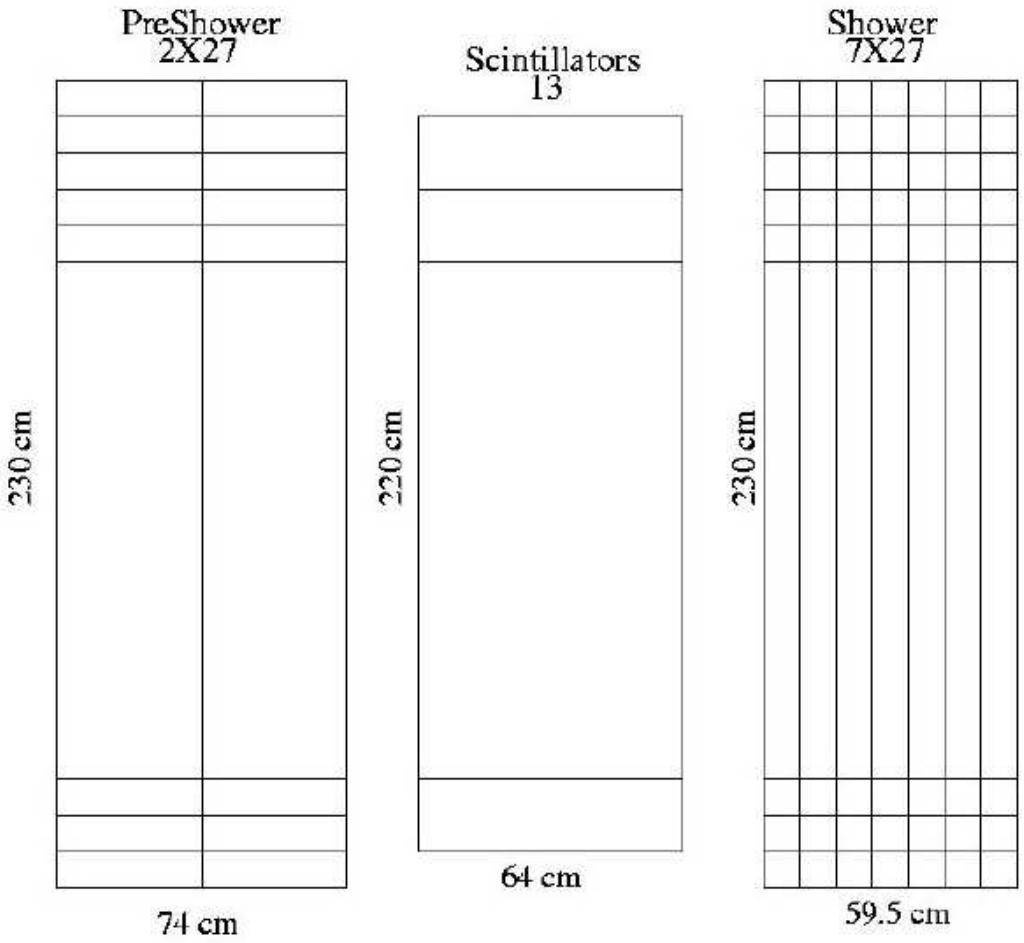

FIG. 3.11: **BigBite Calorimeter Configuration.** The calorimeter consists of a pre-shower, a thin scintillator trigger plane, and a lead glass shower calorimeter.

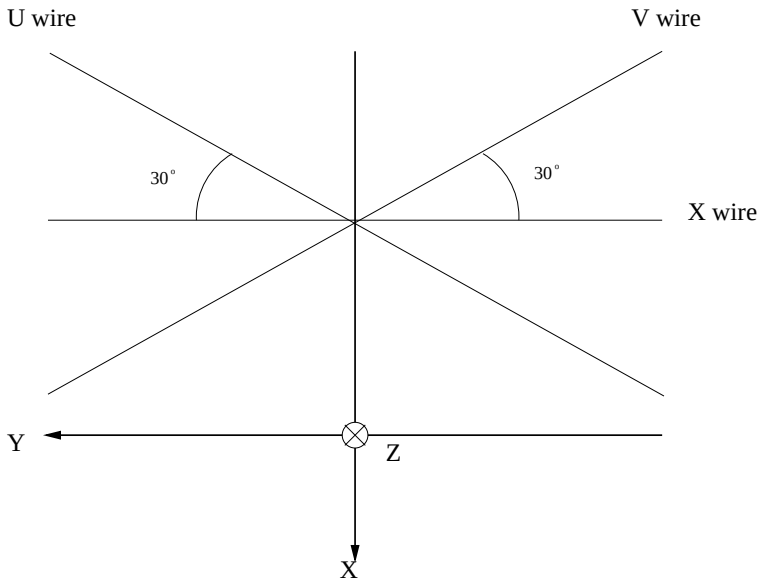

FIG. 3.12: **Wire Plane Orientation for MWDCs.** Wire plane orientation with respect to the detector coordinate axes.

GeV. The magnet was designed to have an acceptance of ± 10cm along the beamline for electrons scattered perpendicular to the symmetry plane of the target.

The magnet is a dipole with a gap of 25 cm. The entrance face is perpendicular to the central trajectory, the exit face has a pole face rotation of 5° [73]. This created a more uniform dispersion across the acceptance, by having a larger field integral for particles entering at the bottom of the acceptance.

3.4.2 Multiple Wire Drift Chambers

In order to aid 2-D track reconstruction in each chamber, the wire chambers had three types of wire orientations: X, U, V. The X wires are parallel to $y_{\rm det}$ axis; V and U are $\pm 30^\circ$ to the $y_{\rm det}$ axis, as seen in Fig 3.12.

Each plane consisted of alternating field wires and sense wires, between cathode planes. Sense wires were separated 1 cm from each other, as seen in Fig. 3.13. The field wires were located between the sense wires with the same 1 cm spacing between field

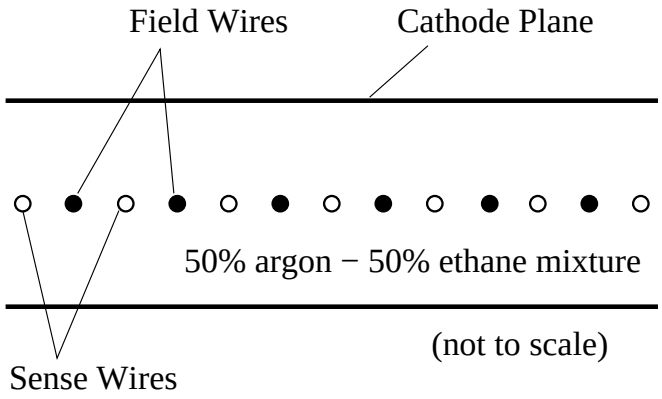

FIG. 3.13: **In-Plane Configuration.** Wire configuration for a single plane in the multiple wire drift chambers; the field wires and the cathode plane were kept at the same potential.

wires. Therefore, there was a spacing of 0.5 cm between any two wires. This configuration was chosen to provide a symmetric field around the sense wires. The chambers are filled with a 50/50 argon/ethane mixture and are held at a pressure slightly greater than atmospheric pressure.

When a charged particle enters the chamber, it ionizes the gas mixture along its path. The ions then drift towards the grounded sense wires. The somewhat rotationally symmetric field makes the drift time insensitive to the direction of the ionized particle, so a drift time can be converted directly to the track minimum distance from the wires.

This experiment required the detection of electrons, but the wire chambers were insensitive to type of charged particle detected. Particle identification is acheived through a combination of electron optics (Sec. 3.4.3) and calorimetry (Sec. 3.4.4).

3.4.3 Electron Optics

The non-focusing dipole magnet was used to determine the momentum of incoming charged particles. In order to properly determine the bend due to the magnetic field, the location of the electron interaction point in the target must also be determined. Both the momentum and the location can then be determined from the track information in the

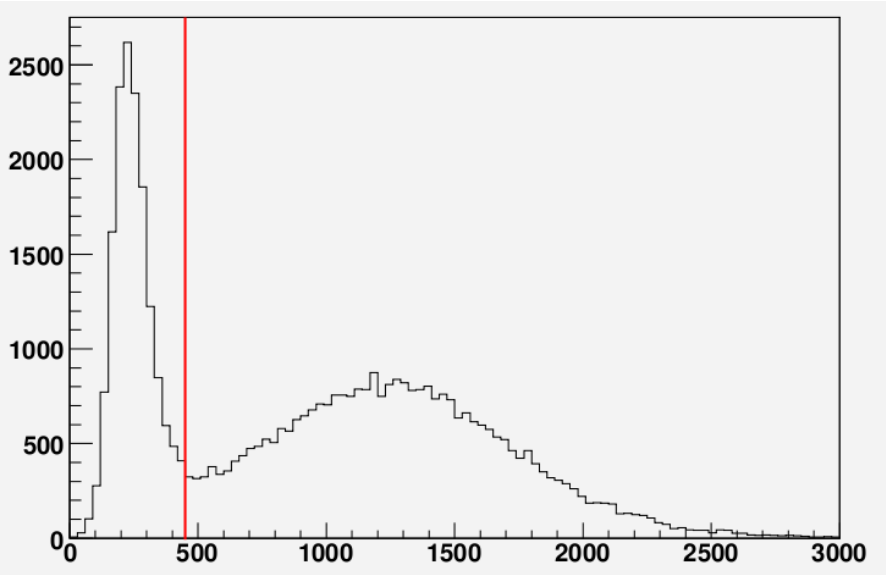

FIG. 3.14: **Pre-shower Particle Identification**. The energy deposited in the pre-shower allows for a clean separation of electrons and negative pions, the cut shown at 450 channels was used to identify electron events.

multiple wire drift chambers.

3.4.4 Calorimetry

The optics information can determine the charge/momentum ratio of the particle. To properly identify the particle, a lead glass array is used to determine the energy of the particle. Particles entering the lead glass blocks produce an electromagnetic shower. The Cherenkov light from this shower was collected from all blocks and the sum of these amplitudes is approximately linear with the energy of the particle. The combination of the shower and pre-shower gives reconstructed energy with a resolution of $\sigma_{dE/E} \approx 10\%$. Information from the pre-shower alone is sufficient to adequately separate electron and pion events, as depicted Fig. 3.14.

The signals from individual shower blocks can be used instead of the summed signals. When this information is combined with the known target location, a rough volume constraining possible tracks is determined. This restricts the possible locations of the

track through the drift chambers by a factor of ten, increasing the speed of the search algorithm [67].

3.4.5 Scintillator

A set of 13 thin scintillator paddles were located between the shower and the pre-shower. They provided the timing information for the electron arm. The paddles have a photomultiplier tube on each end. The timing signal had a resolution of about 300 ps. Association with a track in the drift chambers allows the reconstruction of the time of the electron scattering in the target, and therefore the drift time and path of the electron. This timing information was also used in coincidence with the neutron arm timing information to calculate the time-of-flight for the neutron.

3.5 Neutron Detection

Neutrons were identified in E02-013 by first detecting baryons. Timing information separated particles that did not originate from the target from those that did. Furthermore, this timing information was used to determine the initial momentum of particles that did originate from the target. Finally, charge identification separated neutrons from protons.

Particles were detected in a wall of scintillating material. Layers of dense material (lead and iron) increase the probability of an interaction for both charged and neutral particles. The resulting shower of charged particles provided the signal for an interaction. A cluster of signals from the scintillator was used to determine the location of the interaction.

Two thin layers of scintillator before the conversion layers provided charge information. These veto layers would fire for a charged particle, but there would be no signal from an uncharged particle.

The neutron detector was designed to match the BigBite acceptance, while providing good time-of-flight information for the high velocity neutrons. In addition, it was designed to suppress background and to operate with a high rate (due to the polarized target's high luminosity).

3.5.1 Hadron Time of Flight Spectrometer

The design of the hadron detector was based on two main considerations: precise determination of the particle momentum and an acceptance matching that of BigBite. The former was acheived through a combination of precise timing information ($\delta t < 0.3$ ns) and a long flight path. The latter was matched by making the neutron detector very large.

Momentum resolution, path length, and timing resolution are related as follows:

$$\delta p = \left[\frac{mc\beta^2}{\ell}\left[\frac{1}{(1-\beta^2)^{3/2}}\right]\right]\delta t, \tag{3.3}$$

where δp is the momentum resolution, c is the speed of light, m is the mass of the particle, ℓ is the path length, and β is the velocity of the particle as a fraction of the speed of light: $\beta = \ell/(ct)$. For a given particle velocity and time resolution, a longer flight path results in a finer momentum resolution.

The selected path length is limited by the second design constraint, matching the BigBite spectrometer. Practical considerations for the construction of the detector limit the size of the detector to roughly this size. The final dimensions of $4.2 \times 2.0 \times 6.2$ m^3 (width $\times$ depth $\times$ height)—an active area 11.27 m^2—allowed the neutron detector to be placed 8 m from the target and still subtend nearly 100 msr. This path length, combined with the 300 ps timing resolution provided a momentum resolution of $\delta p = 200$ MeV$/c$ for the highest Q^2 point ($Q^2 = 3.5$ GeV^2, $\beta = 0.95$.)

The neutron detector contained two thin veto planes followed by the neutron-detector planes: seven planes of converter material/scintillator (Fig. 3.15 and Fig. 3.16). The active region of the neutron detectors are 5 or 10 cm thick scintillator bars read out on both

sides, providing a horizontal position as well as precise timing information. The segmentation of the neutron detector planes permits a coarse determination of the neutron's vertical position. The trigger was formed by summing right or left PMT signals across a group of bars. These groups are shown by bars of the same color in Fig. 3.15.

The different kinematic settings required the detector to be moved several times. To minimize downtime, shielding and electronics were localized on the detector. This allowed the entire structure of detector, electronics, and shielding to be moved within 2 hours [75].

3.5.2 Charged Particle Veto

Due to the large number of protons emerging from the target, special attention was paid to the design and implementation of the veto counters. Each veto plane was composed of independent left-and-right scintillators read out on one end, with a total of $48 \times 2 = 96$ detectors per plane. This left-right segmentation served to minimize the counting rate on the phototubes. To further reduce the rate, shielding was placed in front of the veto counters. The thickness of the lead shielding was optimized by Monte Carlo simulations. The use of sheilding may have contributed to the conversion of neutrons to protons (and protons to neutrons). This possibly was accounted for by comparing the ratio of uncharged to charged events from different targets and is detailed in Sec. 5.6.

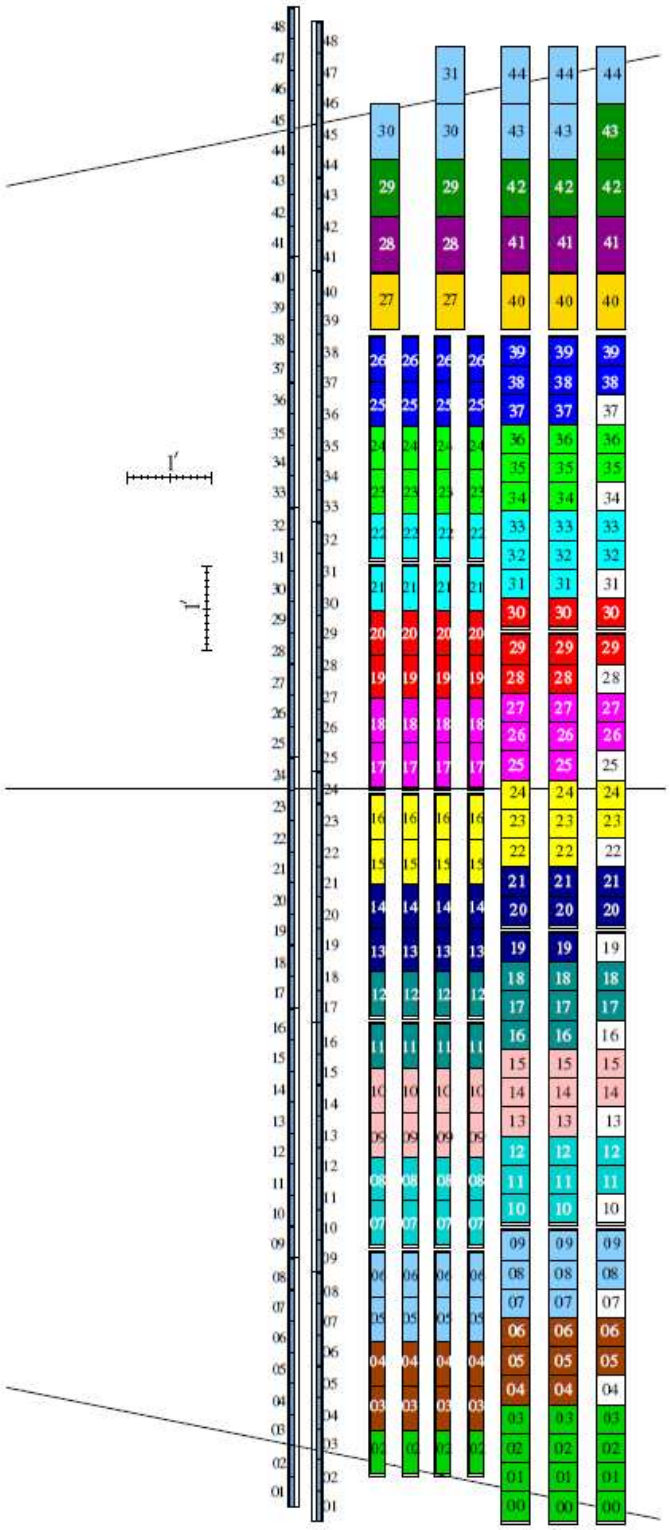

FIG. 3.15: **Diagram of Neutron Detector.** The neutron detector consisted of layers of converting material and scintillating material. The first two layers formed the veto detector. The different colored bars correspond to different trigger sums.

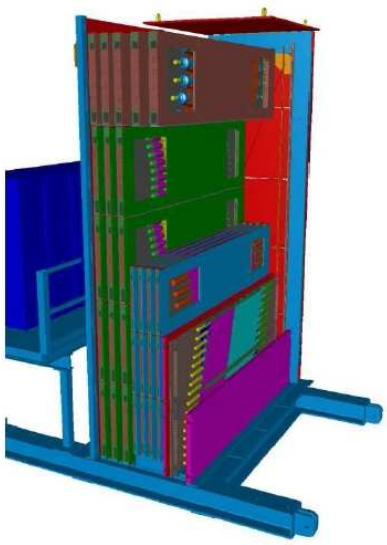

FIG. 3.16: **Drawing of Neutron Detector.** Design drawing of the neutron detector showing the layers of scintillating material and cassette structure.

CHAPTER 4

Target

4.1 ^{3}He as an Effective Polarized Neutron Target

This experiment required polarized electrons scattering from polarized neutrons. The ideal target for this experiment is a dense gas of free neutrons. However, this is impractical for several reasons, primary among them is the short lifetime of the free neutron (885.7 $\pm$ 0.8 s [76]). In order to achieve the luminosity required to make a precise measurement of the asymmetry, neutrons in light nuclei are used as an effective stand-in for free neutrons. For recoil polarimetry measurements, which require a neutron polarimeter, deuterium is often used. The ^{3}He nucleus is ideal for measurements using a polarized target.

A decomposition of the ^{3}He ground state wave function yields a small contribution from the P-wave, approximately 10% D-wave contribution, and the rest in S-wave [77]. In the space-symmetric S-wave of the polarized ^{3}He nucleus, the protons are in a spin-singlet state due to the Pauli exclusion principle. Therefore, their magnetic moments cancel out, and the magnetic moment of the ^{3}He nucleus is nearly equal to the free neutron magnetic moment. The contribution of the P-wave is small enough to essentially ignore.

The effect of the S' and D states can be handled in the analysis of the experiment (see Chapter 5). For E02-013, we restricted the initial momentum of the detected neutron, preferentially selecting the S-wave, which is 100% polarized.

Polarized ^{3}He targets have been used as effective polarized neutron targets since the experiments at SLAC (E142 [78] and E154 [79]). At Jefferson Lab, the ^{3}He polarized target has been used successfully in six experiments prior to E02-013 [80, 81, 82, 83, 84]. Since E02-013 ended, the polarized target has been used for seven more experiments in Hall A that ran in 2009 [85, 86, 87, 88, 89, 90, 91].

In general, there are two methods of polarizing ^{3}He which are widely used: direct optical pumping of the ^{3}He meta-stable state and optical pumping of an alkali vapor which spin-exchanges with the ^{3}He nucleus.

4.1.1 Spin-Exchange Optical Pumping

The term spin-exchange optical pumping (SEOP) refers to a two-step process. First an alkali metal atom is optically pumped, and quickly polarized. Second, that polarized alkali metal atom spin-exchanges with a noble gas nucleus (for our experiment, ^{3}He).

Optical Pumping

Optical pumping is the polarization of an alkali metal by placing the metal in a magnetic field and exciting it with circularly polarized light. Due to the angular momentum selection rules, the alkali metal quickly becomes polarized. For this experiment, rubidium is optically pumped. Other alkali metals can be used, but rubidium has several practical benefits (lower vapor temperature and larger Zeeman splitting) which makes it the preferred alkali metal for the Jefferson Lab target.

Ignoring the spin of the Rb nucleus, the Rb atom can be excited from the $5S_{1/2}$, $m = -1/2$ state to the $5P_{1/2}$, $m = 1/2$ by right circularly polarized laser light of the

correct wavelength (795 nm), as in Fig. 4.1. The atom can now spontaneously decay, emitting a photon which may reduce the optical pumping efficiency. At Jefferson Lab, a small amount of nitrogen gas is added to the sample. As a diatomic molecule, nitrogen has vibrational and rotational degrees of freedom to absorb energy and enables radiationless decay of the atoms. Using measured quenching cross sections [92], the radiationless quenching time of the excited state is estimated to be 1.3 ns, which is much shorter than the radiative decay time of 28 ns. Therefore only 5% of excited atoms emit a photon [93]. Due to collisional mixing of Rb atoms, the atom can decay to either the $5S_{1/2}$, $m = -1/2$ or $m = 1/2$. By using only right circularly polarized light, the atom cannot be excited from the $5S_{1/2}$, $m = 1/2$ state. By continually pumping with right circularly polarized light, the alkali sample quickly becomes highly polarized.

However, this picture is muddied by the hyper-fine interaction due to the non-zero nuclear spin of the Rb atom. The hyper-fine splitting is larger than the Zeeman splitting at the holding fields used at Jefferson Lab ($\approx$ 25 G). Therefore, the electrons are in eigenstates of the total spin $F = I + S$, where I is the nuclear spin ($I = 5/2$ for ^{85}Rb) and S is the electron spin. As in the simpler $I = 0$ example, there is a state ($F = 3$, $m_F = 3$) from which the electrons cannot be excited, so the Rb becomes quickly polarized, although they must go through more excitation cycles before becoming polarized [93].

Spin-Exchange

In rubidium optical pumping experiments using ^{3}He as a buffer gas (similar to Jefferson Lab's use of nitrogen), it was discovered that Rb and ^{3}He would spin-exchange, resulting in a polarization of the ^{3}He gas [94]. Spin-exchange occurs through a hyperfine interaction characterized by the magnetic dipole interaction

$$H_{SE} = \alpha \mathrm{K}^{\mathrm{He}} \cdot \mathrm{S}^{\mathrm{Rb}}, \tag{4.1}$$

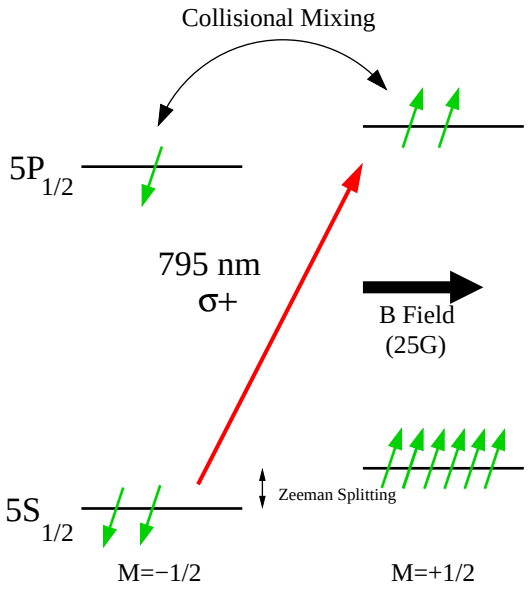

FIG. 4.1: **Optical Pumping.** Simplified description of optical pumping, neglecting nuclear spin.

where K^{He} is the ^{3}He nuclear spin and S^{Rb} is the Rb electron spin. The coupling function, α is a function of the internuclear separation of the Rb-He pair. The interaction is dominated by the Fermi-contact interaction:

$$\alpha(R) = \frac{16\pi}{3}\frac{\mu_B\mu_K}{K}\left|\psi(R)\right|^2 \tag{4.2}$$

where μ_B is the Bohr magneton, μ_K is the magnetic moment of the noble-gas nucleus and $\psi(R)$ is the wave function of the alkali-metal valence electron evaluated at the position of the noble-gas nucleus [95]. This wave function includes an enhancement to the alkali-metal valence electron wave function in the presence of noble gases. This enhancement comes from the large kinetic energy acquired by the electron as it scatters in the core potential of the noble gas atom [96, 97].

The spin-exchange for ^{3}He is dominated by binary collisions described above. For heavier noble gases, the spin-exchange has a large contribution from van der Waals molecules. This can be suppressed by a large magnetic field (a few hundred Gauss) [9].

Spin Relaxation

In addition to spin-exchange interactions, which polarize the noble gas, there are interactions which can limit the total polarization.

The first is an anisotropic hyperfine interaction. The isotropic hyperfine interaction between the alkali metal electron and the noble gas nucleus transfers the polarization to the noble gas. The anisotropic magnetic-dipole coupling polarizes in the opposite direction to compensate for the excess angular momentum [9].

Spin-relaxation can also come from the spin-rotation interaction which transfers polarization from the electron spin to the translation degrees of freedom. For the light noble gas nuclei this interaction is primarily due to the alkali-metal core [9].

Spin-relaxation in the alkali metal can also occur through the collisions of spin-polarized alkali-metal atoms. The Rb-Rb spin destruction cross section is very large (1.5×10^{-17} cm^2).

4.1.2 Hybrid Spin Exchange Optical Pumping

This experiment was the first to take advantage of the greatest step forward in SEOP in recent years: hybrid alkali pumping [13, 98].

The polarized targets at Jefferson Lab have relied on the spin exchange between polarized Rb and ^{3}He. However, this is primarily due to the commercial availability of high powered lasers tuned to the Rb $5S_{1/2} \rightarrow 5P_{1/2}$ D_1 transition (795nm). In fact, greater spin-exchange photon efficiencies can be achieved with other alkali-metals. Photon efficiency, η_γ, is defined to be the number of polarized nuclei produced per photon absorbed in the vapor. A near 100% efficiency is predicted from Na-^{3}He [9]. Experimental measurements of K-^{3}He demonstrate a 10 times improvement in spin-exchange efficiency for K-^{3}He over Rb-^{3}He at temperatures ranging from 400 to 460 K [10], see Fig. 4.2. Stated in other terms, approximately 50 photons are required to produce a single polarized ^{3}He

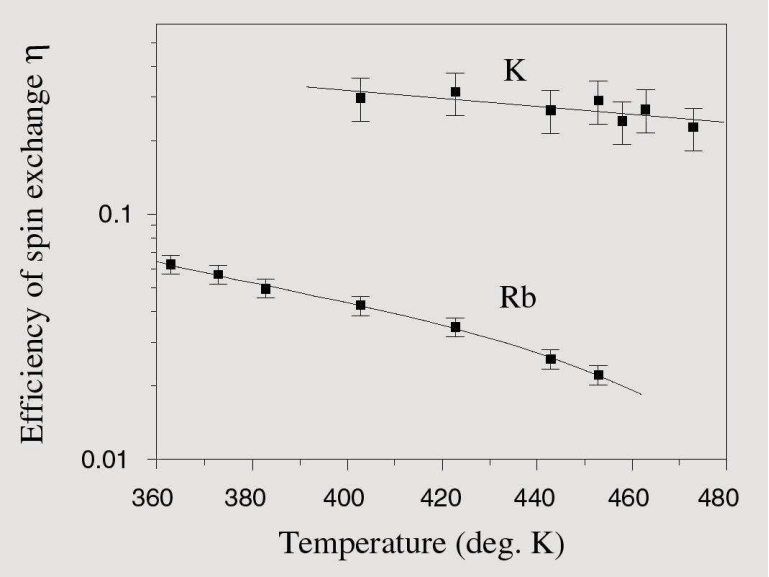

FIG. 4.2: **Spin-Exchange Efficiencies for ^{3}He-Rb and ^{3}He-K.** Over a range in temperatures, the spin efficiency of ^{3}He-K is an order of magnitude larger than for ^{3}He-Rb. Figure from [10].

.

nucleus when using Rb-^{3}He SEOP, but only 4 photons are required for K-^{3}He.

However, there is still no source of commercially available lasers of sufficient power and narrow linewidth to polarize K for an electron target. A method of hybrid polarization may be adopted to achieve high polarizations [98]. The method involves a mixture of Rb and K vapors. The spin-exchange cross section between the two alkali-metals is very large, and the spin-exchange rate is over 200 times faster than the typical spin-relaxation rates [11]. Therefore, the K vapor has an electron polarization equal to the Rb vapor electron polarization.

The rate of helium polarization is:

$$\frac{dP_{\rm He}}{dt} = \gamma_{\rm SE}(P_{\rm A} - P_{\rm He}) - \gamma_{\rm He}P_{\rm He}, \tag{4.3}$$

where $\gamma_{\rm SE} = k_{\rm K}[{\rm K}] + k_{\rm Rb}[{\rm Rb}]$, $k_{\rm K}$ and $k_{\rm Rb}$ are the spin-exchange constants, $P_{\rm A}$ is the alkali polarization (identical for K and Rb) and $\gamma_{\rm He}$ is the spin lost by ^{3}He through relaxation.

The effective spin relaxation rate for Rb is modified to account for the presence of

K:

$$\Gamma'_{\mathrm{Rb}} = \Gamma_{\mathrm{Rb}} + D\Gamma_{\mathrm{K}} + q_{\mathrm{KR}}[K], \tag{4.4}$$

where Γ_{Rb} is the spin-relaxation rate for Rb, D is the ratio of the alkali metal densities, $D = [K]/[Rb]$, Γ_K is the spin-relaxation rate for K, and q_{KR} is the K-Rb loss rate (taken to be small for most conditions of interest).

Spin-exchange efficiency, η_{SE}, is the ratio of the rate at which angular momentum is transferred to the ^{3}He, and under ideal conditions, $\eta_\gamma = \eta_{\mathrm{SE}}$. The typical expression for spin-exchange efficiency can be modified to include the effect of having two alkali-metals,

$$\eta_{\mathrm{SE}} = \frac{\gamma_{\mathrm{SE}}\,[^3\mathrm{He}]}{[\mathrm{Rb}]\,\Gamma'_{\mathrm{Rb}}} = \frac{(k_{\mathrm{Rb}} + Dk_{\mathrm{K}})[^3\mathrm{He}]}{\Gamma_{\mathrm{Rb}} + D\Gamma_{\mathrm{K}} + q_{\mathrm{KR}}[\mathrm{K}]} \tag{4.5}$$

The spin-exchange constants have been measured, $k_{\mathrm{K}} = (6.1 \pm 0.4) \times 10^{-20}$ cm^3/s and $k_{\mathrm{Rb}} = (6.8 \pm 0.2) \times 10^{-20}$ cm^3/s [99]. The relative closeness of these values indicates that improved spin-exchange efficiency is not due to an enhancement of the spin-exchange rate, but rather a decrease in the spin-relaxation rate.

4.2 Magnetic Field

4.2.1 Field Requirements

The magnetic field for this experiment was constrained by several considerations. First, the strength of the field must be large enough to successfully polarize the ^{3}He and measure that polarization. On the other hand, the total field integral must be small enough that the incident electron beam is not deflected from the beam dump. For E02-013, a 25G holding field was used.

Finally, the field must be sufficiently uniform. The uniformity is required to minimize two depolarization effects. The first is the relaxation time due to field inhomogeneity. This effect is somewhat mitigated by the constant optical pumping. Because of the

constant optical pumping, this effect manifests itself in the form of a limit on polarization. From previous measurements, it was determined that no effect was seen if the field gradient was kept below 100 mG/cm. The hybrid-alkali mixture provided a much faster rate of polarization, making this experiment less sensitive to this effect than earlier Jefferson Lab polarized ^{3}He experiments.

There is also a prompt effect due to NMR measurements. The signature of this effect is a depolarization evident in back-to-back measurements. During an NMR measurement, the nuclear spins of ^{3}He change direction, and are then returned through a process known as Adiabatic Fast-Passage. Field gradients of 20mG/cm can produce depolarizations of approximately 1% per measurement.

4.2.2 Magnetic Field Box

The distinguishing feature of previous ^{3}He targets was a set of Helmholtz coils. For this experiment, the coils were not present. In their place was a large iron box. This box served as a shield for the fringe fields coming from BigBite. The box had 4 sets of 2 coils (8 total) wrapped around the sides of the iron box. They were arranged in such a way to produce a field in the iron that resulted in a uniform field across the target region. An overhead schematic is presented in Fig. 4.3

4.2.3 Induction Enhanced by Iron Core

A major concern in using coils wrapped around an iron box to generate the magnetic field used to polarize the target was the possibility of a non-linearity in the field ramp used to produce the spin flip required to measure the polarization. It was assumed that the non-linearity would be due to hysteresis in the iron. Careful measurements of the magnetic field using a Hall probe were made to investigate this possibility. The tests showed a linear “up sweep,” and a “down sweep” with minor variations from linearity. In short, no

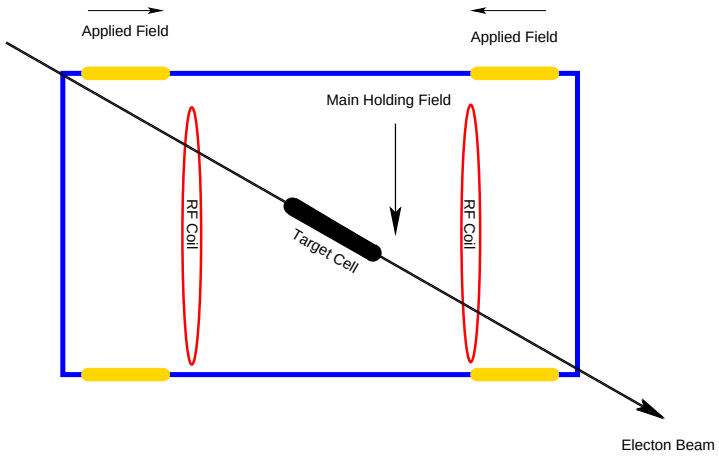

FIG. 4.3: **Schematic of Target Holding Field.** Overhead view of target box showing placement of coils and the location of the resulting uniform field.

hysteresis effects were observed.

When the linearity was checked, it was assumed that the dominant contribution to any non-linearity would be from the hysteresis. The field was stepped, a measurement was made, and the field was stepped again. This would be sufficient to detect hysteresis effects, but not time dependent effects. In the course of running the experiment, a time dependent effect was discovered.[1]

In order to perform an AFP NMR measurement (see section 4.6.1), the field must be swept from a low to high field value and back again. In other words, during the AFP NMR measurement, the field is time dependent. A pronounced lag can be noticed between the voltage sent to the coils and the field produced. Investigations of this effect indicate that is due to the inductance of the coils. This inductance is small for open core coils, but becomes large when iron is introduced into the coils, as is the case for E02-013.

[1]The work in this section was performed by the author and J. Singh of the University of Virginia, `js7uq@virginia.edu`

The control voltage for the field is determined by the simple relationship:

$$B(t) = \alpha V(t) + \beta \tag{4.6}$$

where $B = |\vec{B}|$ is the magnitude of the magnetic field, and α and β are constants to be determined experimentally, from exactly the tests that were used to check for linearity. When the field sweep for the magnet box was calibrated, a variation from the expected value was observed. It became impossible to reconcile the results from the earlier tests with the observations of the time of the sweep and the maximum field.

In Eq. 4.6, the standard DC Ohm's law is assumed, as the change in applied voltage is considered slow enough to allow this approximation. Of course, the complete form of the voltage for an LR series circuit is given by:

$$V(t) = I(t)R + L\frac{dI}{dt} \tag{4.7}$$

Again, in previous experiments it was assumed that the change in current was sufficiently slow to ignore the inductive term.

For this experiment the basic set-up was modified by the addition of the iron in the circuit. In that case, the DC magnetic permeability of the iron is 2-3 orders of magnitude larger than that of air. This is a boost to the inductance. The rate of change of the current is still small, but the product of the rate of change and the inductance is now significant.

It is useful to define a time constant, τ, such that:

$$\frac{V(t)}{R} = I(t) + \tau\frac{dI}{dt} \tag{4.8}$$

We can solve this equation by treating the current as the product of two functions:

$$I(t) = f(t)g(t) \tag{4.9}$$

$$I' = fg' + f'g \tag{4.10}$$

The equation can then be written as:

$$\frac{V}{fgR} = 1 + \tau\frac{f'}{f} + \tau\frac{g'}{g} \tag{4.11}$$

Since g and g' are arbitrary functions, and will be multiplied by another function, we can arbitrarily fix the relationship.

$$\tau\frac{g'}{g} + 1 = 0 \tag{4.12}$$

The result of this choice is a decaying exponential (what we would naively expect from the solution in the $I_0 = 0$ case).

$$\frac{dg(t)}{dt} = -\frac{g}{\tau} \tag{4.13}$$

$$g(t) = g(0)e^{-\frac{t}{\tau}} \tag{4.14}$$

What is left is to solve for f and f':

$$\frac{V}{fgR} = \tau\frac{f'}{f} \tag{4.15}$$

$$f' = \frac{V}{gR\tau} \tag{4.16}$$

$$\frac{df(u)}{du} = \frac{V(u)}{g(u)R\tau} \tag{4.17}$$

$$f(u) = \frac{1}{R\tau}\int\frac{V(u)}{g(u)}du \tag{4.18}$$

$$= \frac{1}{R\tau g(0)}\int V(u)e^{\frac{u}{\tau}}du \tag{4.19}$$

With these functions determined, the current can be written:

$$I(t) = f(t)g(t) \tag{4.20}$$

$$= g(0)e^{-\frac{t}{\tau}}\frac{1}{R\tau g(0)}\int V(u)e^{\frac{u}{\tau}}du \tag{4.21}$$

$$= \frac{1}{R\tau}\int_{-\infty}^{t} V(u)e^{\frac{u-t}{\tau}}du \tag{4.22}$$

In our "current sweep" the resistance is assumed to be constant; the power supply is actually sweeping the voltage. The voltage sweep is symmetric and triangular—ranging from time $-T$ to $+T$, with a maximum at $t = 0$.

$$V(t) = \begin{cases} V_1 = V_0 & t \leq -T \\ V_2 = V_0 + V_A\left(1 + \frac{t}{T}\right) & -T \leq t \leq 0 \\ V_3 = V_0 + V_A\left(1 - \frac{t}{T}\right) & 0 \leq t \leq +T \\ V_4 = V_0 & t \geq +T \end{cases}$$

Similarly, the current is a continuous piecewise function:

$$I_1 = I(t \leq -T) = \frac{1}{R\tau}\left[\int_{-\infty}^{t} V_1(u) e^{\frac{u-t}{\tau}} du\right] \tag{4.23}$$

$$I_2 = I(-T \leq t \leq 0) = \frac{1}{R\tau}\left[\int_{-\infty}^{-T} V_1(u) e^{\frac{u-t}{\tau}} du + \int_{-T}^{t} V_2(u) e^{\frac{u-t}{\tau}} du\right] \tag{4.24}$$

$$I_3 = I(0 \leq t \leq +T) = \frac{1}{R\tau}\left[\int_{-\infty}^{-T} V_1(u) e^{\frac{u-t}{\tau}} du + \int_{-T}^{0} V_2(u) e^{\frac{u-t}{\tau}} du + \int_{0}^{t} V_3(u) e^{\frac{u-t}{\tau}} du\right] \tag{4.25}$$

$$I_4 = I(t \geq +T) = \frac{1}{R\tau}\left[\int_{-\infty}^{-T} V_1(u) e^{\frac{u-t}{\tau}} du + \int_{-T}^{0} V_2(u) e^{\frac{u-t}{\tau}} du + \int_{0}^{+T} V_3(u) e^{\frac{u-t}{\tau}} du + \int_{+T}^{t} V_4(u) e^{\frac{u-t}{\tau}} du\right] \tag{4.26}$$

For the first section:

$$I_1(t) = \frac{1}{R\tau}\left[\int_{-\infty}^{t} V_0 e^{\frac{u-t}{\tau}} du\right] = \frac{V_0}{R} \tag{4.27}$$

For the second section:

$$\begin{aligned} I_2(t) &= \frac{1}{R\tau}\left[\int_{-\infty}^{-T} V_0 e^{\frac{u-t}{\tau}}du + \int_{-T}^{t}\left(V_0 + V_A\left(1+\frac{u}{T}\right)\right)e^{\frac{u-t}{\tau}}du\right] \\ &= \frac{1}{R}\left[V_0 + V_A\left(1+\frac{t}{T}\right)\right] - \frac{V_A\tau}{RT}\left[1-e^{\frac{-T-t}{\tau}}\right] \end{aligned} \tag{4.28}$$

For the third section:

$$\begin{aligned} I_3(t) &= \frac{1}{R\tau}\left[\int_{-\infty}^{-T} V_0 e^{\frac{u-t}{\tau}}du + \int_{-T}^{0}\left(V_0 + V_A\left(1+\frac{u}{T}\right)\right)e^{\frac{u-t}{\tau}}du\right. \\ &= \frac{1}{R}\left[V_0 + V_A\left(1-\frac{t}{T}\right)\right] + \frac{V_A\tau}{RT}\left[e^{\frac{T-t}{\tau}} - 2e^{-\frac{t}{\tau}} + e^{\frac{-T-t}{\tau}}\right] \end{aligned} \tag{4.29}$$

Overall, the current can be written in terms of the DC solution and a dynamic term. The dynamic term can be written proportional to the "lag time" function $l(t)$:

$$I(t) = \frac{V(t)}{R} + \frac{V_A\tau}{RT}l(t) \tag{4.30}$$

This "lag time" function is piecewise continuous:

$$l(t) = \begin{cases} 0 & t \le -T \\ -1 + e^{\frac{-T-t}{\tau}} & -T \le t \le 0 \\ 1 - 2e^{-\frac{t}{\tau}} + e^{\frac{-T-t}{\tau}} & 0 \le t \le +T \\ e^{\frac{T-t}{\tau}} - 2e^{-\frac{t}{\tau}} + e^{\frac{-T-t}{\tau}} & t \ge +T \end{cases} \tag{4.31}$$

Results for different values of τ have been plotted in Fig. 4.4.

In principle, the corrections to the NMR sweep could be calculated by measuring or calculating V_A, L, and R. In addition, a plot of the magnetic field versus time during a sweep could be made, and then fit with this function. However, there may be difficulty in fitting to a discontinuous function. Another way exists and is the method used for this experiment.

For this method, we first investigate the effect of a step function in the voltage on the current. We use the voltage step function:

$$V(t) = \begin{cases} V_0 & t \le 0 \\ V_0 + V_A & t \ge 0 \end{cases} \tag{4.32}$$

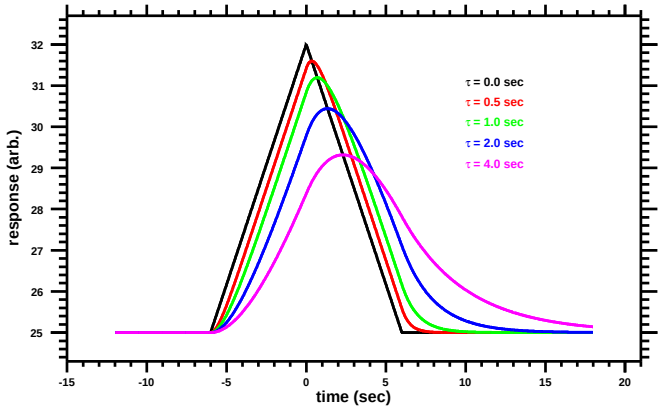

FIG. 4.4: **Decay Constant.** A stable magnetic field is disconnected from a current, the resulting decay is used as a measurement of the ratio L/R.

The current is therefore:

$$I_1 = I(t \leq 0) = \frac{1}{R\tau}\int_{\infty}^{0} V_0 e^{\frac{u-t}{\tau}}\,du \tag{4.33}$$

$$I_2 = I(t \geq 0) = \frac{1}{R\tau}\int_{\infty}^{0} V_0 e^{\frac{u-t}{\tau}}\,du + \frac{1}{R\tau}\int_{0}^{t} (V_0 + V_A)\, e^{\frac{u-t}{\tau}}\,du \tag{4.34}$$

This gives:

$$I_1 = \frac{V_0}{R} \tag{4.35}$$

$$I_2 = \frac{V_0 + V_A}{R} - \frac{V_A}{R}e^{-\frac{t}{\tau}} \tag{4.36}$$

Similarly to the ramping case, this can be written in terms of a DC term and a term containing a "lag time":

$$I(t) = \frac{V(t)}{R} + \frac{V_A}{R}e^{-\frac{t}{\tau}} \tag{4.37}$$

So, the deviation from an ideal step function is parametrized by this "lag time" function.

$$l(t) = \begin{cases} 0 & t \leq 0 \\ -e^{-\frac{t}{\tau}} & t \geq 0 \end{cases} \tag{4.38}$$

In the laboratory, this results in a simple manner of measuring τ. A power supply can hold the current at a nominal level (corresponding to V_0). While measuring the magnetic

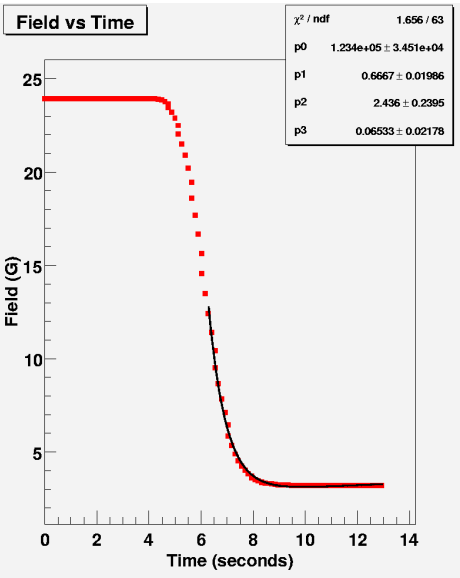

FIG. 4.5: **Magnetic Lag Decay Constant.** A stable magnetic field is disconnected from a current, the resulting decay is used as a measurement of the ratio L/R.

field, the power supply can be switched off (corresponding to an instantaneous $V_A = -V_0$). In such a case, the equation for the current (and corresponding magnetic field) is:

$$I(t) = \frac{V_0}{R} e^{-\frac{t}{\tau}}, \tag{4.39}$$

which is much easier to reliably fit. An example of such a fit is Fig. 4.5.

This time lag in the magnetic field due to the enhanced induction has no effect on the target polarization numbers presented. The lag results in a line shaping effect, but it will be the same for both the NMR measurements used to extract a polarization constant and the NMR measurements used to monitor the polarization. Analysis of NMR signals used demonstrate that this effect is consistent. This line shaping effect will have an overall effect on the error due to the fit for each NMR measurement. However, this uncertainty is small compared to the uncertainty due to the calibration constant (roughly 0.6% vs. roughly 4.5%).

4.3 Polarized Laser Light

Optical pumping requires a source of polarized light of the correct wavelength. In Hall A, this light is provided by lasers of 795nm[2] These laser diodes are coupled to optical fibers. The light emerges from these fibers unpolarized: in a mixture of S and P polarization states. After passing through a collimating lens, the light hits a beam splitting cube. P-wave light passes through the cube, S-wave light is reflected 90° to the path of the beam. The S-wave light passes through a quarter-wave plate, is then reflected from a flat mirror, and passes through the quarter-wave plate again. The result of these two passes is that the light is now in the P-wave state and passes back through the beam splitter. At this point, the light from the fiber has produced two beams of P-wave light. Each of these beams pass though a quarter-wave plate, resulting in two beams of circularly polarized light. Both right- and left-circularly polarized light can polarize the Rb, however, both beams must be polarized with the same handedness to accumulate polarization. A schematic can be seen in Fig.4.6.

In previous Hall A and SLAC experiments using a polarized ^{3}He target, the laser light was directly transferred from an array of lasers, through the polarizing optics, to the cell. This lead to experimental design constraints due to the requirement of a separate building in the experimental hall. The separate structure was required for laser safety considerations, and to shield lasers from ionizing radiation.

This experiment used 75 m optical fibers to bring 150 W of laser light to the target (by using 5 fibers, each transporting 30 W). The light was brought to the polarizing optics near the target through five optical fibers and a 5–1 combiner. The use of these high powered fibers eliminated the need for a separate structure in the experimental hall, allowed lasers to be operated outside the experimental hall, and will, in the future, allow for even more flexible designs.

[2]FAP System purchased from Coherent, Inc. 5100 Patrick Henry Drive, Santa Clara, California 95054

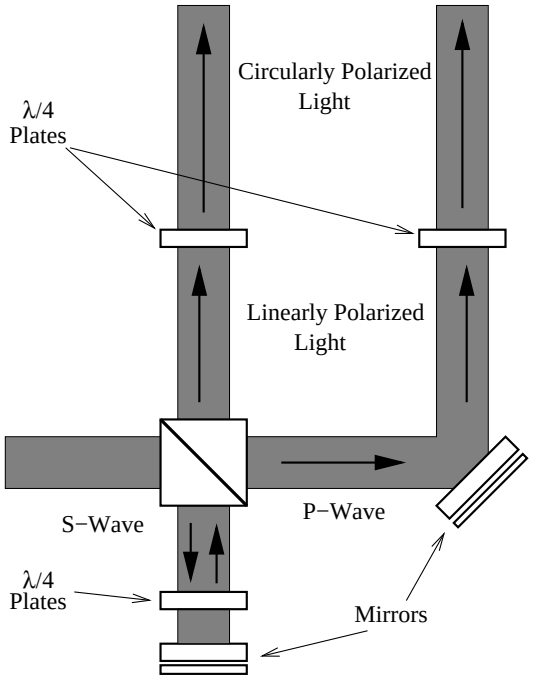

FIG. 4.6: **Polarizing Optics.** Schematic of optics set-up used to convert unpolarized light into right circularly polarized light to polarize Rb vapor

4.4 Target Oven

Once it became clear that the experiment would benefit from using hybrid target cells, the design for the target oven was modified. In a cell that uses rubidium only for spin-exchange, a temperature of 170°C was sufficient to achieve a desirable alkali vapor density. In a cell that uses a mixture of rubidium and potassium, a temperature of at least 230°C was required to achieve a sufficient potassium vapor density to benefit from its addition to the cell.

There was a concern about using the materials similar to previous ovens at high temperatures, above about 200°C. A metal oven would have reached the higher temperatures, but was not considered due to possible effects on both the holding field and the applied RF field. The precision position requirements of both an electron scattering experiment and nuclear polarimetry meant that if a ceramic was used, it should be machinable, and

not something that was formed and later fired, since such materials tend to change shape slightly in the firing process.

The final design was a mixture of a machinable glass sold under the name Macor, and a machinable glass mica. The two materials were chosen for different parts of the oven due to the relative strengths and weaknesses of the materials. In areas where precision was a strict requirement (location of target ladder, location of oven with respect to the support structure, and the NMR pickup coils) Macor was used. The glass mica is a brittle material and flakes off under certain stresses. For the parts of the oven that did not require such a high level of precision the machinable glass mica was used to save both weight and costs.

4.5 Target Cell

The heart of the target system is the target cell. The target cell contains the ^{3}He gas, the alkali mixture and the nitrogen buffer gas. The target cell has three sections: the pumping chamber where the polarized laser light interacts with the alkali metals, and the polarized metal vapor spin-exchanges with the ^{3}He gas; the transfer tube, which separates the two main chambers and allows the pumping chamber to be held at a much higher temperature than the target chamber; and the target chamber, where the electron beam interacts with the polarized ^{3}He gas. A photograph of one of the cells, Anna, is included as Fig. 4.7.

The entire target cell is made of handblown glass. The cell is filled with roughly 8 atm at room temperature of ^{3}He gas, a small quantity of N_2 gas, and the alkali metal mixture, and sealed.

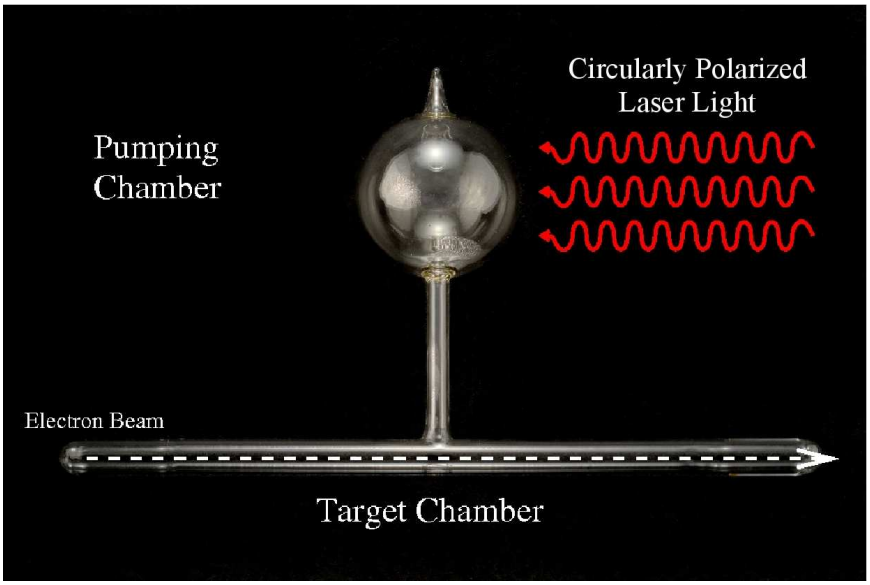

FIG. 4.7: **Target Cell.**The target cell has three sections: pumping chamber, transfer tube, and target chamber.

4.5.1 Construction of Cell

The cells are constructed of GE180 aluminosilicate glass. For E02-013, a longer transfer tube was used to accommodate the target oven design. Two styles of cells were prepared for the experiment. The first had a pumping chamber similar in volume to the target cells used in previous polarized ^{3}He experiments. The second style had a much larger pumping chamber (approximately three times larger volume), but a similar sized transfer tube and target chamber. The larger pumping chamber volume was used in an attempt to make the cells less sensitive to depolarization due to ionization of ^{3}He by the electron beam.

The cells were prepared in the Princeton University glassblowing shop by Mike Souza, who did the pioneering work for the SLAC experiments and has been involved with every polarized ^{3}He experiment performed at Jefferson Lab.

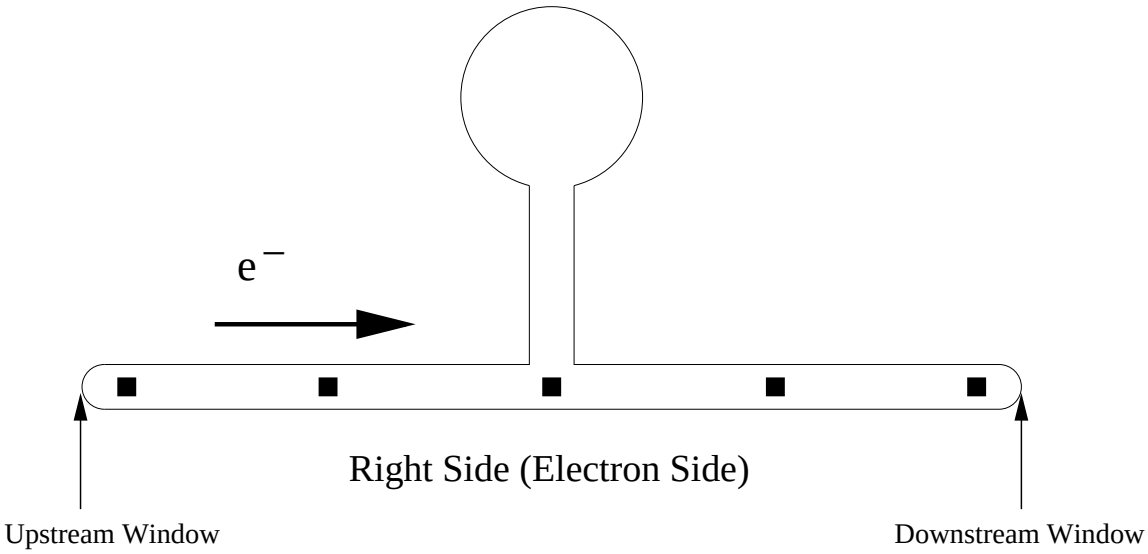

FIG. 4.8: **Location of Thickness Measurements.** Black squares show the approximate location of cell thickness measurements.

4.5.2 Cell Thicknesses

The cells are prepared with tight tolerances, but due to the nature of glassblowing, variations can occur. Since a charged particle traveling through a material such as glass may lose energy due to processes such as Bremsstralung radiation, care must be taken to accurately measure the thickness of the glass cell so that this effect can be properly accounted.

In order to aid in the interpretation of physics data, cell wall thicknesses for all cells used are included as Tables 4.1-4.5. The approximate location of the measurements can be seen in Figure 4.8.

4.5.3 Filling the Cell

Once the cells were prepared by the glassblower, they were shipped to either the College of William & Mary or the University of Virginia to be filled with ^{3}He, N_2, and K-Rb mixture.

Right/Left	From	Distance (cm)	Thickness (mm)
n/a	Upstream	0	0.131
Left	Upstream	3.0	1.42
		13.2	1.59
Neutron		19.2	1.59
Side	Downstream	12	1.62
		2.7	1.66
		Average	**1.57**
Right	Upstream	2.7	1.74
		14	1.77
Electron	Downstream	19.5	1.70
Side		11	1.66
		3.3	1.58
		Average	**1.69**
n/a	Downstream	0	0.127

TABLE 4.1: **Cell Wall Thicknesses – Anna.** This cell was used in the target commissioning studies, before beam was turned on.

Right/Left	From	Distance (cm)	Thickness (mm)
n/a	Upstream	0	0.151
Left	Upstream	3.1	1.60
		12.2	1.63
Neutron		20.9	1.60
Side	Downstream	12.5	1.64
		3.8	1.47
		Average	**1.59**
Right	Upstream	2.2	1.52
		12	1.71
Electon	Downstream	19.3	1.77
Side		12	1.76
		3.0	1.62
		Average	**1.68**
n/a	Downstream	0	0.134

TABLE 4.2: **Cell Wall Thicknesses – Barbara.** This cell was used for the first data point $Q^2 = 1.4\,\mathrm{GeV}^2$.

Right/Left	From	Distance (cm)	Thickness (mm)
n/a	Upstream	0	0.121
Left	Upstream	3.5	1.65
		12.11	1.71
Neutron		19.3	1.72
Side	Downstream	12.2	1.62
		4.2	1.54
		Average	**1.65**
Right	Upstream	4.0	1.49
		11.3	1.60
Electron	Downstream	19.6	1.56
Side		13.4	1.66
		3.7	1.61
		Average	**1.58**
n/a	Downstream	0	0.152

TABLE 4.3: **Cell Wall Thicknesses – Dolly.** This cell was used for the second data point $Q^2 = 2.5\ \mathrm{GeV}^2$.

Right/Left	From	Distance (cm)	Thickness (mm)
n/a	Upstream	0	0.126
Left	Upstream	3.6	1.64
		11	1.60
Neutron		20	1.60
Side		27.3	1.62
	Upstream	3.0	1.59
		Average	**1.61**
Right	Upstream	3.8	1.55
	Downstream	27.0	1.64
Electron		19.5	1.65
Side		12.3	1.64
		3.9	1.59
		Average	**1.61**
n/a	Downstream	0	0.138

TABLE 4.4: **Cell Wall Thicknesses – Edna.** This cell was used for the third and fourth data points $Q^2 = 1.7\ \mathrm{GeV}^2$ and $Q^2 = 3.5\ \mathrm{GeV}^2$

Right/Left	From	Distance (cm)	Thickness (mm)
n/a	Upstream	0	0.128
Left	Upstream	2.8	0.708
		11.5	0.815
Neutron		18.7	0.852
Side	Upstream	13.2	0.859
		3.5	0.944
		Average	**0.836**
Right	Upstream	4.1	1.10
		12.2	0.84
Electron		19.4	0.812
Side	Downstream	10.9	0.784
		4.3	0.849
		Average	**0.877**
n/a	Downstream	0	0.122

TABLE 4.5: **Reference Cell Wall Thicknesses.** This cell was used to measure background from glass and nitrogen in the cell.

Cell	Left Side (mm)	Right Side (mm)	Upstream Window (mm)	Downstream Window (mm)
Anna	1.568	1.690	0.131	0.127
Barbara	1.568	1.690	0.151	0.134
Dolly	1.648	1.584	0.121	0.152
Edna	1.610	1.610	0.126	0.138
Reference	0.836	0.877	0.128	0.122

TABLE 4.6: **Summary of Cell Glass Thicknesses.** Summary table of the thicknesses for all cells used in experiment 02-013, where left is the side closest to the neutron detector and right is the side closest to the BigBite spectrometer.

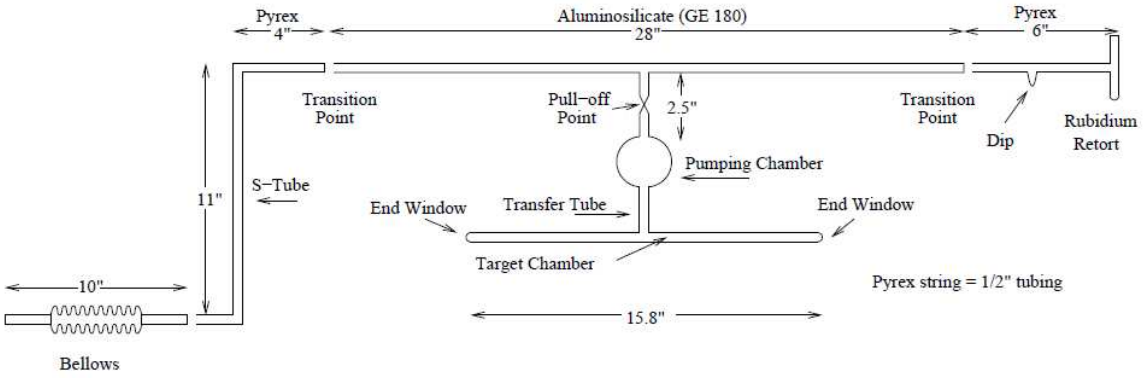

FIG. 4.9: **Target Cell String.** The target cell is shipped as part of a string that allows the cell to be connected to a vacuum pump.

The K-Rb mixtures for all cells used in E02-013 were prepared at the University of Virginia. A nominal K:Rb ratio of 20:1 in the vapor state at 235°C was used for every cell except Edna, which had a 5:1 ratio. Once mixed, this alloy was sealed in a glass ampule.

The cell is shipped as a string of cell, connecting tube, and retort. At the end of the connecting tube, a metal to glass connection allows the cell string to be connected to a combination vacuum pump and gas handling system (see Fig. 4.9). Upon arrival at the university laboratory, the alkali mixture is added to the retort and the cell is connected to a vacuum pump and evacuated. To remove any surface impurities (particularly water) an oven is constructed around the cell to bake out the surface. Portions of the string which are not contained within the oven are heated at regular intervals by means of an oxygen-enriched methane flame, kept at a temperature far below the melting point of the glass.

Prior to the cell fill, the alkali metal mixture is introduced to the pumping chamber by heating the metal and “chasing” the vapor into the pumping chamber. It is possible that some variation in the final alkali ratio is the result of this process.

The cells are filled by first measuring the internal volume of the cell and string by using a known volume of nitrogen at a known temperature. The system is evacuated, and

then the nitrogen buffer gas is added to the system. The cell is then externally cooled using liquid ^{4}He and the ^{3}He gas is added. Cooling is required to keep the pressure of the gas in the cell below atmospheric pressure so that the cell can be separated from the string and sealed. Details of this procedure can be found in Ref. [100].

4.6 Polarimetry

In previous experiments using a polarized ^{3}He target, two methods of measuring the polarization were used. The first is the straightforward method of adiabatic fast passage nuclear magnetic resonance (AFP NMR or just NMR), where the spins of all of the ^{3}He are flipped, creating EMF in a nearby coil that is directly related to the polarization. The second is electron paramagnetic resonance (EPR), where the alkali atoms are used as sensitive magnetometers. They are sensitive enough that the polarization is measured through the shift in the magnetic field around the atoms due to ^{3}He polarization.

These were independent measurements in the past, with the NMR signal calibrated to the known thermal polarization of water. For this experiment, EPR, with its precise absolute polarization measurement, was used to calibrate NMR. The straightforward NMR, which is measured in the scattering chamber, was used as a day-to-day check on the polarization.

4.6.1 Nuclear Magnetic Resonance

Throughout this document, the term NMR refers to a specific type of nuclear magnetic resonance. The specific type is nuclear magnetic resonance seen through adiabatic fast passage (AFP). AFP is a method of reversing the spins of polarized ^{3}He gas. In simple terms, this spin reversal is performed by changing the magnetic holding field while applying an orthogonal RF (91 kHz) magnetic field. If this change is performed slowly

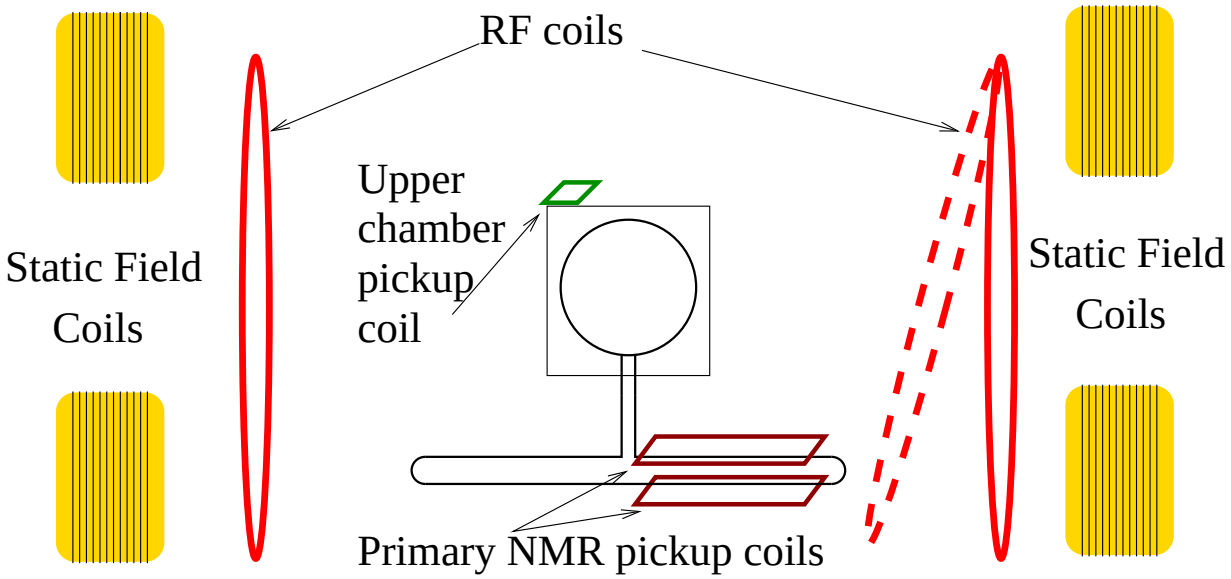

FIG. 4.10: **Schematic of NMR System.** Diagram of the NMR system used for E02-013

enough, it will be an adiabatic change and the spins will change direction. However, the change must be fast enough that the spins do not have time to relax. This relatively fast spin reversal produces an EMF in nearby pickup coils. This EMF is what is commonly referred to as our NMR signal.

A schematic of the NMR system can be seen in Fig. 4.10.

Adiabatic Fast Passage

A ^{3}He nucleus in a static magnetic field can be described by the classical equation for a free magnetization in a magnetic field [101]. For such a magnetization, the magnetic field exerts a torque:

$$\frac{d\vec{M}}{dt} = \gamma \vec{M} \times \vec{H}_0. \tag{4.40}$$

Here, the ^{3}He nucleus magnetic moment ($\vec{M}$) interacts with the static holding field, $\vec{H}_0$. γ is the gyromagnetic ratio.

The form of equation 4.40 indicates a rotation. It proves useful to transform to

rotating coordinates, with angular frequency $\vec{\omega}$. The time-derivative of a time dependent vector $\vec{A}(t)$ computed in the laboratory frame and its derivative calculated in the rotating frame (rotating with frequency $\vec{\omega}$) is:

$$\frac{d\vec{A}}{dt} = \frac{\partial \vec{A}}{\partial t} + \vec{\omega} \times \vec{A}. \tag{4.41}$$

The motion of the magnetic moment in the rotating frame can be obtained by combining 4.40 and 4.41:

$$\frac{\partial \vec{M}}{\partial t} = \gamma \vec{M} \times \left(\vec{H}_0 + \frac{\vec{\omega}}{\gamma} \right). \tag{4.42}$$

This is similar to equation 4.40, provided that $\vec{H}_0$ is replaced by an effective field $\vec{H}_e = \vec{H}_0 + \vec{\omega}/\gamma$. The quantity $\vec{\omega}/\gamma$ can therefore be thought of as a fictitious field resulting from the rotation. Assuming that $\vec{H}_0$ is constant with time, we can choose a frame in which the effective field vanishes ($\vec{\omega} = -\gamma \vec{H}_0$). In this frame the magnetic moment is fixed. Back in the laboratory frame, the magnetic moment rotates with frequency $\omega_0 = -\gamma H_0$, the Larmor frequency of a magnetic moment in an applied field $\vec{H}_0$.

The unit vector $\hat{k}$ is defined such that $\vec{H}_0 = H_0 \hat{k}$. The total field $\vec{H}$ can be described as the total of the static field $H_0 \hat{k} = -(\omega_0/\gamma)\hat{k}$ and a field $\vec{H}_1$ perpendicular to $\vec{H}_0$ and rotating with frequency ω. In the rotating frame, therefore, the effective field is now written as:

$$\vec{H}_e = \left(H_0 + \frac{\omega}{\gamma} \right) \hat{k} + H_1 \hat{i}. \tag{4.43}$$

The magnitude of $\vec{H}_e$ is therefore:

$$H_e = \left[\left(H_0 + \frac{\omega}{\gamma} \right)^2 + H_1^2 \right]^{\frac{1}{2}} = -\frac{a}{\gamma} \tag{4.44}$$

where

$$a = -\left[(\omega_0 - \omega)^2 + \omega_1^2 \right] \frac{\gamma}{|\gamma|}, \tag{4.45}$$

$$\omega_1 \equiv -\gamma H_1. \tag{4.46}$$

In terms of these frequencies, the angle $0 < \theta < \pi$ between $\vec{H}_e$ and $\vec{H}_0$ is:

$$\tan\theta = \frac{H_1}{H_0 + (\omega/\gamma)} = \frac{\omega_1}{\omega_0 - \omega} \tag{4.47}$$

or, in terms of sine:

$$\sin\theta = \frac{\omega_1}{a} = \frac{H_1}{H_e} \tag{4.48}$$

and cosine:

$$\cos\theta = \frac{\omega_0 - \omega}{a} = \frac{H_0 + \frac{\omega}{\gamma}}{H_e} \tag{4.49}$$

Therefore, in the typical case of $H_1 \ll H_0$, the effect of the rotating field on the magnetic orientation is small unless the frequency of the rotation ω is close to the Larmor frequency ω_0. Furthermore, in the typical case a rotating applied field is not used, but rather a linearly oscillating field, a linearly polarized field $2H_1 \cos\omega t$ can be considered to be the superposition of two fields of magnitude H_1 rotating in opposite directions with frequency ω.

This is the case for a static $\vec{H}_0$. If instead of a static field, the field varies slowly, the angle of magnetization with respect to the holding field is also a constant of the motion. The condition that the holding field varies slowly enough to allow the magnetization angle to be constant is the adiabatic condition, $|\Omega| \ll |\gamma H|$, where $|\Omega|$ has units of frequency and is the rate of change of the magnetic field.

A general description of the variation of time of vector $\vec{H}(t)$ is:

$$\frac{d\vec{H}}{dt} = \vec{\Omega} \times \vec{H} + \Omega_1 \vec{H} \tag{4.50}$$

The time variation of the effective field (where the H_0 is varying linearly with time) is

$$\frac{d\vec{H}_e}{dt} = \cos\theta \frac{\dot{H}_0}{H_e} \vec{H}_e + \sin\theta \frac{\dot{H}_0}{H_e} (\vec{n} \times \vec{H}_e) \tag{4.51}$$

where $\vec{n}$ is a unit vector orthogonal to $\vec{H}_0$ and $\vec{H}_1$. Comparing this with the general expression for the time derivative of the vector $\vec{H}$, Eq. 4.50, gives the relation:

$$\Omega = \sin\theta \frac{\dot{H}_0}{H_e} = H_1 \frac{\dot{H}_0}{H_e^2}$$

So, in terms of the fields used in AFP, the adiabatic condition can be written as

$$\dot{H}_0 \ll \frac{\gamma H_e^2}{\sin\theta} \tag{4.52}$$

At resonance (where the condition is strongest), the adiabatic condition simplifies to:

$$\dot{H}_0 \ll \gamma H_1^2. \tag{4.53}$$

It can be shown that if this condition is met, then the angle of magnetization with respect to $\vec{H}_e$ is a constant of the motion[101].

If the holding field starts below resonance with the oscillating field, then the effective field is practically parallel to the holding field. As the holding field changes and moves through resonance, the magnetic moment of ^{3}He will follow the effective field. By following the effective field the magnetic moment will eventually become anti-parallel to the holding field. As the magnetic moment of ^{3}He passes through resonance, there will be a magnetic moment equal to the initial value of the ^{3}He magnetism, in the direction of $\vec{n}$.

The change in the magnetic field must be slow enough to satisfy the adiabatic condition. However, the change must be faster than the relaxation times T_1 and T_2, which are longitudinal and transverse relaxation times. Here, longitudinal and transverse are with respect to the static holding field. The longitudinal relaxation time is the trend of the magnetization to its equilibrium value:

$$\frac{dM_z}{dt} = -\frac{M_z - M_0}{T_1}, \tag{4.54}$$

where $M_0 = \chi_0 H_0$ is the equilibrium magnetization (χ_0 is the magnetic susceptibility).

The transverse relaxation time, T_2, comes from the interaction of the spins with each other. In other words, the description of the motion of the magnetic spins above is for a free magnetic moment. The transverse relaxation time arises from the fact that these moments are in an ensemble with other magnetic moments. The transverse effect can be written:

$$\frac{dM_x}{dt} = -\frac{M_x}{T_2} \frac{dM_y}{dt} = -\frac{M_y}{T_2}$$

In practice, the sweep rate of 1.2 G/s is both faster than the relevant relaxation rate of approximately 2×10^{-3} G/s and slower than the adiabatic condition of approximately 6×10^{5} G/s.

NMR Signal

If the holding field starts far from resonance, then the magnetic moment of the ^{3}He is parallel to the holding field (as H_e is also parallel to the holding field). As the magnetic field is swept through resonance, the magnetic moment follows H_e and ends up anti-parallel to the holding field. As the holding field reaches resonance with the oscillating field, there is a transverse magnetization equal in size to the magnetization when the field was held static. This will induce a voltage signal, $S(t)$, that can be measured in pickup coils that are perpendicular to both the holding field and the oscillating field [93]

$$S(t) \propto M_{\mathrm{T}} = M\frac{H_{e,\mathrm{T}}}{|\vec{H}_e|} = M\frac{H_1}{\sqrt{(H(t)-H_0)^2+H_1^2}}, \tag{4.55}$$

where M_{T} is the component of the magnetic moment vector that is transverse to the static holding field, and $H_{e,\mathrm{T}}$ is the component of the effective field transverse to the static holding field.

In practice, this signal is modified by the magnetic flux through the coils, the gain of the electronics used to measure the signal, and the density of the ^{3}He gas. Due to these factors, the signal is a relative measurement. Absolute calibration is possible through the use of a water cell [100]. However, for E02-013, calibration was performed with electron paramagnetic resonance *in situ* (see Sec. 4.6.2), so the factors that modify the signal were constant. EPR calibration allows the use of NMR as a fairly simple, robust measurement that can quickly provide a relative measurement of the polarization.

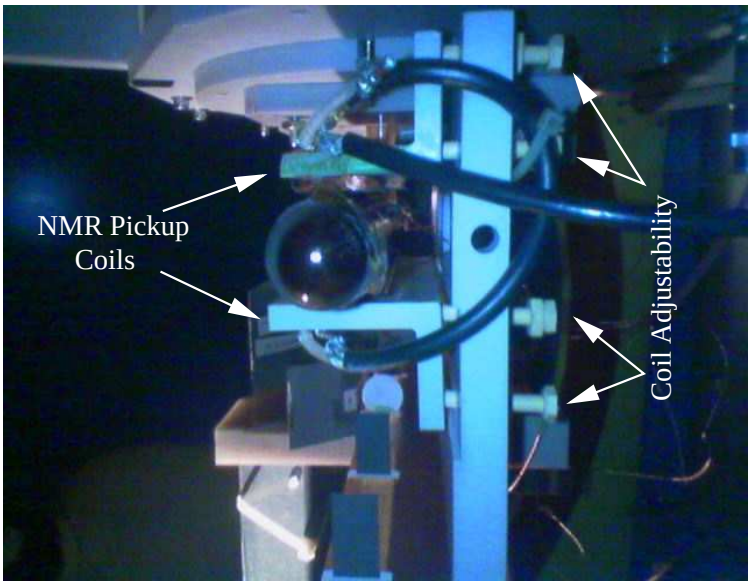

FIG. 4.11: **Adjustable NMR Coils.** For the first time in a Jefferson Lab polarized ^{3}He experiment, the adjustablitity of the coils was part of the target design.

NMR Background

Background signals in Jefferson Lab NMR measurements are typically suppressed through the use of a lock-in amplifier. An RF signal generator sends a timing signal that the lock-in amplifier uses to isolate signals that occur with the same frequency. The background is limited to two sources: the small fraction of the random background spectrum that is accepted by the lock-in amplifier, and signal that is correlated with the RF signal generator.

In general, this correlated signal has produced the greatest "noise" for the NMR signal. The most direct method of reducing this signal is to make minute adjustments to the location of the NMR pickup coils so as to be orthogonal to the RF drive field. For E02-013, this method was made easier through the inclusion of a specially designed mounting system that allowed remarkable adjustability (see Fig. 4.11).

In addition, a gross adjustability of the RF drive coils was added (Fig. 4.10). One coil was fixed in place, and the partner second coil was installed so that its angle with

respect to the other coil could be adjusted. In practice, this adjustment was made first, and locked in place. Then the fine-tuning adjustments could be made at the NMR coils.

Previous experiments had attempted to cancel this signal by using an electronic device to take a copy of the signal, match the amplitude of the copy to the amplitude of the signal through the pickup coil, then add the copy and the pickup signal out of phase. For E02-013, a small coil on an adjustable mount was installed close to the RF drive coil. The orientation of the coil was adjusted so that the amplitude of the signal through the small coil was the same as the signal through the NMR coils. Then the small coil signal was fed to the NMR system's pre-amplifier. The pre-amplifier has two inputs (A and B) and the option of adding the signal out of phase (A-B). This passive cancellation signal proved to be stable and significantly reduced the background signal in the NMR measurements.

NMR Measurements During E02-013

In a typical day, an NMR polarization measurement was made every 6 hours. NMR measurements were also taken before data-taking resumed after an extended down time.

The procedure for performing an NMR measurement, from the shift-takers perspective, was relatively straightforward. First, the shift-taker prepared the cell by confirming that the ^{3}He cell is in the beam position, and making sure that the beam is off. The target ladder was designed so that the NMR measurement could be taken in any location. However, for the sake of consistency, the measurements were always made with the target in the same position. This avoided any effects due to large-scale field inhomogeneity and mis-alignment of the laser. Moving the target changed the laser path length and could mean less laser light was incident on the cell; this would result in a change in internal temperature, and therefore an incorrect polarization extraction. This is also why, if the target was moved before the measurement, the target operator must wait until the temperature has stabilized before proceeding.

The target operator ran the NMR measurement by running a LabView program. This program turned on the RF field, then ramped current through the coils on the magnetic box to ramp the magnetic field from 20 G to 32 G (referred to as the UP sweep). As the field was swept, the signal from the pick-up coils was read by the lock-in amplifier. After the current was lowered back to its set point, re-aligning the ^{3}He magnetization, this was the DOWN sweep, and data were collected during this sweep as well. A schematic of the NMR electronics is included as Figure 4.12. At this point, the target was ready to take data again. If target movements were kept to a minimum, NMR measurements could be taken within a five minute window. The target operators then extracted the signal height using the LabView fitting program, and received four values, as they fit both the up and down sweeps. The lock-in amplifier split the signal into X and Y channels, relative to the reference signal. Once UP and DOWN signal heights for the X and Y files for the pickup coils were determined, the target operator could compute the polarization by applying this formula to the values:

$$P = \frac{C}{2} * \left(\sqrt{X_{\mathrm{Up}}^2 + Y_{\mathrm{Up}}^2} + \sqrt{X_{\mathrm{Down}}^2 + Y_{\mathrm{Down}}^2} \right)$$

where P is the target polarization, C is the calibration constant provided by the target experts, $\mathrm{X_{Up}}$ is the signal height of the Up sweep in the x-channel, $\mathrm{Y_{Up}}$ is the signal height of the Up sweep in the y-channel, and $\mathrm{X_{Down}}$ and $\mathrm{Y_{Down}}$ are the signal heights of the Down sweep.

4.6.2 Electron Paramagnetic Resonance

The method of electron paramagnetic resonance uses light from the target cell's alkali metals as a precise magnetometer. This magnetometer is used to measure the small change in the magnitude of magnetic field due to polarized ^{3}He that is either aligned or anti-aligned with the main holding field.

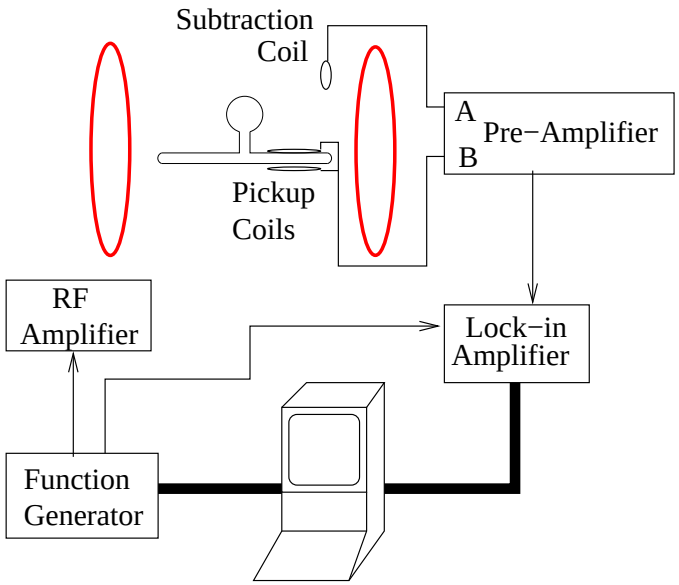

FIG. 4.12: **NMR Electronics.** Arrangement of the electronics required to make electronics measurements. The pre-amplifier subtracts the signal from the subtraction coil before sending the signal to the lock-in amplifier.

There are two shifts in the Zeeman resonance of Rb and K in the presence of polarized ^{3}He. There is a shift due to the same spin exchange mechanism that produces the polarization in the gas [102]. There is also a shift due to the presence of a classical magnetic field of the polarized ^{3}He. These shifts can be isolated by changing the direction of the magnetic field, or by reversing the direction of the ^{3}He magnetic moments with respect to the field. A variation of the method of AFP described in Sec. 4.6.1, in which the holding field is held constant and the frequency of the RF field is varied is used to flip the ^{3}He magnetic moments.

The shift due to the magnetic field produced by the polarized ^{3}He is proportional to the ^{3}He magnetization (and therefore the density and polarization of the ^{3}He [93]):

$$\Delta\nu_b = \frac{d\nu_{\rm EPR}(F,M)}{dB} C M_{\rm He} = \frac{d\nu_{\rm EPR}(F,M)}{dB} C n_{\rm He} \mu_{\rm He} P_{\rm He} \tag{4.56}$$

where ν_b is the shift due to the ^{3}He magnetic field, $\nu_{\rm EPR}$ is the frequency due to the EPR transition and depends on the F, M quantum numbers of the transition, B is the magnetic

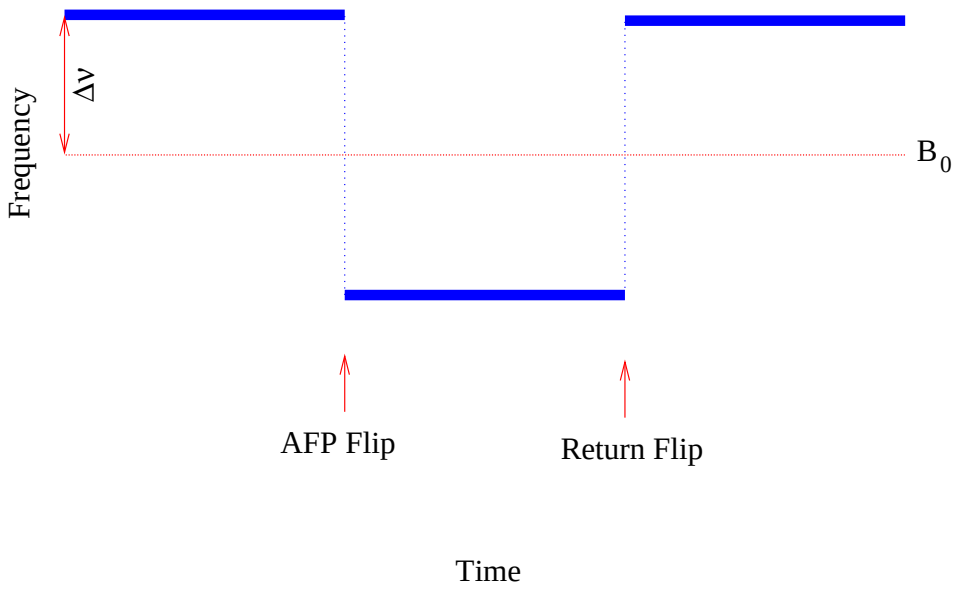

FIG. 4.13: **EPR Measurement.** Sketch of the EPR transition, with the the shift of the frequency from the frequency due to the main holding field, B_0, highlighted.

field, C is a dimensionless quantity that depends on the shape of the sample, and M_{He} is the magnetization of ^{3}He. The magnetization is the product of the number of ^{3}He nuclei, n_{He}, the magnetic moment of ^{3}He, μ_{He}, and the average polarization of the ^{3}He sample, P_{He}. For a spherical sample, combining the shifts due to collision and classical magnetic field, we obtain:

$$\Delta\nu_{\mathrm{EPR}} = \frac{8\pi}{3}\frac{d\nu_{\mathrm{EPR}}(F,M)}{dB}\kappa_0\mu_{\mathrm{He}}P_{\mathrm{He}} \tag{4.57}$$

where κ_0 is a constant which depends on temperature that has been measured experimentally [103].

Measuring EPR Frequency

This change in frequency depends on many things, but the small shift that is due to the magnetization of ^{3}He is the only shift that depends on the direction of the ^{3}He spins. Therefore, we can isolate the shift if we can change the direction of the spins while keeping everything constant. We do this by means of frequency sweep AFP (applying

an oscillating field that is in resonance with the ^{3}He nuclei's precession in an applied magnetic field—this is very similar to how NMR is performed).

We measure the frequency before and after the "flip". This isolates everything else and leaves us with (twice) the frequency shift due to the ^{3}He polarization. Taking difference between the frequency before the flip ($\nu\uparrow$) and the frequency after the flip ($\nu\downarrow$),

$$\nu\uparrow - \nu\downarrow = \nu_{\rm all} - \nu_{\rm all} + \nu_{^3{\rm He}\uparrow} - \nu_{^3{\rm He}\downarrow}, \tag{4.58}$$

where $\nu_{^3{\rm He}}$ is the frequency shift due to ^{3}He and $\nu_{\rm all}$ is the frequency shift due to all other effects. Since

$$\nu_{^3{\rm He}\uparrow} = -\nu_{^3{\rm He}\downarrow},$$

the difference between the two frequencies is twice the shift due to the polarization of ^{3}He. This can also be seen schematically in Fig. 4.13.

Locking the Frequency

The EPR transition is excited by broadcasting an RF frequency signal through a coil. We scan across a frequency to find the transition, and then lock to that transition.

Exciting the EPR transition depolarizes the alkali metal (Rb, for simplicity). Once the alkali metal depolarizes, it begins to re-polarize, and produces a florescence. We can track the amount of florescence as a function of RF frequency. Because our RF frequency is FM modulated, we see the derivative of the EPR transition line-shape. We lock to the zero of the derivative (*i.e.*, a maximum or minimum, but we know it's the local maximum), using a feedback loop. Figure 4.14 is a diagram of the feedback loop electronics.

Once the frequency is locked, the AFP sweep can begin. At the moment of resonance, all the ^{3}He spins flip. The feedback system can track the EPR frequency during this flip and the system is locked to the new EPR frequency. In this state, the ^{3}He spins are anti-aligned with the alkali metals polarization direction, so a return flip is required to prevent depolarization.

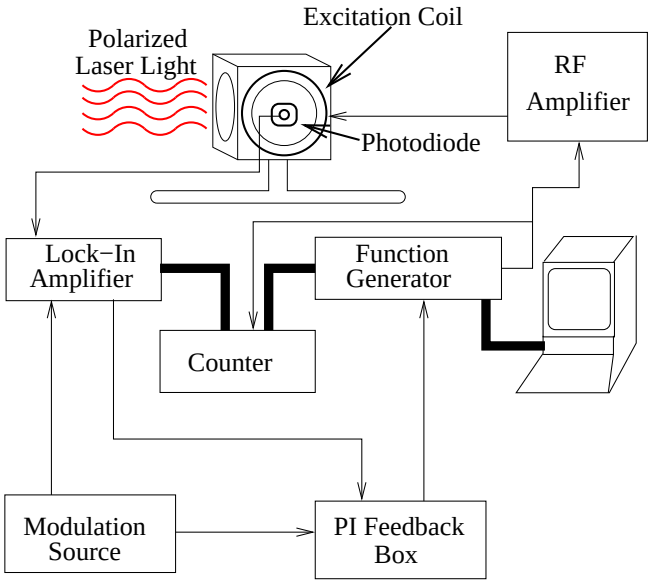

FIG. 4.14: **EPR Electronics Diagram.** Diagram of the electronics used to create the feedback loop required to precisely measure the frequency of the EPR transition.

The Parameter κ_0

In Eq. 4.57 there is a parameter, κ_0, that depends on temperature, but not the density or the polarization of ^{3}He. If all Rb-^{3}He interactions were ignored, the frequency shift would be due to the classical magnetization of a sphere. Experimentally, $\kappa_0 \approx 6$ and can be thought of as an enhancement due to the attraction of the Rb electron wavefunction to the ^{3}He nucleus.

The Fermi-contact interaction term for the interaction of a polarized alkali and a noble gas takes the form $\alpha\vec{K}\cdot\vec{S}$, where $\vec{K}$ is the spin of the noble gas nucleus, and $\vec{S}$ is the spin of the alkali metal. The coupling parameter, $\alpha(R)$ depends on the distance between the nuclei and of the noble gas and the alkali metal. This parameter takes the form,

$$\alpha = \frac{8\pi}{3} g_s \mu_B \frac{\mu_K}{K} |\Psi(R)|^2, \tag{4.59}$$

where g_s is the Landé g-factor, μ_B is the Bohr magneton, and μ_K is the magnetic moment of the noble gas nucleus [104]. The wavefunction, $\Psi(R)$ has been enhanced by the

presence of a noble gas:

$$\psi(R) = \eta\phi(R), \tag{4.60}$$

where $\phi(R)$ is the alkali-metal valence wavefunction in the absence of a noble gas, and $\eta \gg 1$ for all noble gases. The enhancement comes from the large kinetic energy acquired by the electron as it scatters in the core potential of the noble-gas atom [95].

This spin-exchange enhancement translates to an enhancement in the EPR frequency shift. It can be easily seen in the calculation of κ_0 at high pressure [104]:

$$\kappa_0 = \eta^2 \int_0^\infty |\psi(R)|^2 e^{-V(R)/kT} 4\pi R^2 dR \tag{4.61}$$

where $V(R)$ is the van der Waals potential. Uncertainty in the van der Waals potential and the enhancement factor prevent accurate calculations of κ_0. Recently efforts have been made to determine the temperature dependence of κ_0. Clearly, calculations of the temperature dependence suffer from the same difficulties:

$$\frac{d\kappa_0}{dT} = \frac{\eta^2}{kT^2} \int_0^\infty |\psi(R)|^2 e^{-V(R)/kT} 4\pi R^2 dR \tag{4.62}$$

However, since this enhancement is due to the the interaction of valence-electrons with the alkali metal, there is a strong dependence on the alkali metal density. κ_0 can be seen as the proportionality factor between an average valence-electron density and the alkali metal atom density, $[A]$,

$$(|\psi|^2)_{\text{av}} = \kappa_0[A]. \tag{4.63}$$

4.6.3 Magnitude and Direction of B_0

This measurement of the polarization also provides "free" information about the magnitude of the magnetic field and orientation of the ^{3}He spins with respect to the magnetic field.

As seen in Fig. 4.13, the magnitude of B_0 can be extracted from the frequency about which the EPR transitions occur. This has proved to be an incredibly precise measure-

State	Flip?	Spins
Hat	Flipped	Aligned
Well	Not Flipped	Anti-Aligned

TABLE 4.7: **The States of the Spins.** The alignment of the spins with the magnetic field can be determined from the shape of the EPR signal.

ment of the magnetic field in the location of the EPR measurement. For E02-013, this effectively means we measured the magnetic field about once a day.

The direction of the ^{3}He spins cannot be determined directly from the EPR data. However, once the magnetic holding field direction is known, it is a simple matter to determine if the spins are aligned or anti-aligned relative to the holding field. One needs to combine this information with some other measurement to determine the direction of the ^{3}He spins with respect to an external coordinate system.

In the case of a frequency shift above the holding field "frequency," meaning the mid-point between the two EPR frequencies, ("well" state, pictured in Fig. 4.13), the effective field seen by the alkali metal is the holding field plus the classical field of the polarized gas. For the "hat state" (not pictured), the field subtracts.

Recall that the magnetic moment for ^{3}He is negative, and the neutron spins are aligned with the ^{3}He spins. This means that if the field is adding, then the spins (of both the neutron and ^{3}He) are pointed opposite the magnetic field. The relation between the direction of the spins and the shape of the EPR signal can be seen in Table 4.7.

4.6.4 Hybrid EPR

When only one alkali metal is used in the cell, EPR is a straightforward proposition. For the hybrid cells, there is a mixture of two alkali metals. The EPR response of either metal can be monitored by the fluorescence of the metal being pumped.

In Rb-K hybrid cells, the spin exchange between Rb and K is so efficient that at

any point in time the polarizations of the two metals are identical. It is this property that allows the K to polarize the ^{3}He without being pumped directly. However, it is also this property that allows EPR to be performed on either metal. Exciting the EPR transition in K depolarizes the K. The depolarized K depolarizes the Rb; the process of re-polarizing the Rb causes the Rb to fluoresce.

The depolarization of interest comes from exciting the EPR transition in the alkali metal in the cell. In the case of a hybrid cell, either alkali metal can be depolarized. In either case, we use the D_2 line of the metal that is optically pumped. It is possible to use the amount of D_2 light of one metal (*e.g.* Rb) to monitor the depolarization of another (*e.g.* K) because the spin-exchange cross section for Rb and K is extremely large [11]. In this way, the Rb polarization serves as a real time monitor of the K polarization.

Potassium κ_0 Temperature Dependence

The value of κ_0 for Rb-^{3}He has a marked temperature dependence. Recent measurements by Babcock *et al.* [103] expand the temperature range beyond the precision measurements of this value by Romalis and Cates [102]. Typically, $\kappa_0(T)$ is reported as two parts: a static value (κ_0) and a temperature dependent piece (κ_0'), so that:

$$\kappa_0(T) = \kappa_0(T_{\rm ref}) + \kappa_0'(T - T_{\rm ref}), \tag{4.64}$$

where $T_{\rm ref}$ is a given reference temperature.

For the recent Babcock measurement [103], $\kappa_0 = 6.39$ and $\kappa_0' = 0.00934 \pm 0.00014$, with $T_{\rm ref} = 200^\circ{\rm C}$. The uncertainty on the temperature dependence is small at 1.5%.

This is not the case for $\kappa_0^{\rm K}$. In the same paper, Babcock *et al.* use the values from Romalis and Cates [102] and hybrid cells to measure values for $\kappa_0^{\rm K}$ and $\kappa_0^{\rm Na}$. Both $\kappa_0^{\rm K}$ and $\kappa_0^{\rm Na}$ have temperature dependence similar to $\kappa_0^{\rm Rb}$. However, there is a greater uncertainty

on both the reference value of κ_0 and the temperature dependence.

$$\kappa_0^{\mathrm{K}}(T) = (5.99 \pm 0.11) + (0.0086 \pm 0.0020)(T - 200^{\circ}\mathrm{C}) \quad (4.65)$$

$$\kappa_0^{\mathrm{Na}}(T) = (4.72 \pm 0.09) + (0.00914 \pm 0.00056)(T - 200^{\circ}\mathrm{C}) \quad (4.66)$$

The target used for E02-013 was routinely operated at temperatures of approximately 280° C (see Sec 4.6.5 for details). At these high temperatures, the uncertainty on κ_0^{K} due to temperature is 2.4%. When the systematic uncertainty on the reference value is combined, the total systematic uncertainty on κ_0^{K} is 3.0%, which is a 4.1% effect on the measurement of the polarization. This is, by far, the largest systematic uncertainty on the target polarization.

4.6.5 Target Density

The $^3\vec{\mathrm{He}}$ cell has 8 resistive temperature devices (RTDs) attached to various locations. These RTDs are constantly read out via the Hall A EPICS system. Since they are placed on the outside of the cell, localized internal heating (*e.g.*, from laser energy absorption in the pumping chamber) is not registered by the RTDs, due to the temperature gradient across the thick (approximately 4 mm) glass wall. To correct for this, a series of temperature tests are performed on the cell to gauge the true temperature of the gas within.

These tests are a series of NMR measurements. First, the NMR signal is measured with the lasers on. Then lasers are turned off, and the cell is allowed to reach equilibrium temperature. Then, another NMR measurement is performed. Once the depolarization effects due to performing the NMR measurements are taken into account, the relative difference in signal height gives an indication of change in density. The change in density, combined with the measurement of the target chamber temperature, gives the true pumping chamber internal gas temperature.

Theory of Density Measurements

The NMR signal can be expressed as the product of a number of factors:

$$S_{\mathrm{NMR}} = P \cdot n_{\mathrm{He}} \cdot \Phi \cdot \mu_{\mathrm{He}} \cdot C_{\mathrm{electric}} \tag{4.67}$$

where C_{electric} accounts for factors due to the electronics used, $\mu_{^3\mathrm{He}}$ is the ^{3}He magnetic moment, Φ is the flux through the coils, $n_{^3\mathrm{He}}$ is the number of ^{3}He atoms that generate that flux and P is the polarization of those atoms. When performing the temperature tests, we will be looking at the ratio of signals, reducing the equation to an expression that depends solely on the polarization and density,

$$\frac{S_{\mathrm{on}}}{S_{\mathrm{off}}} = \frac{P_i n_{\mathrm{on}}}{P_j n_{\mathrm{off}}},$$

where S_{on} is the signal in the NMR pickup coils with the lasers on, and S_{off} is the corresponding signal with the lasers off, $n_{\mathrm{on(off)}}$ is the number of ^{3}He nuclei seen by the pickup coils with the lasers on (off). The polarization may change during the series of measurements and $P_i \neq P_j$. There is a depolarization of the ^{3}He each time that an NMR measurement is made (referred to as AFP loss). A correction can be applied to so that the polarizations can be treated as equal. Once corrected, the equation simplifies even further.

$$\frac{S_{\mathrm{on}}}{S_{\mathrm{off}}} = \frac{n_{\mathrm{on}}}{n_{\mathrm{off}}} \tag{4.68}$$

Since the volumes are the same, the NMR signal effectively functions as a pressure gauge. The number of atoms in the target chamber (n_t) can be determined from the known volumes, and the ratio of the temperatures,

$$n_t = \frac{n_0}{1 + \frac{V_p}{V_0}\left(\frac{T_t}{T_p} - 1\right)} \tag{4.69}$$

where n_0 is the number of ^{3}He nuclei in the target chamber of the target when both chambers are in thermal equilibrium, n_t is the number with the target at a different temperature,

V_p is the volume of the pumping chamber, V_0 is the total volume of the cell, and T_t and T_p are the temperatures of the target and pumping chambers, respectively.

Equation 4.69 follows from the ideal gas law. Although the density of the cell ($n_\circ$) at uniform temperature is known, it is not required, since the ratio of the target chamber with the lasers on ($n_{\rm on}$) to the density with the laser off ($n_{\rm off}$) is required. The approximation $T_{t\ {\rm on}} \approx T_{t\ {\rm off}} = T_t$ is supported by the data. There are only slight fluctuations, which are consistent with fluctuations if the target pumping chamber temperature is stable.

$$\frac{S_{\rm on}}{S_{\rm off}} = \frac{n_{\rm on}}{n_{\rm off}} = \frac{1 + \frac{V_p}{V_0}\left(\frac{T_t}{T_{p\ {\rm off}}} - 1\right)}{1 + \frac{V_p}{V_0}\left(\frac{T_t}{T_{p\ {\rm on}}} - 1\right)} \tag{4.70}$$

Experimental Method

There are two series of tests that must be performed for an accurate laser on/off temperature test. The first is the hot AFP loss tests, the second is the laser on/off temperature tests.

AFP Loss Tests

When an NMR measurement is performed on the E02-013 ^{3}He target, there is a small loss in the polarization. This loss is particular to the type of NMR measurement performed. Since we use adiabatic fast passage NMR, this loss is commonly referred to as "AFP loss". There are many factors that contribute to the AFP loss. There are gradients in the magnetic holding field, impurities in the glass used for the cell, etc. While it would be possible to calculate these contributions to the AFP loss, it is much more straightforward to merely measure this loss. Observations of this loss indicate that it changes with temperature. Due to the variety of contributions to the loss, both temperature dependent and independent, it is again much more straightforward to measure the loss than to attempt to calculate it.

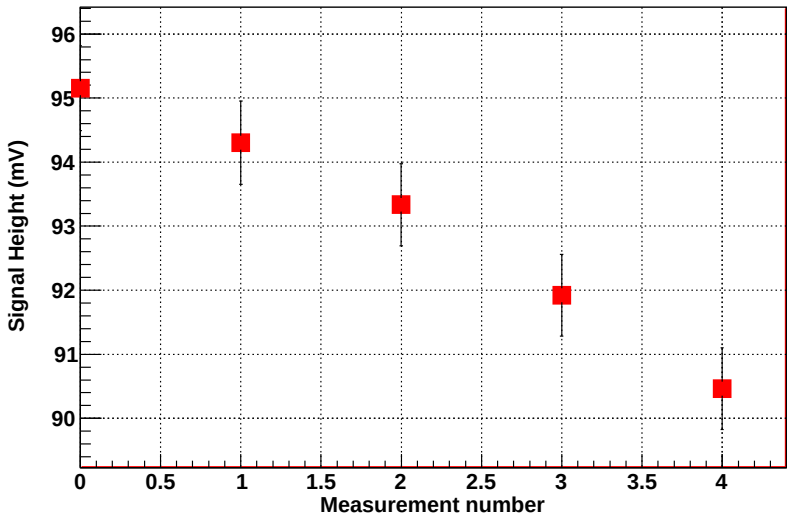

FIG. 4.15: **AFP Loss Test.** Multiple NMR measurements are performed and the average loss per measurement is calculated

The measurement of this loss is very direct. With the cell in an equilibrium state (close to maximum polarization and little recent interaction with the electron beam), the lasers are turned off. The temperature of the cell is allowed to stabilize. Once the temperature is stabilized, a number of NMR measurements (typically 5-10) are performed. The result is a clearly visible loss per measurement, as seen in Figure 4.15. A correction could be made for the depolarization over time that will occur when the cell is no longer polarizing. Since the characteristic decay time is approximately 30 hours and the tests took approximately 10 minutes, the depolarization due to the lasers being off was considered a negligible correction.

Lasers On/Off Tests

The next step is to collect the data with the lasers on and off. First, with the cell at equilibrium, a single NMR measurement is made. Then, the lasers are turned off and the cell is allowed to cool. This cooling takes about 10 minutes. The temperature is

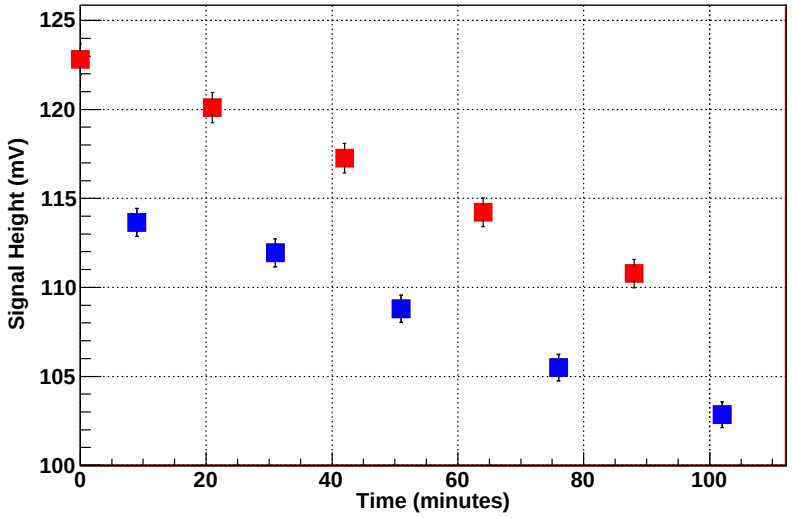

FIG. 4.16: **Uncorrected Lasers On and Off.** There is a clear separation between measurements made with the lasers on and off.

monitored via a stripchart display. When the cell temperature flattens out, the next NMR measurement is made. Once this measurement is made, the lasers are turned back on and the cycle repeats. For Edna, the cycle was repeated four times.

In the case of Edna, the temperature stabilized approximately 5°C below the previous set-point. The time between measurements was approximately 10 minutes. Figure 4.16 shows the clear separation between the lasers on and lasers off. It is also clear that the "slope" is similar to that of the AFP loss test. Once the AFP loss corrections have been made, the differences are even clearer, as in Figure 4.17

Results

Table 4.8 lists the results for the AFP loss test. The average of the losses is 1.24% for the up sweep and 1.27% for the down sweep. The value of 1.26% loss per measurement was used to correct the signals for the lasers on/off test. A similar dataset exists for the AFP loss at the operational temperature with the laser on. It should not be a surprise that

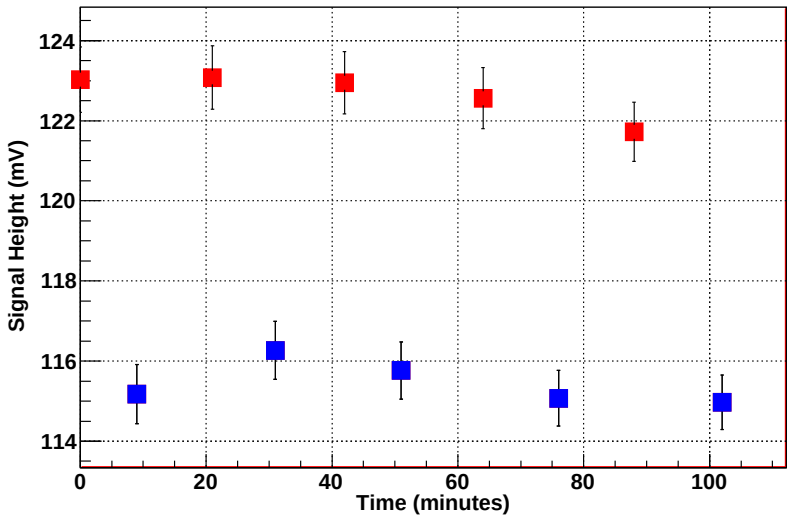

FIG. 4.17: **AFP Loss Corrected Lasers On and Off.** With the AFP corrections added, the separation between measurements with the lasers on and off is very clear; the measurements can also be seen to group together.

the AFP loss is less when the lasers are on. The average of the losses for lasers on are 1.07% for the up sweep and 1.12% for the down sweep. The average of these losses is 1.10%.

Table 4.9 lists the temperature for each measurement in the lasers on/off test. The control RTD and RTD 7 are the measurements for the temperature in the oven (measured on the cell). RTDs 1, 2, 3, and 5 are measurements on the target along the target chamber. All measurements are in degrees Celsius. A striking feature of this table is the lack of variation between measurements for the RTDs on the target chamber. This is the justification for the approximation made in Section 4.6.5; $T_{t\ \mathrm{on}} \approx T_{t\ \mathrm{off}} = T_t$.

Table 4.10 contains the corrected values from the laser on off tests. Each value on the table (except for the first ones) are corrected based on whether or not the lasers were on during the previous measurement.

The parameters used for the calculation of the temperature with the lasers on are listed in Table 4.11. Given these values, we can go back to Equation 4.70. Note: V_0 is the

total volume of the cell.

$$\frac{S_{\rm on}}{S_{\rm off}} = \frac{1+\frac{V_p}{V_0}\left(\frac{T_t}{T_{p\ \rm off}}-1\right)}{1+\frac{V_p}{V_0}\left(\frac{T_t}{T_{p\ \rm on}}-1\right)}$$

From Table 4.11, the following useful ratios are formed:

$$\frac{S_{\rm on}}{S_{\rm off}} = 1.0625 \tag{4.71}$$

$$\frac{V_p}{V_0} = 0.7730 \tag{4.72}$$

$$\frac{T_t}{T_{p\ \rm off}} = 0.6086 \tag{4.73}$$

What remains is to find $\frac{T_t}{T_{p\ \rm on}}$.

$$\begin{aligned}
1.0625 &= \frac{1+0.773\,(0.6086-1)}{1+0.773\left(\frac{T_t}{T_{p\ on}}-1\right)} \\
\frac{T_t}{T_{p\ \rm on}} &= 0.5556 \\
\frac{T_t}{0.5556} &= T_{p\ \rm on} \\
T_t &= 308.77\ \mathrm{K} \\
T_{p\ \rm on} &= 555.74\ \mathrm{K} \\
T_{p\ \rm on} &= 282.59^\circ\ \mathrm{C} \\
\Delta T &= 39.63^\circ\ \mathrm{C}
\end{aligned}$$

4.6.6 Calibration of NMR System Using EPR Measurements

Polarization Gradient

Polarimetry for the $^3\mathrm{He}$ target in Hall A is typically performed with a combination of EPR (see Sec. 4.6.2) and NMR (see 4.6.1).For the experiment E02-013, no water calibration was performed. Therefore, the EPR measurement was not a cross check against the NMR calibration, but instead the only calibration for the NMR measurement.

Measurement	Up (mV)	Down (mV)	Loss Up	Loss Down
1	94.945	95.361	—	—
2	94.167	94.448	0.82%	0.96%
3	93.199	93.470	1.03%	1.04%
4	91.784	92.057	1.52%	1.51%
5	90.328	90.601	1.59%	1.58%

TABLE 4.8: **AFP Loss Results.** The results of the AFP loss tests performed with the lasers off, and the cell at its working temperature of approximately 250°C.

Measurement	control rtd	rtd 7	rtd 1	rtd 2	rtd 3	rtd 5
On 1	240.9	245.6	39.2	38.0	32.3	33.8
Off 1	235.8	233.3	39.4	37.8	33.9	32.0
On 2	241.0	245.2	39.1	39.7	33.7	32.5
Off 2	235.9	233.4	39.1	39.7	33.7	32.1
On 3	240.7	244.7	39.2	37.7	33.8	32.5
Off 3	235.4	232.7	39.1	37.6	33.5	32.0
On 4	240.8	244.7	38.9	37.7	33.4	32.3
Off 4	234.6	232.2	38.9	37.4	33.4	31.8
On 5	241.0	245.0	39.0	37.5	33.4	32.2
Off 4	236.1	232.9	38.6	37.5	33.3	31.9

TABLE 4.9: **Lasers On/Off Temperatures.** The temperatures listed (in degrees Celsius) were taken before each measurement.

Measurement	Up (mV)	Down (mV)	Average (mV)
On 1	122.8	123.3	123.0
Off 1	115.2	115.2	115.2
On 2	122.8	123.4	123.1
Off 2	116.1	116.5	116.3
On 3	122.6	123.3	122.9
Off 3	115.5	116.1	115.8
On 4	122.2	122.9	122.6
Off 4	114.6	115.5	115.1
On 5	121.3	122.2	121.7
Off 5	114.6	115.3	115.0
Average On	122.3	123.0	122.7
Average Off	115.2	115.7	115.5

TABLE 4.10: **Corrected Laser On/Off Values.** NMR values from the laser on/off values that have been corrected for AFP losses

Parameter	Value
T_t	35.62°C
$T_{p\ \mathrm{off}}$	234.23°C
$T_{p\ \mathrm{on}}$	242.96°C
V_0	377.73 mL
V_p	292 mL
S_{on}	122.67 mV
S_{off}	115.45 mV

TABLE 4.11: **Calculation Parameters.** Parameters used in the calculation of the true temperature in the pumping chamber when the lasers are on.

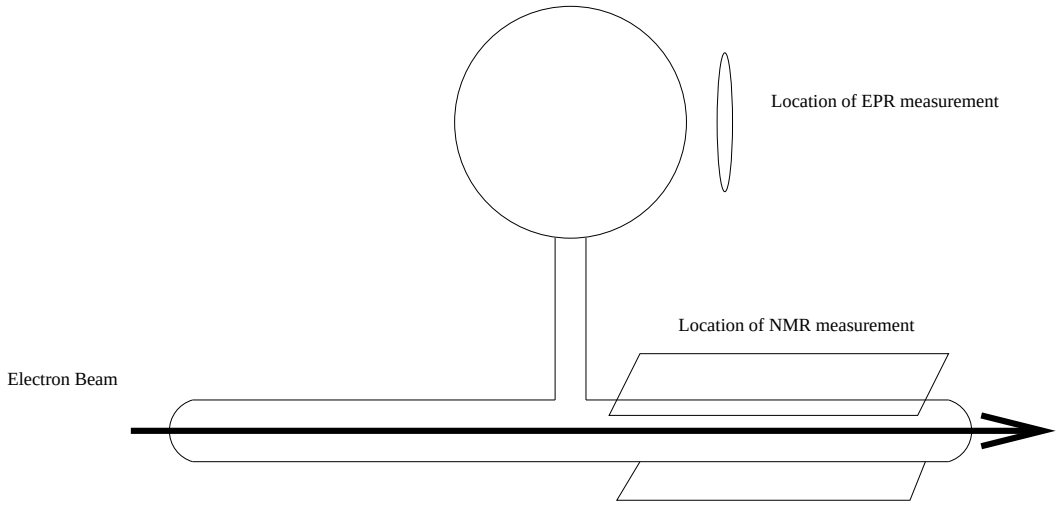

FIG. 4.18: **Relative Position of Measurements.** The NMR measurements are made in the same location as the electron beam interaction; however, the EPR measurement used to calibrate is in another location.

The main difficulty with using this method for NMR calibration lies in the relative position of the two measurements. EPR is performed in the upper of the two chambers. This is the chamber where the ^{3}He gas is polarized ("pumping chamber"). NMR measurements are performed in the lower of the two chambers; this chamber is where the electron beam interacts with the polarized gas ("target chamber"). See Fig. 4.18.

For E02-013, an additional NMR pickup coil was added. The coil was constructed at the College of William & Mary, and was added to the outside of the target oven (see Fig. 4.10). This pickup coil detected an NMR signal. However, due to its distance from the polarized cell, it was not possible to use this signal to track the polarization. Studying this signal, and in particular the ratio of this signal and the signal from the lower coils provided insight into the polarization gradient and the relative densities in the two chambers.

After the ^{3}He is polarized in the pumping chamber, it must diffuse through the thin transfer tube before reaching the target chamber. Once the ^{3}He atoms leave the pumping chamber, they are no longer affected by the polarized Rb and K. They therefore begin the spin-relaxation process. This results in a lower polarization. It must be the case that the

polarization in the target chamber is lower than the polarization in the pumping chamber. The expression that best explains our situation is:

$$P_t^\infty = P_p^\infty \frac{1}{1+\frac{\Gamma_t}{G_t}}, \tag{4.74}$$

where G_t is the diffusion rate, Γ_t is the depolarization rate and P_t^∞ and P_p^∞ are the equilibrium polarizations in the target chamber and the pumping chamber, respectively.

The factors of G_t can be separated into three groups. There are geometrical factors relating to the volume of the pumping chamber and the length and area of the transfer tube. There are factors that are intrinsic chemical properties of ^{3}He gas, and there are factors that are related to the relative density and temperature of the gas in the two chambers. The first two groups of terms are well known. The last group—the density and temperature of the gas—can fluctuate throughout the experiment and cannot be directly measured during the experiment.

Γ_t not only depends on the these temperature and density parameters; it also depends on the depolarization due to the electron beam.

Polarization Gradient Theory

As ^{3}He gas flows from one chamber to the other, it is no longer in contact with the polarized alkali metal, and starts to depolarize. We can think of a polarization current that flows from one chamber to the other.

$$J(z) = \frac{1}{2} n(z) D(z) \frac{dP}{dz} \tag{4.75}$$

where $n(z)$ is the density of helium and $D(z)$ is the diffusion coefficient. Both are functions of position along the transfer tube due to the thermal gradient. After conserving the current and integrating along the transfer tube, we get

$$J = \frac{1}{2} D_t \frac{n_t}{L} K \left(P_p - P_t\right), \tag{4.76}$$

where L is the length of the transfer tube.

K is a constant that depends on the ratio of temperatures in the target and pumping chambers, and an empirically determined diffusion parameter, m,

$$K = (2-m)\frac{1-\frac{T_p}{T_t}}{1-\left(\frac{T_p}{T_t}\right)^{2-m}} \tag{4.77}$$

for ^{3}He, $m = 1.70$ [105]. D_t is the diffusion coefficient at the target chamber.

$$D_t = D(T_\circ)\frac{n_\circ}{n_t}\left(\frac{T_t}{T_\circ}\right)^{m-1} \tag{4.78}$$

The rate of change in polarization due solely to diffusion (for each chamber) is therefore

$$\frac{dP_p}{dt} = -\frac{2JA_{\rm tr}}{n_p V_p} \tag{4.79}$$

$$\frac{dP_t}{dt} = \frac{2JA_{\rm tr}}{n_t V_t} \tag{4.80}$$

Finally, we are left with the following for the change in polarization due to diffusion:

$$\frac{dP_p}{dt} = -\frac{A_{\rm tr}}{V_p L}\frac{n_t}{n_p}D_t K\left(P_p - P_t\right) \tag{4.81}$$

$$\frac{dP_t}{dt} = \frac{A_{\rm tr}}{V_t L}D_t K\left(P_p - P_t\right), \tag{4.82}$$

where $A_{\rm tr}$ is the cross section area of the transfer tube.

This almost completely describes the polarization in the target chamber, since the polarized gas can only come from the upper chamber. The gas in the upper chamber, however, is continually polarized. The change in polarization in the upper chamber is

$$\frac{dP_p}{dt} = -\frac{A_{\rm tr}}{V_p L}\frac{n_t}{n_p}D_t K\left(P_p - P_t\right) + \gamma_{SE}^{\rm Rb}P_{\rm Rb} + \gamma_{SE}^{\rm K}P_{\rm K} - \left(\gamma_{SE}^{\rm Rb} + \gamma_{SE}^{\rm K} + \Gamma_p\right)P_p, \tag{4.83}$$

where $\gamma_{SE}^{\rm Rb}(\gamma_{SE}^{\rm K})$ is the spin-exchange rate for He-Rb(He-K).

The target chamber polarization only needs a correction due to the depolarization effects in the target chamber.

$$\frac{dP_t}{dt} = \frac{A_{\rm tr}}{V_t L} D_t K \left(P_p - P_t\right) - \Gamma_t P_t \tag{4.84}$$

For ease of notation,

$$G_t = \frac{A_{\rm tr}}{V_p L} D_t K$$

If we consider P_t^{∞} and P_p^{∞}, the equilibrium cases, then Eq. 4.84 is equal to zero. The equilibrium polarization of the target chamber in terms of the pumping chamber polarization is therefore:

$$P_t^{\infty} = \frac{P_p^{\infty}}{1 + \frac{\Gamma_t}{G_t}} \tag{4.85}$$

In principle, this equation has everything that we need to determine the relationship between the two chambers. In practice, an additional step is required. When the beam is on (or has recently been on, as is the case for most of our EPR calibrations), we need to determine the effect of the beam on the polarization.

$$\Gamma_t^{\text{beam ON}} = \Gamma_t^{\text{beam OFF}} + \Gamma_{\rm beam} \tag{4.86}$$

We do not have a direct measurement of $\Gamma_t^{\text{beam OFF}}$ for our in-hall setup. However, it can be approximated at a very high level from the data taken at the University of Virginia.

We have NMR signals at times where the beam was on and the beam was off. This will allow us to extract the polarization. Another way to write the polarization in the chambers makes this clear:

$$P_{p,t}^{\text{Beam ON}} = \frac{P_{\rm K,Rb} < \gamma_{\rm SE} >}{< \gamma_{\rm SE} > + < \Gamma > + f_t \Gamma_{\rm beam}} \tag{4.87}$$

$$P_{p,t}^{\text{Beam OFF}} = \frac{P_{\rm K,Rb} < \gamma_{\rm SE} >}{< \gamma_{\rm SE} > + < \Gamma >} \tag{4.88}$$

$$= \frac{P_{\rm K,Rb} < \gamma_{\rm SE} >}{\gamma_{\text{spin up}}} \tag{4.89}$$

where f_t is the fraction of particles in the target chamber, $\Gamma_{\rm beam}$ and $\gamma_{\text{spin up}}$ is the inverse of the spin-up time constant measured for the cell; $< \gamma_{\rm SE} >$ is the volume averaged spin-exchange rate.

Since we are measuring in the same chamber without moving the cell at all, we can take a ratio of the signals, and let the factors of flux and calibration constants cancel:

$$\frac{S^{\text{beam ON}}}{S^{\text{beam OFF}}} = \frac{P_t^{\text{beam ON}}}{P_t^{\text{beam OFF}}} = \frac{\gamma_{\text{spin up}} + f_t\Gamma_{\text{beam}}}{\gamma_{\text{spin up}}} \tag{4.90}$$

$$= 1 + \frac{f_t\Gamma_{\text{beam}}}{\gamma_{\text{spin up}}} \tag{4.91}$$

From measurements at the University of Virginia, we have measurements of $\gamma_{\text{spin up}}$, and f_t.

$$1/\gamma_{\text{spin up}} = 6.174 \pm 0.058 \text{ h},$$

$$f_t = 0.325.$$

Polarization Gradient Results

Results have been determined from the use of the temperature tests and the EPR calibrations taken with beam on and beam off. From the temperature tests we can determine the true temperature in the pumping chamber, and include that number in our diffusion model. Recall from Eqs. 4.77 and 4.78 that the diffusion parameters are temperature dependent. They are therefore corrected for each calibration. The average size of the correction is 5.7% with a spread of 2.5%. The depolarization lifetime due to the beam during Edna's running was:

$$1/\Gamma_{\text{beam}} = 50.8 \text{ hr} \pm 29.6 \text{ hr}$$

Due to the large uncertainty, the EPR calibrations use for the final numbers have come from the measurements with the beam off. For previous experiments the relevant calibration constant between NMR and EPR, c_{EPR} can be expressed in terms of the expression [100]:

$$c_{\text{EPR}} = \frac{S_{\text{NMR}}}{P_{\text{EPR}}(n_{\text{pc}}\Phi_{\text{pc}} + n_{\text{tc}}\Phi_{\text{tc}} + n_{\text{tt}}\Phi_{\text{tt}})C_\nabla C_\tau}, \tag{4.92}$$

where S_{NMR} is the signal from NMR pickup coils, P_{EPR} is the polarization measured through EPR, $n_{\text{pc}}\Phi_{\text{pc}}$ is the number of ^{3}He nuclei in the pumping chamber, multiplied by

the flux of the magnetic field from the pumping chamber seen through the NMR pickup coils. Similarly, $n_{\rm tc}\Phi_{\rm tc}$ and $n_{\rm tt}\Phi_{\rm tt}$ are the number and the flux from the target chamber and transfer tube, respectively. C_∇ is a correction factor due to holding field gradients, and C_τ is a correction due to the time constant on the lock-in amplifier.

For this experiment, we used only EPR calibrations. Therefore, the uncertainty due to the corrections C_∇ and C_τ is effectively zero. These factors affected the NMR signal shape, but were not changed for calibrations with EPR. The flux through the pickup coils did not change, since the cell did not move once mounted between the pickup coils. However, due to the uncertainty in the temperature measurements, we are concerned with the uncertainty in density. The flux is used to properly weight this uncertainty, and the uncertainty on the product of flux and density is required. Overall, the net error associated with this product is estimated to be 1%.

We are left with the error in the ratio of $S_{\rm NMR}$ to $P_{\rm EPR}$. Through a careful consideration of every calibration measurement with the cell in an equilibrium state, we have this number to the level of 1.3% uncertainty. Errors due to other density effects register at the sub–0.25% level.

Combining uncertainty from most sources, we have an error in our calibration constant of 1.67%. The uncertainty due to the temperature dependence of κ_0 from Eqn. 4.57 is 4.11% at the temperatures used for the cells Edna and Dolly. For Barbara, the Rb EPR resonance was measured, and the factor κ_0 has been measured to much greater precision. Additional error due to the uncertainty of the fit of roughly 0.6% is added to each data point. Overall, the average uncertainty (σ_P/P) for Edna was 4.47%, with a spread of roughly 0.01%. Similarly, the uncertainty on the calibration constant used for Dolly was 4.41%. For both cells, the uncertainty due to κ_0 is clearly dominant. For Barbara, fewer EPR calibration measurements lead to a larger uncertainty on the calibration constant, and the cell was moved once in place, leading to a larger uncertainty on the flux and density. The collected uncertainties are listed in Table 4.12.

	Barbara	Dolly	Edna
κ_0	1.47%	4.07%	4.11%
EPR Measurement	2.00%	0.87%	1.32%
Flux and Density	2.17%	1.00%	1.00%
NMR Fit	$\approx$ 0.6 %	$\approx$ 0.6 %	$\approx$ 0.6%
Other temperature	1.79%	0.89%	0.25%
Overall	**3.80%**	**4.41%**	**4.47%**
Days in use	8	14	48

TABLE 4.12: **Error Budget.** The sources and relative sizes of the uncertainty for the target cells.

4.6.7 Target Polarization

Edna achieved a higher in-beam polarization than any cell used in an electron scattering experiment at Jefferson Lab. At times, the cell polarization was above 50%. In addition, this cell was used continuously for over 48 days.

Two other cells, Barbara and Dolly, also achieved acceptable in-beam polarizations. A chart of the polarization is included as Fig.4.19.

4.7 Other Elements of the Target System

4.7.1 Target Ladder

The polarized target was one element of a four position target ladder. The ladder could be raised or lowered to position the required elements in the beam. The four positions were: polarized target, no target (clear path to the beam dump), optics foils, and reference cell. Items were held in place along the target ladder by attachments to a single milled sheet of Macor, a machinable glass ceramic. This sheet was on the side of the target opposite the electron spectrometer, to minimize material between the targets and the electron spectrometer. These positions and the glass ceramic can be seen in Fig. 4.20. A design drawing is included as Fig. 4.21. The target ladder was supported from above

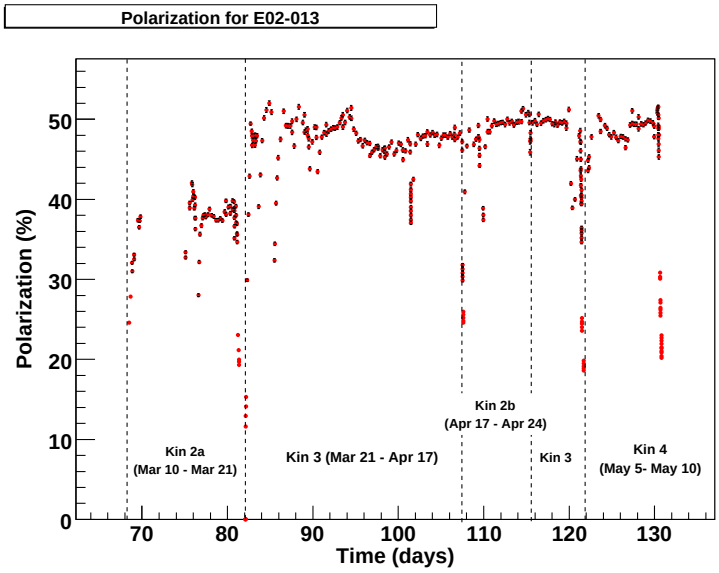

FIG. 4.19: **E02-013 Polarization Measurements.** The polarization numbers for all target cells used in E02-013, the time axis is in days from the start of the year. The error bars do not include a roughly 4% relative systematic uncertainty. Target cell "Dolly" was used for kinematic 2a, "Edna" was used for the other kinematics on this plot. The kinematics are defined in Table 3.1.

by a large ceramic tube. The target was moved by a stepper motor.

4.7.2 Reference Cell

In order to determine the nitrogen dilution, as well as the BigBite optics and neutron timing, a reference cell was used. The reference cell is a glass cell identical to the polarized cells' target chambers. A gas handling system is connected to the inlet of the cell. The cell can then be evacuated and filled with different gasses.

For analysis, there are two main differences between events from the reference cell and the polarized cell. The first is a possible misalignment of the reference cell with respect to the beamline. The polarized cell and the reference cell are mounted and aligned separately. Both are mounted to the transfer tube in the center of the cell, and as a result, there may be a rotation relative to the beamline. The effect of this possible rotation can be determined by means of the same raster check used for the polarized cell. In fact, a

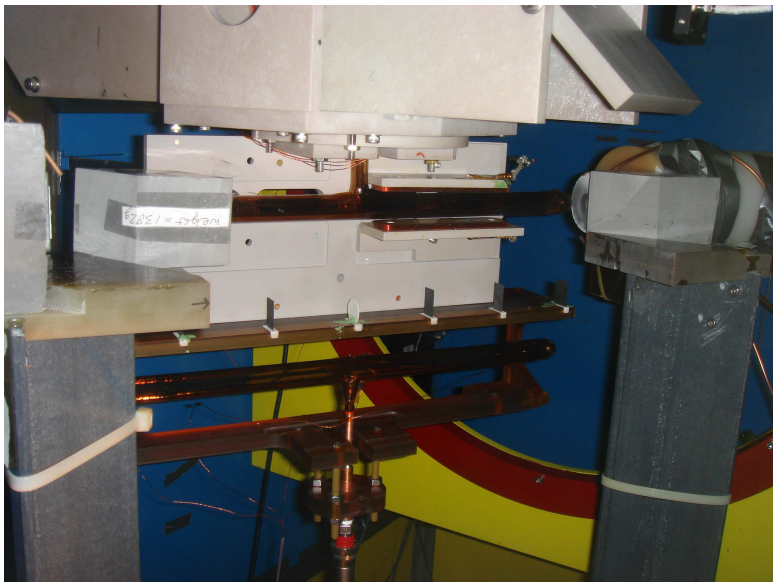

FIG. 4.20: **Target Ladder Photo.** Photograph of the target ladder, the target oven, production cell, NMR pickup coils, optics foils and reference cell are clearly visible.

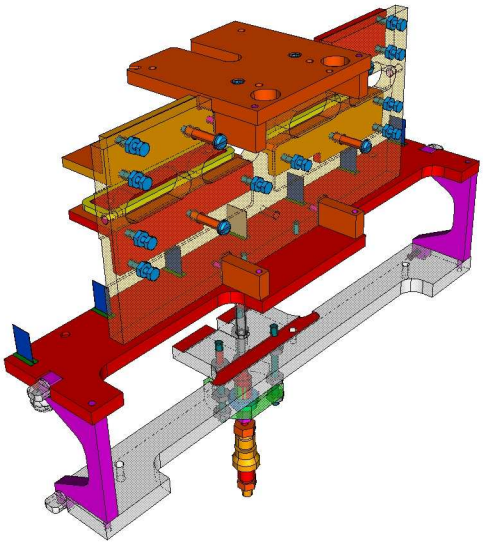

FIG. 4.21: **Target Ladder Design.** Artist rendering of the target ladder from the reverse angle, showing adjustable coil mounts.

different set of beam location parameters was used for the reference cell and the polarized cell.

The second difference is the material that a scattered nucleon must pass through to reach the neutron detector. The target ladder was designed so that there was little material on the BigBite side of the target. The target support material was located on the neutron detector side. Design considerations placed up to 1.25 cm of Macor on the neutron side of the polarized cell, but nothing on the neutron side of the reference cell. These differences were included in all simulations used for the experiment.

4.7.3 Solid Targets

A set of carbon foils were used as part of the optics determination for the BigBite detector. The set consists of 6 carbon foils (of thickness 47.70 mg/cm^2) and one BeO foil. Along the beamline, the BeO foil was located in the center of the foils and was also used as a visual verification of the location of the beam. Details of the optics calibration can be found in Ref. [67]. However, a plot demonstrating the distribution of counts along the beamline can be found in Fig. 4.22.

4.7.4 Collimators

In order to reduce the counting rate in the electron arm, high density collimators were required. In order to be effective, the collimators must be close to the target. However, most of the readily available high density materials conduct electricity. A large block of conducting material in the presence of an RF field will produce an inhomogeneity in the field, which could lead to depolarization in the target cell during NMR measurements. Our experiment used a tungsten powder combined with an epoxy. This allowed us to achieve a density of 9.5 g/cm^3, with no measurable conductivity.

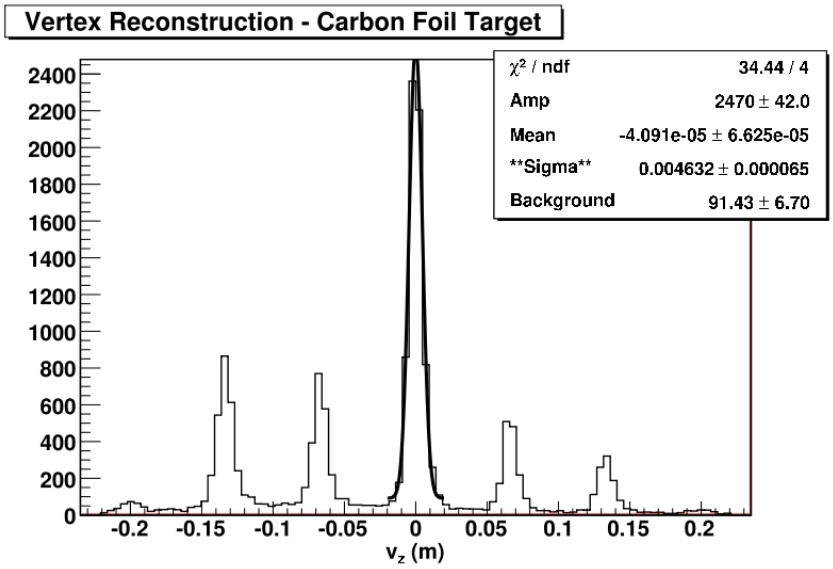

FIG. 4.22: **Optics Foils.** Data taken from electron scattering on optics foils; the number of events from foils at the same location as the target cell windows was greatly diminished due to the collimators. The axis is the position along the beamline, with 0 at the center of the target. The center foil is BeO.

4.7.5 Beamline Elements

After the electrons are produced at the machine source, they are accelerated in a vacuum system until they reach the end station scattering target. At the end of the vacuum pipe is a beryllium window. To minimize the radiative losses due to excessive material, the beryllium was made as thin as possible (0.003 in). After several weeks of running the experiment, the beryllium window failed. The window was replaced with a thicker window (0.005 in) with an aluminium foil cover, and a low flow air cooling jet was introduced.

Ideally, the beryllium window would be located as close to the target as possible, to minimize material that the electrons must pass through. The target is a glass cell filled with a high pressure gas. As such, there is a possibility of the cell rupturing and sending shards of glass into the beryllium window. Such a cell failure could penetrate the beryllium window, and send pieces of glass into the vacuum system.

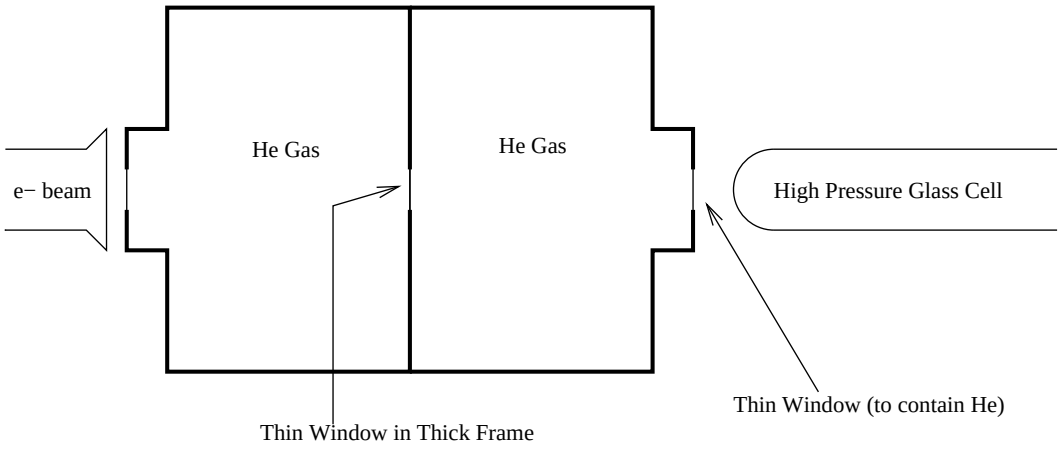

FIG. 4.23: **Helium Expansion Chamber.** Conceptual diagram of the expansion chamber used to protect the beam window from the scattered glass and high pressure gas jet.

To prevent this damage to the CEBAF electron beam pipe, a set of expansion chambers were placed before and after the target. The expansion chamber consists of a tube several times larger than the target chamber, sealed at both ends with a thin (8 μm) Al window. The center of the chamber contains a thicker Al foil (25 μm) window, set in an aluminum frame. In the event of a rupture, the scattered glass shards and high pressure gas would destroy the thin foil and proceed to the center foil. If the center foil failed, the center frame would serve as a baffle for the gas and shards. A diagram of the expansion chambers can be seen in Fig. 4.23. To minimize material between the beam pipe window and the target cell, the expansion chamber was filled with approximately 1 atm of ^{4}He (a slightly positive pressure was maintained). Two expansion chambers were used, as the electron exit from the target was also under vacuum to minimize background.

A series of tests was performed at the polarized target lab at The College of William & Mary to establish the requisite expansion chamber volumes and foil thicknesses [106, 107]. The final design was modified to fit the geometry of the target (Fig. 4.24).

Although thoroughly tested and installed for E02-013, these chambers were never used, as the experiment did not experience a cell rupture.

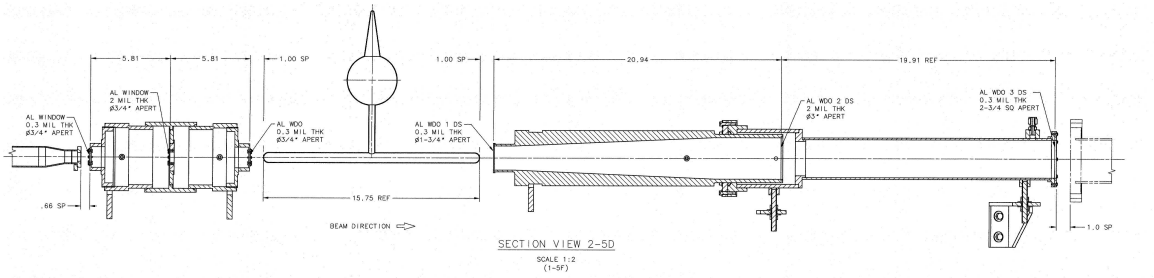

FIG. 4.24: **Beamline Elements.** Diagram demonstrating the location and design of various beamline elements.

CHAPTER 5

Analysis of Electron Scattering Data

The goal of the analysis is to select quasi-elastic scattered neutrons and form the double polarized asymmetry. Additionally, the proper dilution factors must be determined to translate the measured asymmetry into the physics asymmetry. Once the asymmetry is determined, the ratio of G_E/G_M for the neutron can be extracted.

The asymmetry is defined as the difference of the neutrons in the two helicity states divided by the sum of all neutron events:

$$A_{\rm obs} = \frac{N_+ - N_-}{N_+ + N_-} \tag{5.1}$$

where N_+ is the number of neutron events with positive electron helicity and N_- is the number of neutron events with negative electron helicity. These true neutron events are determined from the measured events:

$$A_{\rm raw} = \frac{\Delta}{\Sigma} = \frac{\Delta_n + \Delta_{\rm back} + \Delta_p + \Delta_{\rm N_2} + \Delta_{\rm other}}{\Sigma_n + \Sigma_{\rm back} + \Sigma_p + \Sigma_{\rm N_2} + \Sigma_{\rm other}}, \tag{5.2}$$

where Σ and Δ denote sums and differences, respectively. Σ_n and Δ_n are the neutron sums and differences, $\Sigma_{\rm back}$ is the sum of events from the random background, Σ_p are proton events detected as neutrons, $\Sigma_{\rm N2}$ are events from the small quantity of nitrogen required to produce a polarized ^{3}He cell, and $\Sigma_{\rm other}$ are events from other sources.

These contributions can be separated from each other through the use of dilution factors:

$$D_{\rm back} = 1 - \frac{\Sigma_{\rm back}}{\Sigma} = \frac{\Sigma_n + \Sigma_p + \Sigma_{\rm N_2} + \Sigma_{\rm other}}{\Sigma} \quad (5.3)$$

$$D_{\rm N_2} = 1 - \frac{\Sigma_{\rm N_2}}{\Sigma - \Sigma_{\rm back}} = \frac{\Sigma_n + \Sigma_p + \Sigma_{\rm other}}{\Sigma_n + \Sigma_p + \Sigma_{\rm N_2} + \Sigma_{\rm other}} \quad (5.4)$$

$$D_p = 1 - \frac{\Sigma_p}{\Sigma - \Sigma_{\rm back} - \Sigma_{\rm N_2}} = \frac{\Sigma_n + \Sigma_{\rm other}}{\Sigma_n + \Sigma_p + \Sigma_{\rm other}} \quad (5.5)$$

$$D_{\rm FSI} = 1 - \frac{\Sigma_p}{\Sigma - \Sigma_{\rm back} - \Sigma_{\rm N_2} - \Sigma_p} = \frac{\Sigma}{\Sigma_n + \Sigma_{\rm other}}, \quad (5.6)$$

where $D_{\rm back}$ is the background dilution, $D_{\rm N2}$ is the nitrogen dilution, D_p is a dilution factor to correct for proton events detected as neutrons, and $D_{\rm FSI}$ is the dilution factor accounting for interactions with the scattered neutron and the final state of the ^{3}He nucleus. The product of the dilutions is

$$D_{\rm back} D_{\rm N_2} D_p D_{\rm FSI} = \frac{\Sigma_n}{\Sigma}. \quad (5.7)$$

The uncorrected asymmetry can be written in terms of these dilution factors and the measured asymmetry,

$$A_{\rm raw} = D_{\rm back} D_{\rm N_2} D_p D_{\rm FSI} A_{\rm obs} + \frac{\Delta_{\rm back} + \Delta_p + \Delta_{\rm N_2} + \Delta_{\rm other}}{\Sigma} \quad (5.8)$$

where $A_{\rm obs} = \frac{\Sigma_n}{\Delta_n}$. Since the nitrogen is unpolarized, $\Delta_{\rm N_2} = 0$.

The asymmetry due to the neutron form factors ($A_{\rm phys}$) is diluted in the observed asymmetry, by a number of factors. The relation between the observed asymmetry ($A_{\rm obs}$), and the physics asymmetry ($A_{\rm phys}$) is

$$A_{\rm obs} = P_e \cdot P_n \cdot A_{\rm phys}, \quad (5.9)$$

where P_e is the polarization of the electron beam (see Sec. 3.2.3), P_n is the polarization of the neutron (a combination of the measured ^{3}He polarization and the theoretical polarization of the neutron in the nucleus).

By combining 5.8 and 5.9, $A_{\rm phys}$ can be written in terms of the raw asymmetry, the dilution factors, and the relative asymmetries:

$$A_{\rm phys} = \frac{A_{\rm raw} - \frac{\Delta_{\rm back}}{\Sigma} - \frac{\Delta_p}{\Sigma} - \frac{\Delta_{\rm other}}{\Sigma}}{P_e P_n D_{\rm back} D_{\rm N_2} D_p D_{\rm FSI}}. \tag{5.10}$$

Finally, an analysis of the acceptance and the kinematics of the scattered particles allows the extraction of the ratio $\Lambda = G_E/G_M$ from this asymmetry, see Eqs. 1.2 and 1.3:

$$\begin{aligned} A_{\rm phys} &= -\Lambda \cdot \frac{2\sqrt{\tau(\tau+1)}\tan(\theta/2)\sin\theta^*\cos\phi^*}{\Lambda^2 + (\tau + 2\tau(1+\tau)\tan^2(\theta/2))} \\ &\quad - \frac{2\tau\sqrt{1+\tau+(1+\tau)^2\tan^2(\theta/2)}\tan(\theta/2)\cos\theta^*}{\Lambda^2 + (\tau + 2\tau(1+\tau)\tan^2(\theta/2))}. \end{aligned} \tag{5.11}$$

5.1 Podd – The Hall A ROOT Based Analyzer

The primary software tool used for this analysis is the Hall A ROOT-based analyzer, referred to as "Podd". Podd is a C++ based object-oriented analysis package. This allows an intuitive approach, where individual detector and beamline elements can be calibrated and incorporated to produce physics variables.

E02-013 used many new pieces of equipment. These changes were incorporated into Podd using an experiment-specific library "AGen." This library contains the code necessary to provide tracking in BigBite, cluster reconstruction in the neutron arm, timing information, and other experiment specific code.

Podd is built on the ROOT software package developed at CERN. ROOT is a set of object-oriented frameworks designed to handle large amounts of data in an efficient manner. Data is defined as a set of objects, which allows access to attributes of these objects without touching the bulk of the experimental data [108].

5.2 Flow of Analysis Process

Signals from the BigBite detectors, the neutron arm, and beamline elements including injector hardware (*e.g.*, helicity information, raster information, etc.) are combined and decoded in the first pass through Podd. After the raw event decoding, tracking, cluster finding, and first-pass optics are performed, the data are output into "trees", the ROOT data structure [108].

With these trees, calibrations based on the data may be performed. For example, revised BigBite optics from carbon foil runs can be determined. Hydrogen data may be used to properly calibrate the neutron detector's timing. Some physics variables can be determined at this time, but for the most part, this output is used to build and refine the AGen libraries.

The ROOT files were then generated again with the revised calibrations. The second pass data now has usable physics information. At this point, an asymmetry could be formed by placing cuts on the data. In most cases, however, additional processing was performed by individual users using the Podd framework. This processing determined the values for variables related directly to the analysis of E02-013 data, including the missing momentum, the charge identification, etc.

Dilution information, theoretical inputs, and beam and target polarization were added to a final analysis of the data. The output of this analysis is the physical asymmetry, the average energy transfer seen by the detectors, and finally, the ratio G_E^n/G_M^n. A schematic of this analysis is included as Fig. 5.1.

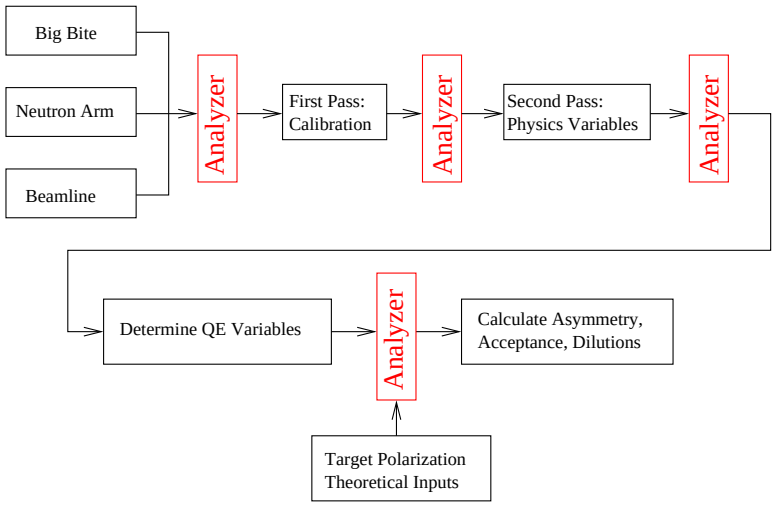

FIG. 5.1: **Flow Chart for Analysis.** Information is collected from the electron detector, neutron detector, and from various sources along the beamline. The information is then processed by the Hall A analyzer to produce kinematic variables. Cuts can be placed on these variables and the asymmetry can be formed.

5.3 Selection of Quasi-Elastic Events

5.3.1 Helicity Selection

The beam helicity changed every 33.3 ms, and this information was included in the datastream. However, to check for systematic uncertainties, a half-wave plate was also used to make an additional periodic change in the helicity of the beam. In addition, the target polarization direction was changed periodically as a check for target-related systematic effects. The sign of the observed asymmetry is the product of the sign of the physics asymmetry due to the form factors and the sign of the beam helicity and the sign of the target spin orientation.

An accurate record of the beam and target signs is essential for properly combining the asymmetries from the different runs. The asymmetry in the raw BigBite triggers serves as a check on the product of the beam and target helicity signs. These asymmetries provide a clean selection of the sign of the asymmetry, as seen in Fig. 5.2. Details of the

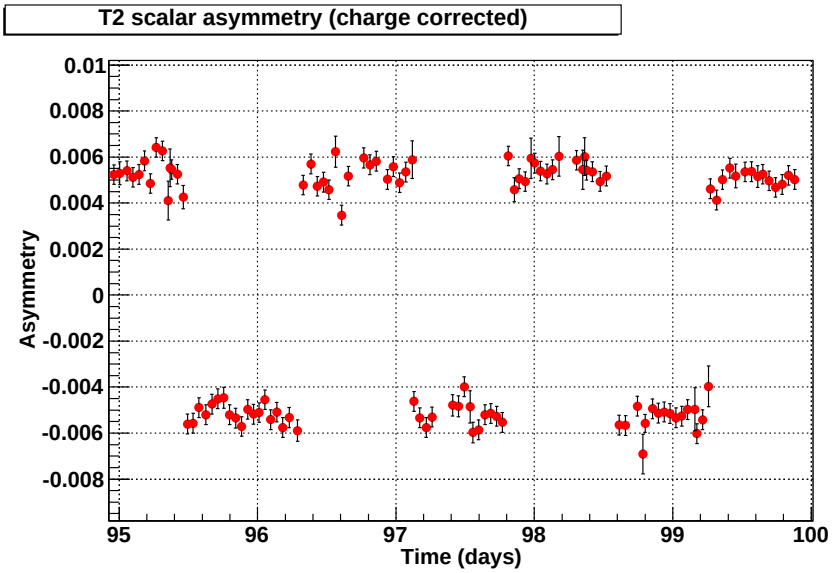

FIG. 5.2: **Asymmetry sign per run.** Asymmetry as seen in the BigBite only trigger, used to combine asymmetries for each run.

variables used to generate the asymmetry follow.

5.3.2 Electron Selection

Electron events were selected from all possible events in the BigBite detector by using tracking information, as well as calorimeter information.

Negatively charged particles are identified through the tracking information. Information on the location of the scattering is also determined through the tracking information. The polarized target is a well defined location, and the events can be selected to restrict the analysis to events originating in the target (Fig. 5.3). The tracking information is calibrated by using the carbon foils target seen in Fig. 4.22, as well as the hydrogen target.

The particle identification is further narrowed by placing a cut on the energy deposited in the pre-shower. The clear separation of these events helped to determine the location of the cut (Fig. 3.14).

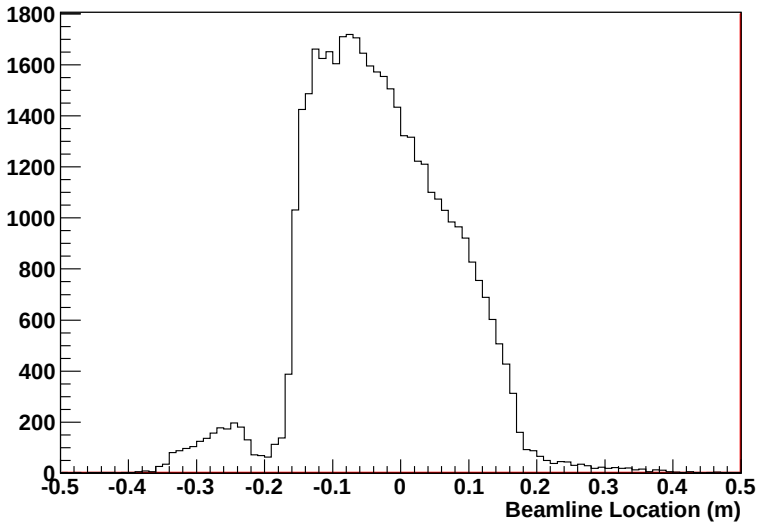

FIG. 5.3: **Pre-shower $>$ 500 Channels Scattered from a Polarized Target.** Primarily electron events distribution along the length of the polarized target. Although the end windows are blocked by collimators, scattering from the air gap between the beamline window and the target window is apparent.

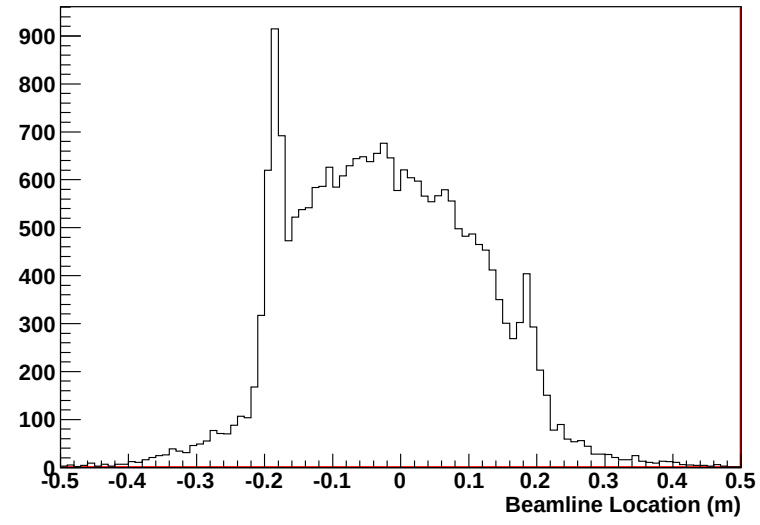

FIG. 5.4: **Pre-shower $<$ 500 Channels Scattered from a Polarized Target.** Glass end windows, which are blocked for electrons, can be seen clearly.

Non-electron events that deposit little energy in the pre-shower detector are generally pion events. This property of pions can be exploited to determine the location of the end windows from the data collected in the BigBite spectrometer. While the location of the windows is well defined, confirmation of this location from electron events is difficult due to the presence of collimators placed around the target. These collimators are included to reduce the number of events detected by the BigBite spectrometer originating from the end window. By looking at pion events, both the location of the end windows and the efficacy of the collimators are confirmed (Fig 5.4).

Invariant Mass

The invariant mass of the reaction can be determined from the initial energy and the momentum of the scattered electron:

$$W^2 = (p_{(i,\mathrm{nucl})} + q)^2 \tag{5.12}$$

where W is the invariant mass, $p_{(i,\mathrm{nucl})}$ is the initial 4-momentum of the nucleon and q is the 4-momentum transferred from the electron to the nucleon. The calculation of W assumes that $p_{(i,\mathrm{nucl})}$ is the 4-momentum for a nucleon at rest, $p_{(i,\mathrm{nucl})} = (m_N, \vec{0})$. In the case of a bound neutron, this is not always true. However, this assumption allows for a separation of electrons quasi-elastically scattered from a neutron and inelastic events in the BigBite spectrometer. A loose cut is placed on these events, and the latter selection of events with relatively small missing momenta further justifies this cut. A comparison of the invariant mass spectrum with and without the inelastic cuts on the neutron arm is seen in Fig. 5.5.

5.3.3 Hadron Selection

Nucleons are selected by the time-of-flight (TOF) method. From the beam energy and the electron tracking information, the energy transferred by the electron can be deter-

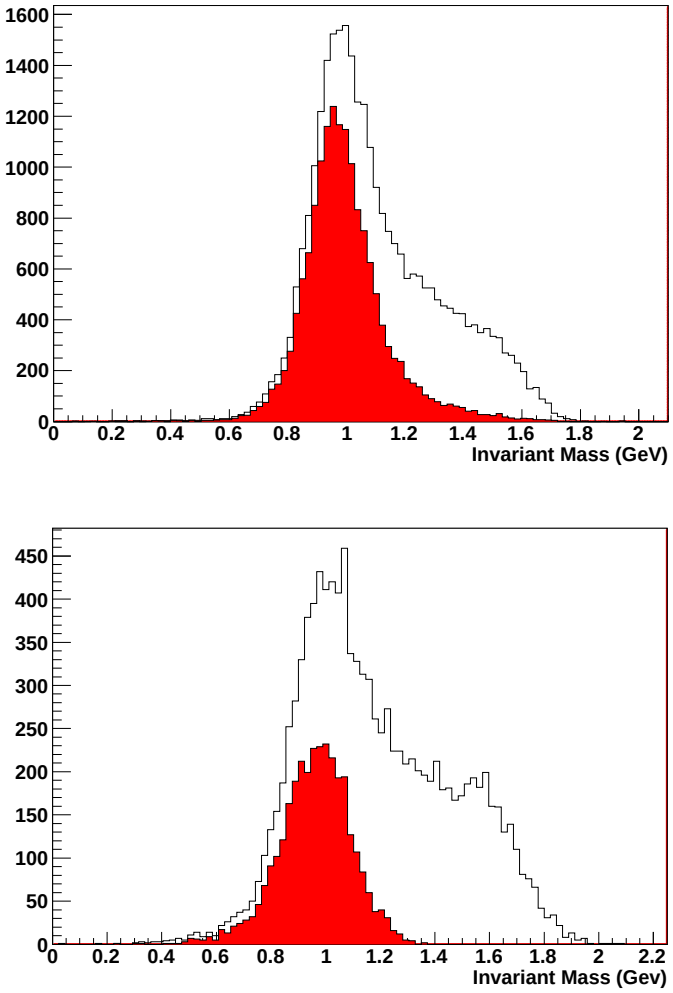

FIG. 5.5: **Invariant Mass Spectra.** Invariant mass spectra for electrons $Q^2 = 1.7\ \mathrm{GeV}^2$ on top, $Q^2 = 2.5\ \mathrm{GeV}^2$ below. Many inelastic events were removed through a coincidence requirement, allowing for a clean selection of quasi-elastic events.

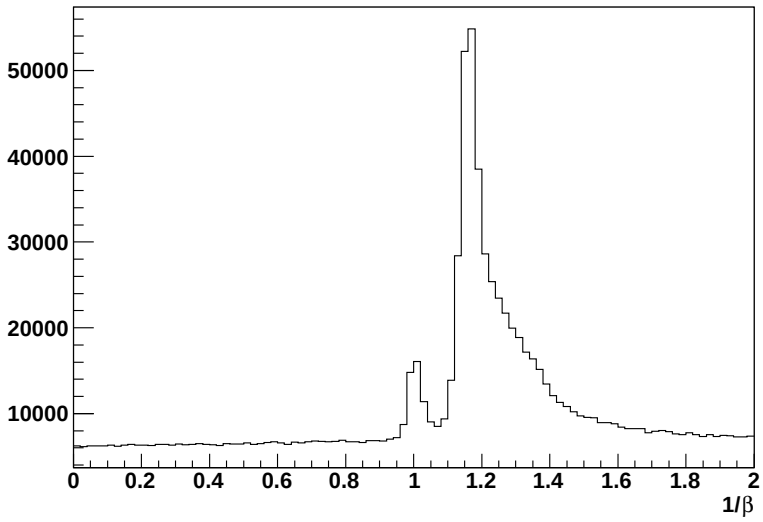

FIG. 5.6: **Time of flight (in units of $1/\beta$).** Time of flight spectrum with no cuts on invariant mass or perpendicular momentum. Prompt photons can be seen at $1/\beta = 1$.

mined. By assuming elastic scattering from a stationary target of known mass, a predicted time of flight can be determined. Events which are located in time close to the predicted time of flight are considered as having quasi-elastically scattered from the target by the electron detected in the BigBite spectrometer. The relatively large distance of the neutron detector from the target (9.6 – 12 m) and the timing precision of the neutron detector (300 ps) allowed for a clean separation of the high speed neutrons originating from the target and other events.

Missing Momentum

The neutron is considered as being quasi-free for this analysis. The variable which serves as a measure of the quasi-freedom is the missing momentum. This variable is calculated from the momentum observed in the electron spectrometer and the momentum of the scattered hadron in the neutron detector. The difference between the momentum transferred from the electron and the TOF momentum is the missing momentum. As it

is a vector, it is instructive to consider the missing momentum in the direction of the transferred momentum separately from the transverse momentum,

$$p_{\mathrm{miss},\parallel} = \hat{q} \cdot (\vec{q} - \vec{p}_{\mathrm{TOF}}) \tag{5.13}$$

$$p_{\mathrm{miss},\perp} = \left|\vec{q} - \vec{p}_{\mathrm{TOF}} - p_{\mathrm{miss},\parallel}\hat{q}\right| \tag{5.14}$$

where $\vec{q}$ is the momentum transfer and p_{TOF} is the momentum determined from the time of flight. These missing momentum components have different interpretations in the neutron arm. $p_{\mathrm{miss},\parallel}$ is related to the difference in time of flight between the time predicted by the q-vector and the observed time, these spectra can be seen in Fig. 5.7. $p_{\mathrm{miss},\perp}$ is related to the spacial separation from the predicted location in the neutron arm and the observed location of the hit. The missing perpendicular momentum spectrum as a function of invariant mass is presented in Fig. 5.8. The missing momentum describes the initial momentum of the nucleon within the nucleus. Nucleons with small initial momentum values are considered quasi-free for this analysis. The selection of low values of missing momentum suppresses the effects of final state interactions.

Missing Mass

The combination of separate cuts on the missing momentum and the cuts on the scattered electron serve to effectively identify quasi-elastic scattered nucleons. However, this sample can be contaminated by inelastic events, primarily π^0 and $\pi^{\pm}$ electro-production. A small fraction of these events can be included in the sample of good hadron candidates.

A strict cut on the missing mass for the reaction $^3\mathrm{He}(e,e'n)X$ can separate inelastic events from quasi-elastic events. Missing mass is defined as:

$$m^2_{\mathrm{miss}} = (P_i + qp_f)^2, \tag{5.15}$$

where P_i is the initial 4-momentum of the target nucleus, q is the 4-momentum transfer, and p_f is the measured 4-momentum of the scattered particle. In the impulse approximation, the missing mass for quasi-elastic scattering is the mass of the two remaining

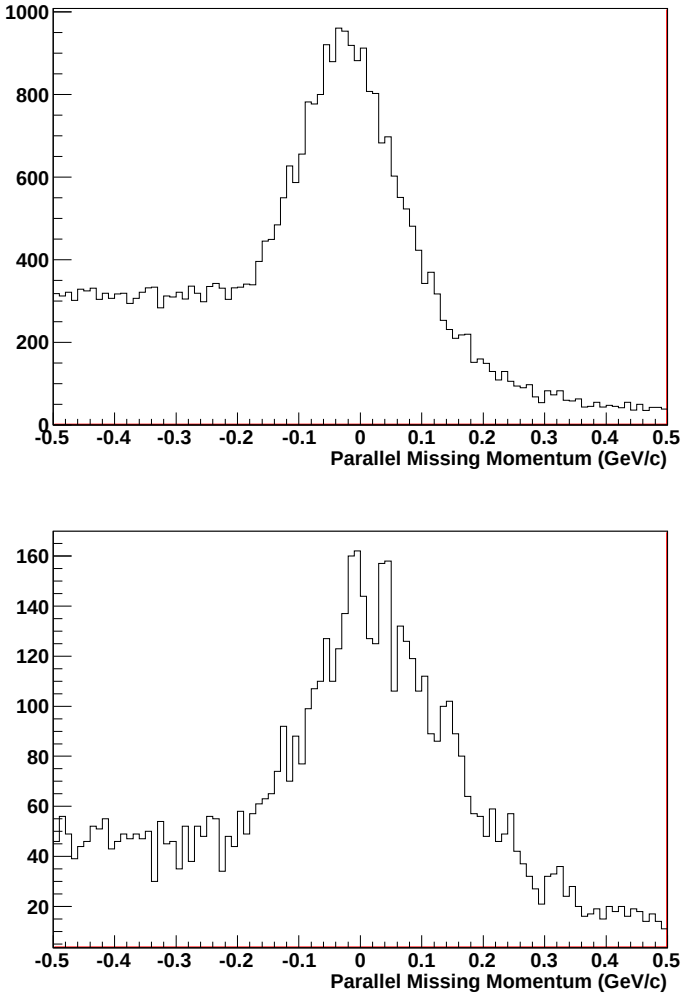

FIG. 5.7: **Parallel Missing Momentum Spectra.** Missing parallel momentum, determined primarily through the time of flight, $Q^2 = 1.7\ \mathrm{GeV}^2$ on top, $Q^2 = 2.5\ \mathrm{GeV}^2$ below. Events have been selected for electrons and a loose cut on invariant mass was applied.

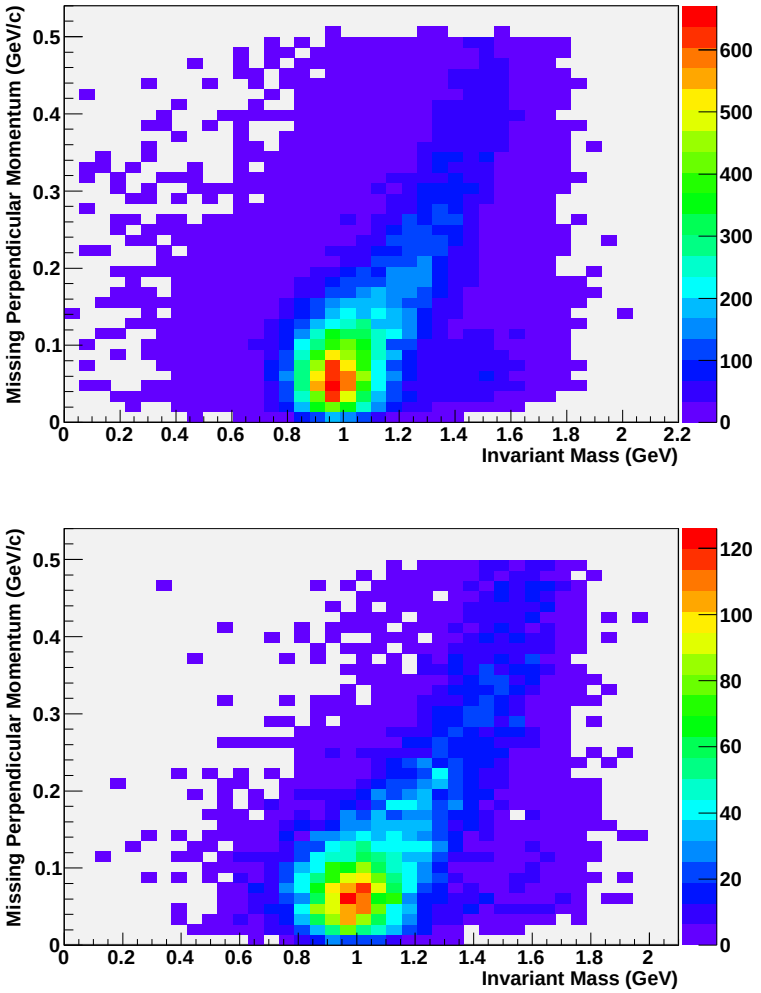

FIG. 5.8: **Invariant Mass vs. Missing Perpendicular Momentum.** $Q^2 = 1.7$ GeV^2 on top, $Q^2 = 2.5$ GeV2 below. A cut on missing parallel momentum, and selecting electrons have been applied.

nucleons. In the case of pion electro-production, there is an additional mass due to the additional pion.

Therefore, restricting the sample to only events with a missing mass smaller than 2 GeV (approximately the mass of two nucleons and a pion) effectively rejects events which originate through pion electro-production. This restriction increases in importance as the transferred 4-momentum increases. The dominant contribution to the resolution of this variable is the resolution of the neutron TOF. In practice, this is used to further restrict the neutron sample to quasi-elastically scattered neutrons. Plots of the missing mass against the invariant mass are seen in Fig. 5.9.

5.3.4 Neutron Selection

Neutron events are separated from the general hadron events by using two thin layers of scintillating material before the main hadron detector. Charged particles passing through this material will produce a signal; uncharged events have a smaller probability of producing a signal. Events that produce a signal in the hadron detector but do not produce a signal in the veto layer are considered to be neutron events.

In practice, there are many events in the hadron detector at any time due to high accidental rates. The analysis used the location of the hadron signal to further narrow the region in which a veto event was expected.

For every hit in the neutron detector, the analysis script loops over all tracks to identify possible veto hit candidates. First, the neutron cluster x position (vertical position) is used to identify possible veto hits. Veto hits that satisfy the inequality

$$|x_{\rm clus} - x_{\rm veto} - x_0| < \Delta x \tag{5.16}$$

are further examined to determine if the time of the hit in the veto corresponds with the time of the cluster:

$$|t_{\rm veto} - t_{\rm clus}| \equiv \Delta t. \tag{5.17}$$

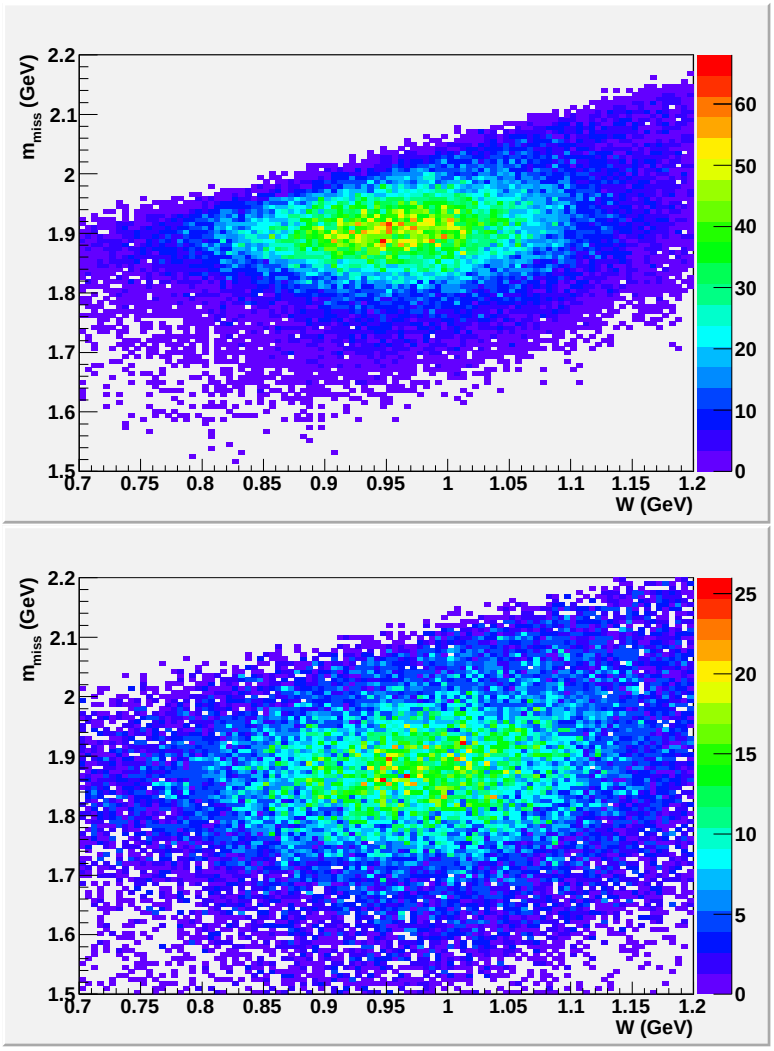

FIG. 5.9: **Missing Mass Spectra.** Missing mass plotted against the invariant mass, $Q^2 = 1.7\ \mathrm{GeV}^2$ on top, $Q^2 = 2.5\ \mathrm{GeV}^2$ below. Quasi-elastic events have an invariant mass W near the mass of the nucleon, and a missing mass near twice the mass of the nucleon. Inelastic events are excluded by requiring $m_{\mathrm{miss}} < 2$.

In Eq. 5.16, $x_{\rm clus}$ is the position of the neutron cluster, $x_{\rm veto}$ is the position of the veto hit and x_0 is an offset determined by the data. Δx is determined from proton events (scattering from a H_2 target), and is 70 cm for these data. Similarly, in Eq. 5.17, $t_{\rm clus}$ is time of the hit in the neutron detector. The veto time, $t_{\rm veto}$ is not merely the time in the veto TDC, but has been corrected for the position of the hit in the neutron cluster.

If Δt is within a time determined from proton data (20 ns), then the event in the neutron detector is considered charged. If Δt is larger than the time window, but within the deadtime associated with the veto electronics, then the charge of the event is considered to be undetermined. Events in the neutron detector which do not have a hit in the veto detector within the good location and timing window are considered neutral.

5.4 Background Subtraction

A plot of the time-of-flight indicates the presence of a random, flat background. This is particularly clear if the plot uses units of $1/\beta$, where $\beta = v/c$. In such a plot, events arriving at the detector with $1/\beta < 1$ must be random background as they correspond to events moving faster than the speed of light. This becomes clearer if the plot does not contain the cuts on invariant mass or missing perpendicular momentum. In such a plot (Fig. 5.6), events from photons detected in the neutron detector are seen as a distribution at $1/\beta = 1$.

By shifting the time-of-flight to the unphysical region, and applying the same cuts (W, time-of-flight, particle identification, etc.), the random background can be approximated. In Fig. 5.10, the background is indicated in red.

Missing q-perpendicular

Shifting the time-of-flight spectrum will change the variables that depend on time-of-flight. In addition, the time-of-flight background may not be flat through the physical

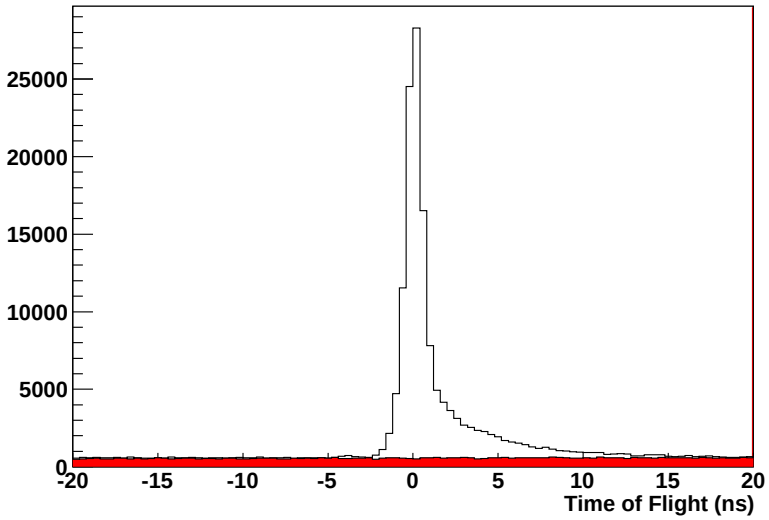

FIG. 5.10: **Background Events.** The time-of-flight spectrum, with relevant cuts. The time-shifted events used to determine the background are indicated in red.

region. The kinematics of the experiment are such that we can define a time-independent variable. Since the experiment is a measurement at a relatively high momentum transfer, and the ^{3}He nucleus is weakly bound, quasi-elastic neutrons should primarily move in the direction of the momentum transfer. True coincident events should be limited to small variations from the momentum transfer, and the deviation from the momentum direction can be tracked by using a variable which we call $q_\perp$, defined as

$$q_\perp = \sqrt{\vec{q}\cdot\vec{p} - |\vec{p}|^2}. \tag{5.18}$$

This can be clearly seen in Fig. 5.11. The results plotted against the time-of-flight can be seen in Fig. 5.12.

5.5 Nitrogen Dilution

Operation of the polarized target requires 1-2% by number of the gas in the cell to be nitrogen. Even though the percentage is small, the effect on the polarization could be up to

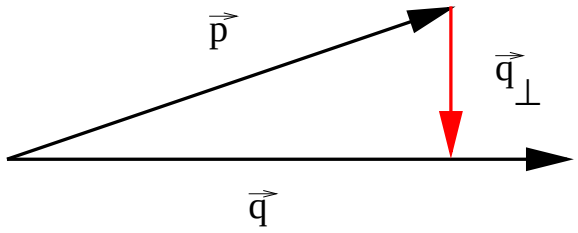

FIG. 5.11: **Diagram of $q_\perp$.** This variable is used to determine whether neutron events originated from a quasi-elastic scattering.

14%, due to the relative difference in the number of protons and neutrons. By restricting the analysis to a selection of quasi-elastic neutrons with small missing momentum, the effect is reduced. The exact value is determined by analyzing data collected from the reference cell filled with different pressures of nitrogen.

The asymmetry correction factor is determined through a measurement of the event yield due to nitrogen from a nitrogen-filled reference cell. Then, the effect is scaled to the effect on the target cell by ratio of the densities of nitrogen in the reference and target cells. The dilution factor is determined by comparing the yields in the detectors from the reference cell and the polarized cell.

$$D = 1 - \frac{\rho_{\rm targ}(\mathrm{N}_2)}{\rho_{\rm ref}(\mathrm{N}_2)} \frac{Y^{(\mathrm{N}_2)}}{Y^{(\mathrm{N}_2+{}^3\mathrm{He})}} \tag{5.19}$$

where $\rho_{\rm ref}(\mathrm{N}_2)$ is the density of nitrogen in the reference cell, $\rho_{\rm targ}(\mathrm{N}_2)$ is the density of nitrogen in the target cell (a fraction of the total target density), and Y is the yield. The ratio $\rho_{\rm ref}(\mathrm{N}_2)/\rho_{\rm targ}(\mathrm{N}_2)$ has a temperature dependence. It is clear, however, that the ratios $\rho_{\rm targ}(\mathrm{N}_2)/Y^{(\mathrm{N}_2+\mathrm{He})}$ and $\rho_{\rm ref}(\mathrm{N2})/Y^{(\mathrm{N}_2)}$ do not, since they are the yields scaled by factors of the target luminosity. Therefore, the overall dilution factor is temperature independent and can be applied to all ^{3}He runs.

These yields are the total number of events, after appropriate cuts have been applied, and normalized with charge, live-time, and detector efficiencies. The same cuts are applied to both nitrogen reference cell and polarized ^{3}He cell runs. The yields can be

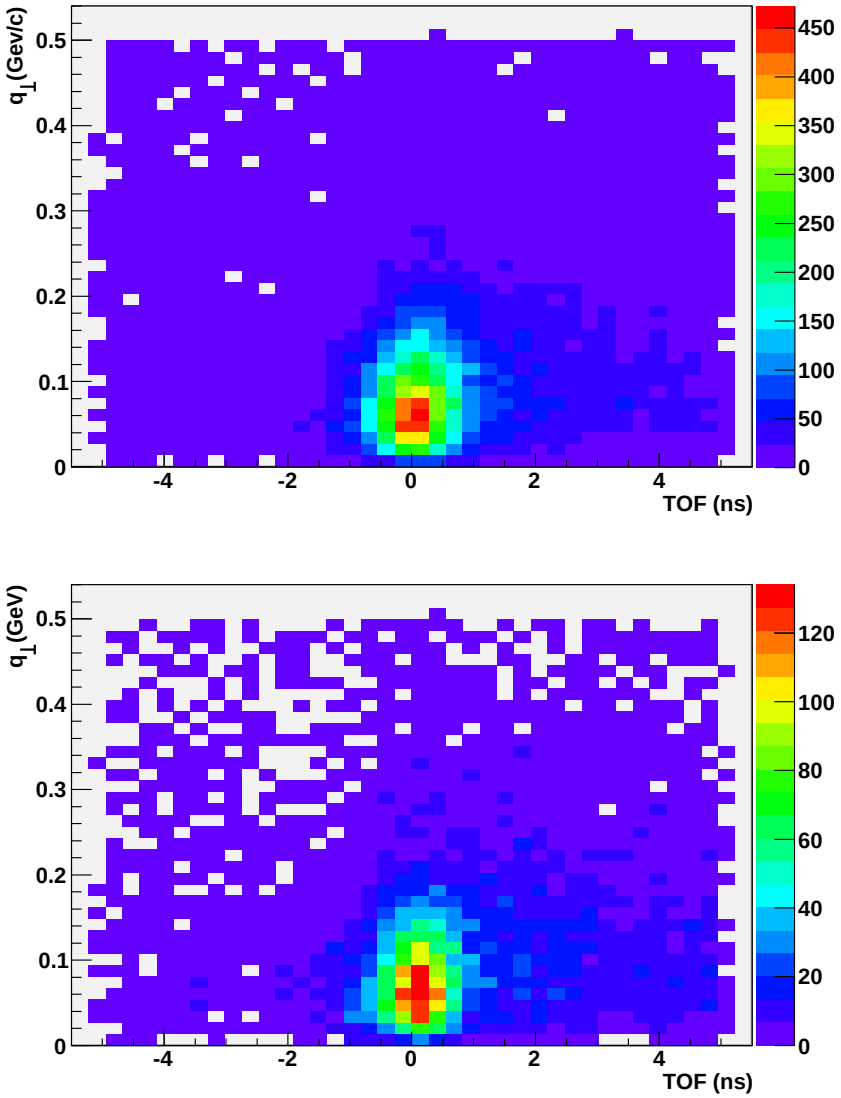

FIG. 5.12: $q_\perp$ **vs. Time of Flight.** The variable $q_\perp$ plotted against time of flight. The $Q^2 = 1.7\ \mathrm{GeV}^2$ plot is on top, and $Q^2 = 2.5\ \mathrm{GeV}^2$ is below.

Q^2 (GeV^2)	$p_\parallel$ (MeV/c)	$p_\parallel$ (MeV/c)	D_{N_2}
1.7	250	150	0.960
2.5	250	150	0.939
3.5	400	150	0.947

TABLE 5.1: **Nitrogen Dilution for Different Kinematics.** The nitrogen dilution factor varies with Q^2 and with the cuts on missing momentum.

expressed as

$$Y = \frac{N_{\rm cuts}}{Q \cdot LT \cdot \epsilon}, \tag{5.20}$$

where Q is the accumulated charge, LT is the live-time (combined electronic and computer), ϵ is the combined detector efficiencies, and $N_{\rm cuts}$ is the number of events after all cuts are applied. These cuts are determined by the ^{3}He analysis.

Previous documents on this topic have made reference to a one-track correction factor (*e.g.* [81]). This factor is only necessary for inclusive measurements. The coincidence requirement of our experiment imposes the requirement that each event have a well-defined track.

The nitrogen dilution factor must be determined for each kinematic as it is dependent on the $N_2(e,e'n)$ cross section. It is also dependent on the cuts on perpendicular and parallel missing momenta, as the nuclear effects for ^{3}He and N_2 are different. For $Q^2 = 1.7$ GeV^2, using momentum cuts: $|p_\parallel| < 250$ MeV/c and $|p_\perp| < 150$ MeV/c, $D_{N_2} = 0.943 \pm 0.02$. Results for other kinematics can be seen in Table 5.1.

5.6 Proton to Neutron Conversion

The neutron detector identifies hadrons and uses the veto counters to determine if the event was charged or uncharged. The particle must travel through materials and may experience an interaction before reaching the veto plane. The effect of this interaction can be determined through a thorough Monte Carlo analysis of the scattering process. In

addition, insight may be gained through the analysis of data collected on several different nuclear targets during the experiment.

5.6.1 Formalism

The goal of this analysis is to develop a correction factor for misidentified protons that can be applied to the neutron asymmetry after appropriate cuts are implemented. This correction factor can be written

$$D_{p/n} = 1 - \frac{N_p^n}{N_n^n} = 1 - \frac{\sigma_p}{\sigma_n}\frac{\eta_p^n}{\eta_n^n}, \tag{5.21}$$

where p/n is the ratio of protons to neutrons in the target nucleus, σ_n (σ_p) is the cross section for free neutrons (protons). The efficiency of detecting a neutron as a neutral particle is η_n^n, and the efficiency of detecting a proton as a neutral particle is η_p^n. Ratios of the efficiency can be determined by comparing data taken from different targets. The factors of N_n^n and N_p^c are then generalized,

$$N_n^n \propto (A-Z)\sigma_n\eta_n^n \tag{5.22}$$

$$N_p^c \propto Z\sigma_p\eta_p^c \tag{5.23}$$

where $A(Z)$ is the atomic mass(number) of the target, N_n^n is the number of neutrons detected as neutral particles and N_p^c is the number of particles originating as protons that are detected as charged particles (*i.e.,* with an associated veto hit).

Ratios of the number of particles detected as a charged or uncharged hadron can be written as

$$R_{n/c} = \frac{N^n}{N^c} = \frac{(A-Z)\sigma_n\eta_n^n + Z\sigma_p\eta_p^n}{(A-Z)\sigma_n\eta_n^c + Z\sigma_p\eta_p^c} \tag{5.24}$$

During the experimental run, targets of ^{3}He, H_2, N_2, and mixed C/BeO were used. These provide data from targets with different ratios of $(A-Z)/Z$. It is useful, therefore,

to re-write Eq. 5.24 in terms of these ratios:

$$R_{n/c} = \frac{\frac{(A-Z)}{Z}\frac{\sigma_n}{\sigma_p}\left(\eta_n^n/\eta_p^c\right) + \left(\eta_p^n/\eta_p^c\right)}{\frac{(A-Z)}{Z}\frac{\sigma_n}{\sigma_p}\left(\eta_n^n/\eta_p^c\right) + 1} \tag{5.25}$$

This can be used to specify the ratios relevant to each target, given as

$$R_{n/c}^{\mathrm{H}} = \eta_p^n/\eta_p^c \tag{5.26}$$

$$R_{n/c}^{\mathrm{N,C,BeO}} = \frac{\frac{\sigma_n}{\sigma_p}\left(\eta_n^n/\eta_p^c\right) + \left(\eta_p^n/\eta_p^c\right)}{\frac{\sigma_n}{\sigma_p}\left(\eta_n^c/\eta_p^c\right) + 1} \tag{5.27}$$

$$R_{n/c}^{^3\mathrm{He}} = \frac{\frac{\sigma_n}{\sigma_p}\left(\eta_n^n/\eta_p^c\right) + \frac{p}{n}\left(\eta_p^n/\eta_p^c\right)}{\frac{\sigma_n}{\sigma_p}\left(\eta_n^c/\eta_p^c\right) + \frac{p}{n}} \tag{5.28}$$

In terms of the ratios of efficiencies:

$$\frac{\eta_p^n}{\eta_p^c} = R_{\mathrm{H}} \tag{5.29}$$

$$\frac{\eta_n^n}{\eta_p^c} = \frac{\sigma_p}{\sigma_n}\frac{\frac{p}{n}R_{\mathrm{N}}(R_{^3\mathrm{He}} - R_{\mathrm{H}}) - R_{^3\mathrm{He}}R_{\mathrm{N}} + R_{^3\mathrm{He}}R_{\mathrm{H}}}{R_{\mathrm{N}} - R_{^3\mathrm{He}}} \tag{5.30}$$

$$\frac{\eta_n^c}{\eta_p^c} = \frac{\sigma_p}{\sigma_n}\left(\frac{\left(\frac{p}{n}-1\right)\left(R_{^3\mathrm{He}} - R_{\mathrm{H}}\right)}{R_{\mathrm{N}} - R_{^3\mathrm{He}}} - 1\right) \tag{5.31}$$

The ratios of efficiencies are precisely what is required to write the dilution factor in terms of the charged and uncharged ratios of counts for different targets:

$$D_{p/n} = 1 - \frac{R_{\mathrm{H}}(R_{\mathrm{N}} - R_{^3\mathrm{He}})}{\frac{p}{n}R_{\mathrm{N}}(R_{^3\mathrm{He}} - R_{\mathrm{H}}) - R_{^3\mathrm{He}}R_{\mathrm{N}} + R_{^3\mathrm{He}}R_{\mathrm{H}}} \tag{5.32}$$

5.6.2 Rate Dependence

The efficiencies of detecting a particle as charged or uncharged are highly dependent on the rate of events in the veto detectors. The identification of uncharged particles is determined by the failure of the veto detector to fire. The veto detector could fail to fire because the particle has no charge, or, it could fail to fire because of electronic or processor deadtime. Such deadtime is rate dependent, and an analysis of this issue based on the probability of detecting a veto trigger in the correct timing window has been performed. Conversely, a neutral event could be associated with an accidental veto hit. In practice, the latter is a larger effect than the deadtime effect.

5.6.3 The Ratio: p/n

The formalism leaves the term p/n for ^{3}He intact throughout the derivation of the dilution factor. The neutron and proton have different momentum distributions in the ^{3}He nucleus. Therefore, the relative densities of protons and neutrons in the ^{3}He nucleus appear to be a function of initial momentum selected. The ratio of p/n for the choice of initial momenta used for E02-013 has been calculated based on the work of Schiavilla *et al.* [109, 110], and its effect on the final value of G_E^n has been determined.

A calculation of the single nucleon momentum distributions in ^{3}He is presented in Fig. 5.13. A ratio of the proton to neutron as a function of momentum was then calculated (Fig. 5.14). The ratio does converge to 2/1, when the momentum reaches approximately 600 GeV/c. This calculation was used as the basis of a study into the effect of cuts on the perpendicular and parallel momentum (Fig. 5.15) on the ratio of proton to neutron.

These cuts represent limits on the momenta in the initial state. However, we measure the proton and neutron momenta through detectors that have finite resolutions. As a result, the initial momenta may be different from the detected momenta. A Monte Carlo simulation was performed to estimate the size of the effect of detector acceptance on the ratio of p/n. The resolution effects were simulated by the addition of random noise with the same width as the detector resolution. Then cuts were placed on the final momentum. An example can be seen in Fig. 5.16.

For each set of momentum cuts, the ratio must be calculated before the dilution factor can be used (Table 5.2). The difference in the ratio is between 6-10% depending on the cuts. The effect on the extracted G_E^n is 3-5%.

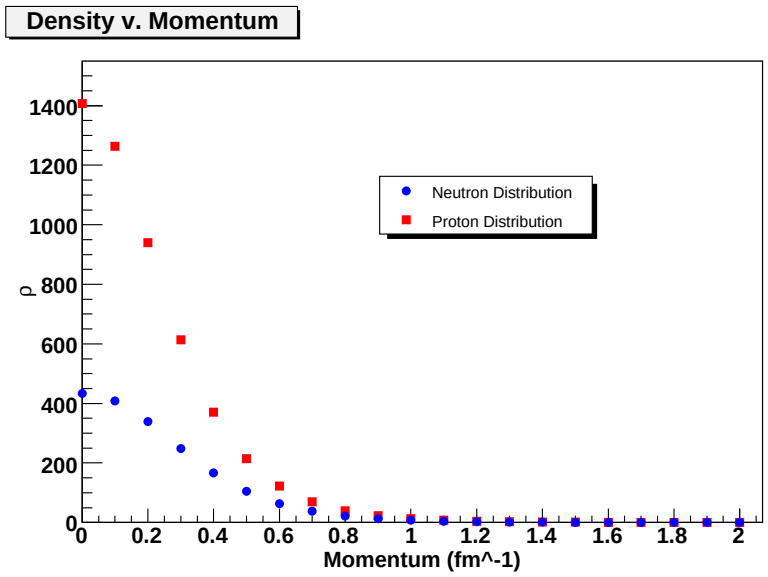

FIG. 5.13: **Nucleon Momentum Density in ^{3}He.** Normalized density as a function of momentum.

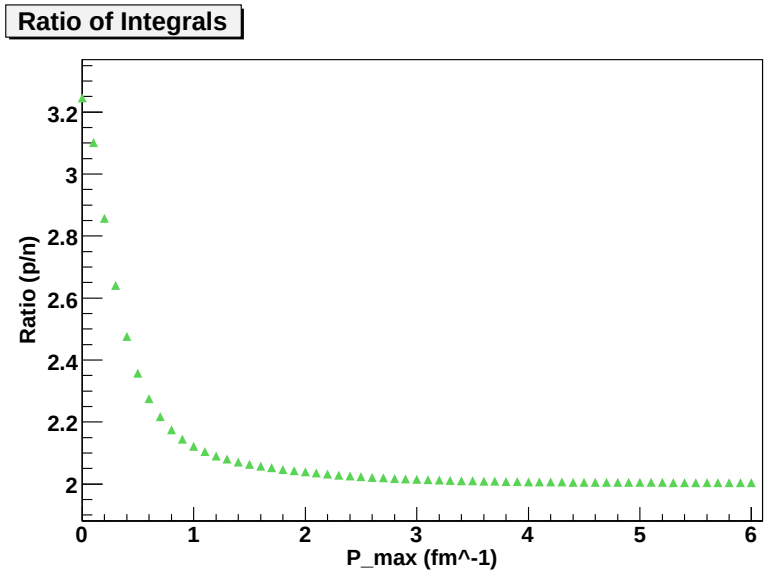

FIG. 5.14: **Ratio p/n as a Function of Momentum.** Calculation provided by R. Schiavilla [109], converted to ratio of protons to neutrons for different momenta.

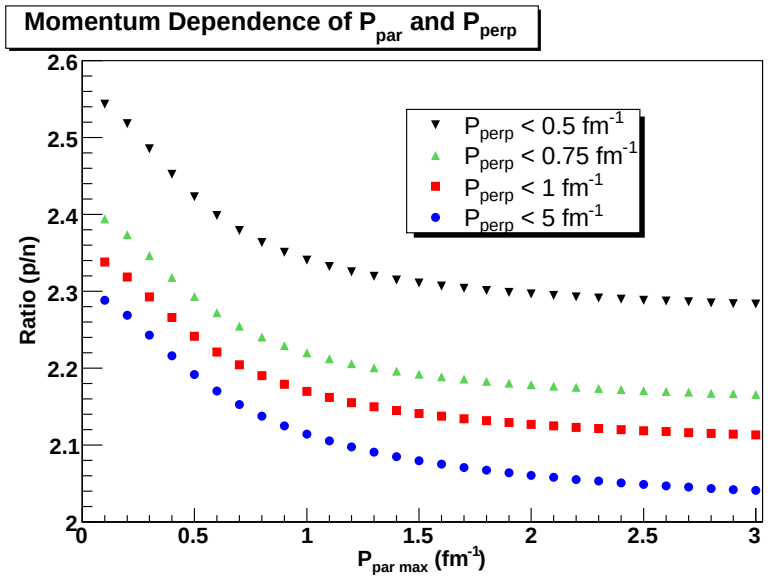

FIG. 5.15: **Ratio p/n with Varying Momentum Cuts.** Ratio p/n presented as a function of limits on components of momentum.

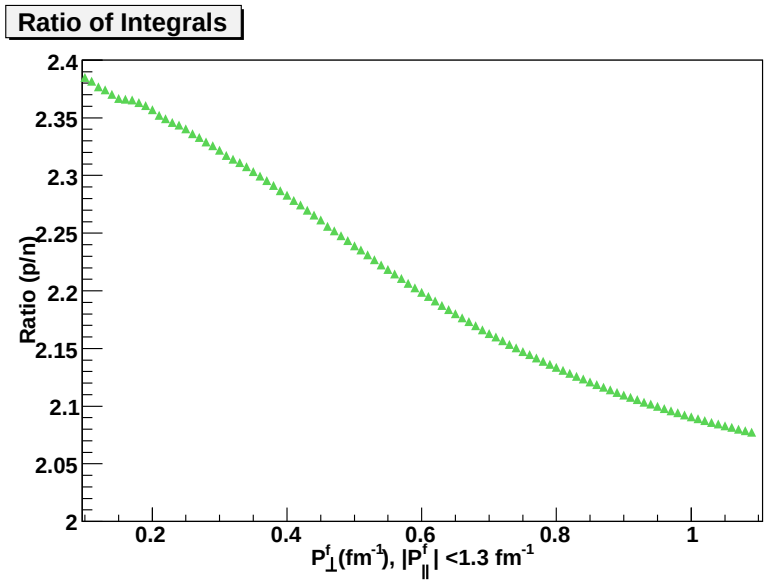

FIG. 5.16: **Ratio p/n with Resolution Effects.** Resolution effects are added through Monte Carlo methods, resulting in a simulation of the p/n ratio based on cuts in the detector.

Q^2	$p_\perp$	$p_\parallel$	p/n
1.7	< 150 MeV/c	< 250 MeV/c	2.15
2.5	< 150 MeV/c	< 250 MeV/c	2.15
3.5	< 150 MeV/c	< 400 MeV/c	2.14

TABLE 5.2: **Table of Ratio p/n.**The p/n ratio calculated for specific missing momentum cuts, using Monte Carlo calculations that take resolution effects into account.

5.7 Run Summation

For the most part, corrections to the asymmetry can be calculated for the entire dataset. However, for corrections such as beam and target polarization, the corrections must be applied to each run individually. Recalling Eq. 5.9,

$$A_{\rm obs} = P_e \cdot P_n \cdot D_{\rm N_2} \cdot D_{\rm background} \cdot D_{\rm FSI} \cdot A_{\rm phys},$$

the factors $D_{\rm N_2}$, $D_{\rm background}$, and $D_{\rm FSI}$ can be calculated for the entire run. Once these factors have been determined, a physical asymmetry can be calculated for each run. These asymmetries can be combined by summing the asymmetries, weighted by the inverse statistical uncertainty squared:

$$A_{\rm phys} = \frac{\sum_i \frac{A_{{\rm phys},i}}{\sigma_i^2}}{\sum_i \frac{1}{\sigma_i^2}}. \tag{5.33}$$

The uncertainty on the weighting includes the statistical uncertainty as well as the uncertainty on the beam and target polarizations. If statistical uncertainty alone were considered, this would reduce to a weighting by the number of events in each run. The statistical uncertainty, $\sigma_{\rm stat} = \frac{1}{\sqrt{N}}$, introduced to Eq. 5.33 yields:

$$A_{\rm phys} = \frac{\sum_i A_{{\rm phys},i} N_i}{\sum_i N_i} \tag{5.34}$$

5.8 Final State Interactions

The goal of E02-013 is to measure the electric form factor of the neutron. Since no free neutron target could be used for this experiment, a neutron bound in a nucleus must be used. The selection of small missing momentum insures that the neutron is quasi-free. Even with this condition, the neutron may interact with the protons in the nuclear medium as it becomes free.

These final state interactions have been calculated. The method used is the Generalized Eikonal Approximation (GEA) [111]. This is a general form of the eikonal approximation introduced by R. Glauber [112, 113]. In general, four main processes contribute to the semi-exclusive scattering reaction. The largest term is the impulse approximation, in which the virtual photon knocks-out the bound neutron. In this case, neither the nucleon nor the virtual photon interact with the other members of the bound system. The second largest contributor to the cross section are the final state interactions, which contributes when the struck nucleon interacts with the residual nuclear system before being detected. Smaller contributions come from less direct interactions with the virtual photon. In the case of meson exchange currents—the third process—the virtual photon interacts with a meson exchanged between two nucleons in the system. In the fourth process, the virtual photon interacts with the nucleon to produce a Δ-isobar before decaying.

The contributions from meson exchange current (MEC) and isobar current (IC) become smaller at higher momentum transfers (such as those in E02-013). The strength of the interaction scales as $1/Q^4$. In GEA calculations, the final state interactions remain constant with momentum transfer at our values of Q^2.

At energies higher than a few GeV, the GEA gives rise to a reduction theorem. High energy particles propagating in the nuclear medium cannot interact with the same bound nucleon a second time after interacting with another bound nucleon. In the case of an electron scattering with a high Q^2 from a ^{3}He nucleus, the struck nucleon can either

not interact with the residual system, interact with one or the other nucleons, or interact with both nucleons. It cannot re-interact, so the potentially infinite series of scattering amplitudes is truncated after double scattering. These amplitudes can then be calculated from the well known proton-proton or proton-neutron scattering cross sections [111].

These total cross sections are constant with momentum above approximately 1.5 GeV/c, approximately the momentum of the lowest momentum neutrons studied in E02-013.

GEA calculations performed for this experiment include the finite acceptance of the experimental setup. While calculating the contribution from FSI, the effective neutron polarization for E02-013 kinematics was also calculated. Exclusivity and the kinematic restrictions cause the effective polarization to be larger than for inclusive measurements [114].

5.9 Extraction of G_E^n

From Eq. 5.11, it is apparent that the extraction of $\Lambda = G_E^n/G_M^n$ is not straightforward, as it enters into the expression for $A_{\rm phys}$ non-linearly. Eq. 5.11 can be written simply by separating the kinematic terms from the terms dependent on G_E^n:

$$A_{\rm phys} = \frac{\Lambda B + C}{\Lambda^2 + D} \tag{5.35}$$

where

$$\begin{aligned} B &= -2\sqrt{\tau\left(\tau+1\right)}\tan\left(\theta/2\right)\sin\theta^*\cos\phi^* \\ C &= -2\tau\sqrt{1+\tau+\left(1+\tau\right)^2\tan^2\left(\theta/2\right)}\tan\left(\theta/2\right)\cos\theta^* \\ D &= \Lambda^2 + \left(\tau + 2\tau\left(1+\tau\right)\tan^2\left(\theta/2\right)\right) \end{aligned}$$

Following the derivation in Ref. [115], this simplified form suggests expansion in a

series in Λ about $\Lambda = 0$:

$$\begin{aligned} A_{\rm phys} &\approx (B\Lambda + C)(1/D - \Lambda^2/D^2 + \Lambda^4/D^2) \\ &= \frac{C}{D} + \frac{B}{D}\Lambda - \frac{C}{D^2}\Lambda^2 - \frac{B}{D^2}\Lambda^3 + \frac{C}{D^3}\Lambda^4 + \frac{B}{D^3}\Lambda^5 \\ &= T_0(\theta,\phi) + T_1(\theta,\phi)\Lambda + T_2(\theta,\phi)\Lambda^2 + T_3(\theta,\phi)\Lambda^3 + T_4(\theta,\phi)\Lambda^4 + T_5(\theta,\phi)\Lambda^5 \end{aligned}$$

where

$$\begin{aligned} T_0 &= \frac{C}{D} \\ T_1 &= \frac{B}{D} \\ T_2 &= -\frac{C}{D^2} \\ T_3 &= -\frac{B}{D^2} \\ T_4 &= \frac{C}{D^3} \\ T_5 &= \frac{B}{D^3}. \end{aligned}$$

5.9.1 Angular Acceptance

The physical asymmetry

$$A_{\rm phys} = \frac{\sigma_+ - \sigma_-}{\sigma_+ + \sigma_-} = \frac{\Delta}{\Sigma} \tag{5.36}$$

is related to the observed asymmetry through factors of polarization and other dilution factors (Eq. 5.9). It is also determined by the acceptance over which the measurement is made:

$$A_{\rm obs} = \frac{N_+ - N_-}{N_+ + N_-} = PD\frac{\int d\Omega_e \Delta(\theta,\phi)\epsilon(\theta,\phi)}{\int d\Omega_e \sigma_0(\theta,\phi)\epsilon(\theta,\phi)},$$

where Δ and Σ are defined in Eq. 5.36, P and D are the polarization and dilution factors seen in Eq. 5.9, and $d\Omega_e$ is the electron acceptance as a function of the electron angle. For an asymmetry measurement, only the relative acceptance is required,

$$\epsilon(\theta,\phi) = \frac{dN_+(\theta,\phi) + dN_-(\theta,\phi)}{2\Sigma(\theta,\phi)}, \tag{5.37}$$

where $dN_{+(-)}(\theta,\phi)$ is the number of events with positive (negative) helicity in a given angular bin, which then allows the asymmetry to be written:

$$A_{\rm obs} = PD\frac{\int d\Omega_e \frac{\Delta(\theta,\phi)}{2\Sigma(\theta,\phi)}(dN_+(\theta,\phi)+dN_-(\theta,\phi))}{\int d\Omega_e \frac{1}{2}(dN_+(\theta,\phi)+dN_-(\theta,\phi))}. \tag{5.38}$$

Or, in terms of the sum of elastic events:

$$A_{\rm obs} = \frac{PD}{N_+ + N_-}\sum_{\rm elastic\ events}\frac{\Delta(\theta,\phi)}{\Sigma(\theta,\phi)} \tag{5.39}$$

Returning to the expansion of the physical asymmetry in terms of Λ, the physical asymmetry can be rewritten in terms of the averages of the expansion coefficients,

$$A_{\rm phys} = \frac{1}{PD}\frac{N_+ - N_-}{N_+ + N} = \left[\overline{T}_0 + \overline{T}_1\Lambda + \overline{T}_2\Lambda^2 + \overline{T}_3\Lambda^3 + \overline{T}_4\Lambda^4 + \overline{T}_5\Lambda^5\right]. \tag{5.40}$$

5.9.2 Determination of Q^2

This expansion allows determination of the value of Q^2 averaged over the acceptance. If a linear dependence of Λ on Q^2 is assumed over the acceptance, then Λ can be written

$$\Lambda(Q^2) = \Lambda_n + \alpha(Q^2 - Q_n^2), \tag{5.41}$$

where Λ_n is Λ at a nominal value of Q^2 (*i.e.*, Q_n^2), and α is the slope of Λ with respect to Q^2. Using this expression in Eq. 5.40 and retaining only the terms linear in α,

$$\frac{\Delta}{\sigma_0}(Q^2) = \frac{\Delta}{\sigma_0}(Q_n^2) + T_1\alpha(Q^2 - Q_n^2). \tag{5.42}$$

Writing the asymmetry by averaging over the acceptance:

$$\overline{A} = A(Q_n^2) + \alpha(\overline{T_1 Q^2} + \overline{T_1}Q_n^2). \tag{5.43}$$

The acceptance averaged value of the asymmetry is the same as the asymmetry at a nominal value of Q^2, if the nominal value of Q^2 is determined by:

$$Q_n^2 = \frac{\overline{T_1 Q_n^2}}{\overline{T_1}}. \tag{5.44}$$

5.9.3 Acceptance Averaged G_E^n

The kinematics for E02-013 were carefully chosen so that the momentum transfer direction was nearly perpendicular to the polarization direction of the target. In that case, and since $\Lambda \ll 1$, Λ can be written

$$\Lambda_0 = \frac{A_{\rm phys} - \overline{T_0}}{\overline{T_1}}. \tag{5.45}$$

Even though the angle of polarization was not perpendicular to the momentum transfer, this approximation is good to 5%. A higher accuracy can be achieved by including higher order terms in Eq. 5.40. An accuracy better than 1% can be acheived by using the first 5 terms. The roots of this function can be determined numerically. Newton's method is applied to find the roots of:

$$f(\Lambda) = A_{\rm phys} - \left(\overline{T}_0 + \overline{T}_1\Lambda + \overline{T}_2\Lambda^2 + \overline{T}_3\Lambda^3 + \overline{T}_4\Lambda^4 + \overline{T}_5\Lambda^5\right). \tag{5.46}$$

The method uses the approximation:

$$\Lambda_{i+1} = \Lambda_i - \frac{f(\Lambda)}{f'(\Lambda)}, \tag{5.47}$$

using the first order approximation of Eq. 5.45 as the starting point.

CHAPTER 6

Results

The results of the analysis allow the physical asymmetry to be calculated. Recall Eq. 5.10:

$$A_{\rm phys} = \frac{A_{\rm raw} - \frac{\Delta_{\rm back}}{\Sigma} - \frac{\Delta_p}{\Sigma} - \frac{\Delta_{\rm other}}{\Sigma}}{P_e P_n D_{\rm back} D_{\rm N_2} D_p D_{\rm FSI}}$$

From this asymmetry, the ratio $\Lambda = G_E^n/G_m^n$ can be determined, from Eq. 5.11:

$$\begin{aligned} A_{\rm phys} &= -\Lambda \cdot \frac{2\sqrt{\tau\left(\tau+1\right)}\tan\left(\theta/2\right)\sin\theta^*\cos\phi^*}{\Lambda^2 + \left(\tau + 2\tau\left(1+\tau\right)\tan^2\left(\theta/2\right)\right)} \\ &\quad - \frac{2\tau\sqrt{1+\tau+\left(1+\tau\right)^2\tan^2\left(\theta/2\right)}\tan\left(\theta/2\right)\cos\theta^*}{\Lambda^2 + \left(\tau + 2\tau\left(1+\tau\right)\tan^2\left(\theta/2\right)\right)} \end{aligned}$$

6.1 Cut Selection

To properly identify quasi-elastic events, cuts were placed on data collected in the electron spectrometer and the neutron detector.

6.1.1 Electron Cuts

The first set of cuts applied to the full data set selects only events caused by quasi-elastic scattered electrons originating from the target. The electron beam interacts with

Variable	Low	High
Target Position	-0.18 m	0.18 m
Pre-Shower	400 channels	—
BigBite Momentum	0.5 GeV/c	1.4 GeV/c
Invariant Mass	0.7 GeV/c^2	1.15 GeV/c^2

TABLE 6.1: **Electron Arm Cuts.** Cuts on the data to restrict events to quasi-elastically scattered events originating from the target.

the polarized ^{3}He gas within the target portion of the glass cell. This cell is centered at the origin of the hall coordinate system. The long dimension of the cell is 40 cm and is aligned with $\hat{z}$. Cuts to ensure that the electrons were scattered from the cell are $\pm$18 cm in the $\hat{z}$-direction. Loose cuts on the momentum and the location of the hit in the drift chamber serve to reduce the random background.

As described in Sec. 5.3.2, good electron events are separated from pions by using the pre-shower calorimeter. A cut is made so that only events depositing an energy greater than 400 channels (143 MeV) are included. In a perfectly elastic interaction, the invariant mass, as measured by the scattered electron, would be equal to the mass of the neutron. A wide cut is permitted on the data taken in this experiment, as the neutron arm data helps restrict the selection of inelastic events. The electron cuts are summarized in Table 6.1.

6.1.2 Missing Parallel Momentum

In practice, the limits on missing parallel momentum can be replaced by limits on the time-of-flight with respect to the expected time-of-flight of the neutron. For each electron event, an expected time-of-flight can be determined from the calculated q-vector. The difference between the expected time of the hit in the neutron arm and the actual time of the hit is attributable to the motion of the neutron within the ^{3}He nucleus. In other words, this difference in timing is simply the missing parallel momentum expressed in units of time. Figure 6.1 demonstrates the equivalence of the cuts on the two variables. There is

Variable	Low	High
TOF difference	-1 ns	1 ns
$q_\perp$	0	150 MeV/c
Fiducial, x-direction	-1.6 m	1.0 m
Fiducial, y-direction	-0.87 m	0.2 m

TABLE 6.2: **Neutron Arm Cuts.** When combined with the electron arm cuts, these restrict the events to events originating from the target, which scattered from a quasi-free neutron.

some variation due to the lengths of the different paths taken by the particles.

6.1.3 Other Neutron Cuts

The time-of-flight is the primary cut to restrict the data to quasi-elastic scattered neutron events. However, a cut on the missing momentum perpendicular to the direction of flight further restricts the data set to quasi-elastic scattered events. This is accomplished by placing a cut on the variable $q_\perp$, as discussed in Sec. 5.4.

Finally, a loose fiducial cut is used to restrict events to the region of the neutron detector that is well covered by the veto plane. The neutron cuts are summarized in Table 6.2

6.2 Dilution Factors

Once the proper neutron sample has been identified, the dilution factors need to be calculated to extract the physical asymmetry.

6.2.1 Background

Random background can be accounted for by applying a shift to the time-of-flight spectrum so that events in an unphysical region are used to approximate the random background in the good time-of-flight sample.

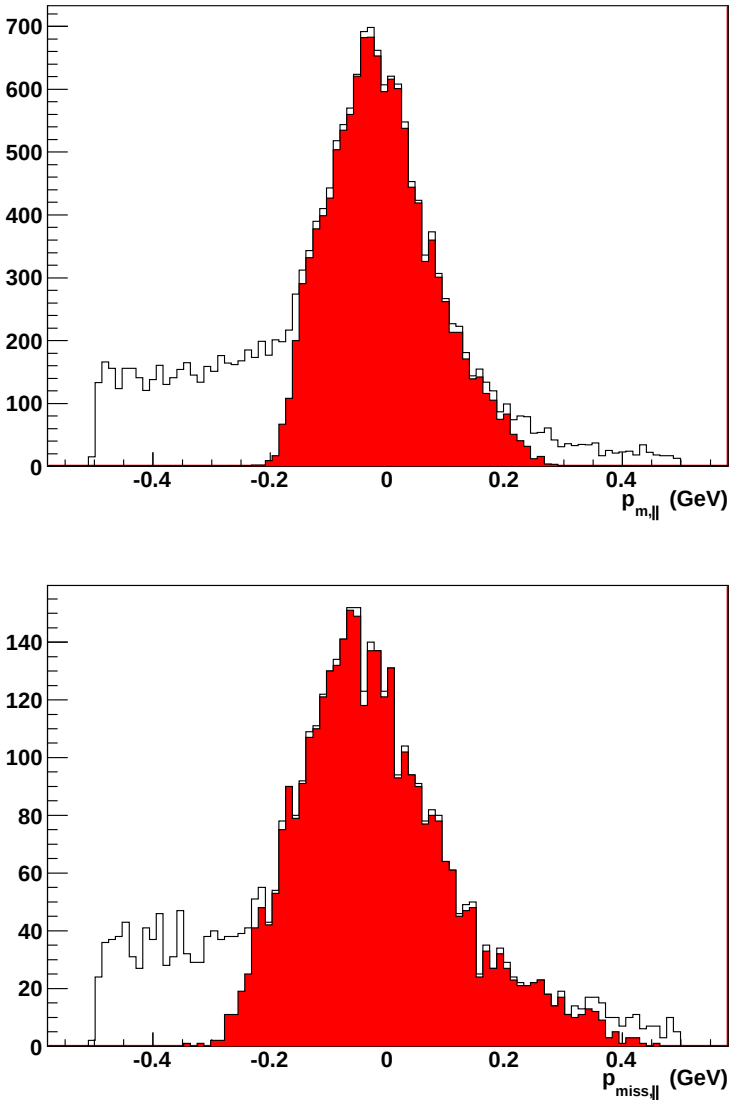

FIG. 6.1: **Missing Parallel Momentum with Time of Flight Cuts.** The missing parallel momentum histogram in white. The red histogram is also the missing parallel momentum, but with a cut on time-of-flight (-1 ns $<$ time-of-flight $<$ 1 ns). Top plot is for $Q^2 = 1.7$ GeV^2, lower plot is for $Q^2 = 2.5$ GeV^2.

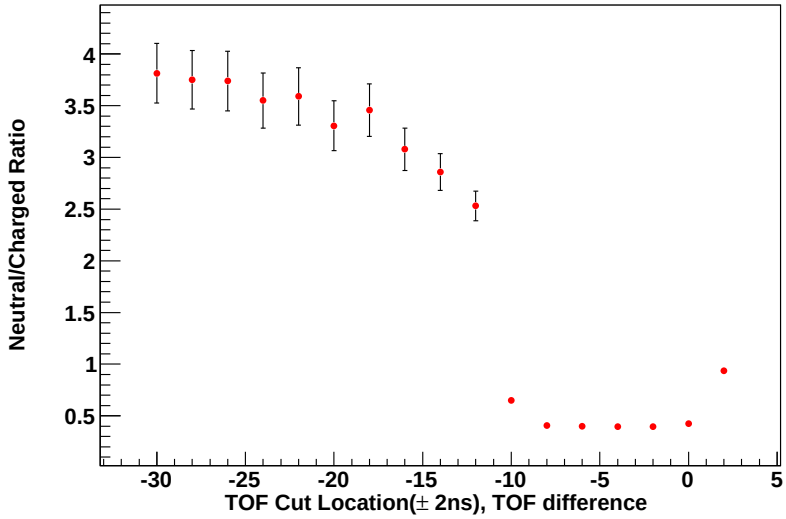

FIG. 6.2: **Charge Ratio v. Time of Flight.** The neutral/charged ratio varies as a function of time of flight, but is constant in a region far from the majority of scattering events (-30 to -20 ns).

The time shift must be large enough to be free of the effects of scattering events, but should be in a region where the background exists and is fairly constant. The shift used for all kinematics in this experiment was 30 ns. Fig. 6.2 shows that the neutral/charged ratio is consistent in this region, indicating that it is free of scattering events. The number of events in this region is consistent with the number of events closer to the good time-of-flight region.

Background Charge Identification

Recall that charge identification in the neutron detector for this experiment is determined by the use of a thin veto layer. If there is a signal from the veto layer in good agreement with the time and position of a hit in the neutron detector, then that event is determined to be from a charged event. This method of determining charge means that charged and uncharged events in the background sample must be treated differently.

The goal of this analysis is to subtract the number of events from our neutral sample

that are there as the result of a neutral background. Since the charges of the events are determined using timing information, a shift in the time-of-flight may change the efficiency of determining the charge. In fact, there are two extreme, but ultimately unlikely scenarios. First, the veto could properly identify all events in the background as charged or uncharged. In this case, the number of neutral events to subtract is the number calculated by shifting the time-of-flight. The second case is that none of the events are properly identified. The true uncertainty must therefore be somewhere in between. Following [67], the correct number of neutral events, $\Sigma^{\rm un}_{\rm back}$ from the background sample is:

$$\Sigma^{\rm un}_{\rm back} = \frac{N^{\rm un}_{\rm back}}{2} \pm \langle N^{\rm un}_{\rm back} \rangle, \tag{6.1}$$

where $\langle N^{\rm un}_{\rm back} \rangle$ is the root mean square value of a flat distribution from $-\frac{N}{2}$ (no neutral background) to $\frac{N}{2}$ (background is as measured). If this is normalized to 1, the RMS value can be written:

$$\langle N^{\rm un}_{\rm back} \rangle_{\rm RMS} = \left(\int_{-\frac{N}{2}}^{\frac{N}{2}} \frac{x^2}{N} dx \right)^{1/2} = \frac{N}{\sqrt{12}}. \tag{6.2}$$

While one extreme may seem more likely than the other, determining this from the data is tedious and does not result in a significant reduction of experimental uncertainty. Such information could be extracted from a sufficiently precise Monte Carlo simulation. However, as will be shown, the effect on the knowledge of G^n_E due to this uncertainty of the charge of the background is small and this method sets reasonable limits on this uncertainty.

If a background event is identified as charged, this means that there was a signal in the veto layer at the proper time and location. These events are charged background events. However, if the neutral events are misidentified, then the misidentified events must come from the charged events, so the number of background events can be written:

$$\Sigma^{\rm un}_{\rm back} = \frac{N^{\rm un}_{\rm back}}{2} \pm \frac{N^{\rm un}_{\rm back}}{\sqrt{12}} \tag{6.3}$$

$$\Sigma^{\rm ch}_{\rm back} = N^{\rm ch}_{\rm back} + \frac{N^{\rm un}_{\rm back}}{2} \pm \frac{N^{\rm un}_{\rm back}}{\sqrt{12}}. \tag{6.4}$$

Dilution

Recall the dilution factor due to background is simply:

$$D_{\rm back} = 1 - \frac{\Sigma_{\rm back}}{\Sigma}$$

And, for the uncharged background,

$$\Sigma^{\rm un}_{\rm back} = \frac{N^{\rm un}_{\rm back}}{2} \pm \frac{N^{\rm un}_{\rm back}}{\sqrt{12}}$$

The asymmetry associated with the background is simply:

$$\frac{\Delta_{\rm back}}{\Sigma} = \frac{N^{+}_{\rm back} - N^{-}_{\rm back}}{\Sigma}$$

Uncertainty

The uncertainty on the neutral background due to charge identification, $N^{\rm un}_{\rm back}/\sqrt{12}$, is combined with the statistical uncertainty ($\sqrt{N^{\rm un}_{\rm back}/2}$) to calculate the uncertainty for the background dilution factor.

$$\delta D_{\rm back} = \left(\frac{\delta\Sigma^2_{\rm back}}{\Sigma^2} + \frac{\Sigma^2_{\rm back}\left(\delta\Sigma\right)^2}{\Sigma^4} \right)^{1/2} = \left(\frac{N^{\rm un}_{\rm back}}{2\Sigma^2} + \frac{\left(N^{\rm un}_{\rm back}\right)^2}{12\Sigma^2} + \frac{\left(N^{\rm un}_{\rm back}\right)^2}{4\Sigma^3} \right)^{1/2} \quad (6.5)$$

6.2.2 Nitrogen Dilution and Proton Misidentification Uncertainty

Nitrogen Dilution Uncertainty

The nitrogen dilution factor is:

$$D = 1 - \frac{\rho_{\rm targ}({\rm N}_2)}{\rho_{\rm ref}({\rm N}_2)} \frac{N^{({\rm N}_2)}}{N^{({\rm N}_2+^3{\rm He})}} \frac{Q^{({\rm N}_2+^3{\rm He})}}{Q^{({\rm N}_2)}} \equiv 1 - \frac{C_{{\rm N}_2}}{C_{\rm He}}, \quad (6.6)$$

where $C_{{\rm N}_2}$ and $C_{\rm He}$ are the number of quasi-elastic events normalized by the product of the nitrogen density and accumulated charge for the nitrogen reference cell and the polarized ^{3}He cells, respectively.

The factors of accumulated charge and number of events can be calculated from the data. The density of nitrogen in the reference cell is determined by a pressure gauge and reference cell RTDs, and the density of nitrogen in the ^{3}He cell is calculated when the cell is filled. The number of events, $N^{(\mathrm{N}_2)}$ and $N^{(\mathrm{N}_2+^3\mathrm{He})}$ are background subtracted and therefore have the associated systematic error.

The uncertainty on the dilution factor is:

$$(\delta D_{\mathrm{N}_2})^2 = \frac{(\delta C_{\mathrm{N}2})^2 C_{\mathrm{He}}^2 + (\delta C_{\mathrm{He}})^2 C_{\mathrm{N}2}^2}{C_{\mathrm{He}}^4} \tag{6.7}$$

where C_{N_2} and C_{He} are defined in Eq. 6.6.

The uncertainty for these terms is

$$\delta C_{\mathrm{N}_2} = C_{\mathrm{N}_2}\sqrt{\left(\frac{\delta\rho_{\mathrm{ref}}(\mathrm{N}_2)}{\rho_{\mathrm{ref}}(\mathrm{N}_2)}\right)^2 + \left(\frac{\delta N^{(\mathrm{N}_2)}}{N^{(\mathrm{N}_2)}}\right)^2 + \left(\frac{\delta Q^{(\mathrm{N}_2)}}{Q^{(\mathrm{N}_2)}}\right)^2} \tag{6.8}$$

$$\delta C_{\mathrm{He}} = C_{\mathrm{He}}\sqrt{\left(\frac{\delta\rho_{\mathrm{targ}}(\mathrm{N}_2)}{\rho_{\mathrm{targ}}(\mathrm{N}_2)}\right)^2 + \left(\frac{\delta N^{(\mathrm{N}_2+^3\mathrm{He})}}{N^{(\mathrm{N}_2+^3\mathrm{He})}}\right)^2 + \left(\frac{\delta Q^{(\mathrm{N}_2+^3\mathrm{He})}}{Q^{(\mathrm{N}_2+^3\mathrm{He})}}\right)^2} \tag{6.9}$$

Proton Misidentification Uncertainty

The expression for the proton dilution factor was given as Eq. 5.32:

$$D_{p/n} = 1 - \frac{R_{\mathrm{H}}(R_{\mathrm{N}} - R_{^3\mathrm{He}})}{\frac{p}{n}R_{\mathrm{N}}(R_{^3\mathrm{He}} - R_{\mathrm{H}}) - R_{^3\mathrm{He}}R_{\mathrm{N}} + R_{^3\mathrm{He}}R_{\mathrm{H}}}$$

Following [67], the uncertainty on this factor is:

$$\begin{aligned}\delta D_{p/n} = \Bigg[&\left(\frac{\frac{p}{n}R_{\mathrm{H}}(R_{^3\mathrm{He}} - R_{\mathrm{N}})\delta R_{\mathrm{H}}}{R_{^3\mathrm{He}}(R_{\mathrm{N}} - R_{\mathrm{H}})^2(\frac{p}{n} - 1)}\right)^2 + \left(\frac{\frac{p}{n}R_{\mathrm{N}}R_{\mathrm{H}}\delta R_{^3\mathrm{He}}}{(\frac{p}{n} - 1)R_{^3\mathrm{He}}^2(R_{\mathrm{N}} - R_{\mathrm{H}})}\right)^2 \\ &+ \left(\frac{\frac{p}{n}(R_{^3\mathrm{He}} - R_{\mathrm{H}})\delta R_{\mathrm{N}}}{(\frac{p}{n} - 1)(R_{\mathrm{N}} - R_{\mathrm{H}})^2}\right)^2 + \left(\frac{(R_{^3\mathrm{He}} - R_{\mathrm{H}})\delta\frac{p}{n}}{(\frac{p}{n} - 1)^2(R_{\mathrm{N}} - R_{\mathrm{H}})}\right)^2\Bigg]^{1/2}\end{aligned} \tag{6.10}$$

6.2.3 Other Contributions to Uncertainty

Final State Interactions

The other major dilution is due to final state interactions, discussed in section 5.8. At this time, a calculation has been made, but the uncertainty on the final results has not

been agreed upon by the collaboration. For this analysis, $\delta D_{\rm FSI} = 0.05$ was used.

Inelastic Contribution

For the kinematics studied in this document, the contribution from inelastic events is very small. Monte Carlo estimates indicate that they contribute at the 1.5% level [116] to the overall dilution factor. This is not the case for measurements at higher Q^2 using the same experimental procedure. In that case, the contribution to the dilution is 3-10% [116].

6.3 Error Propagation

This experiment is primarily a counting experiment. Once proper cuts are applied, the number of neutral events detected from one electron helicity state and the number from the other state are compared. If these events are random at some fixed rate, they should form a Poisson distribution. A Poisson distribution with a mean number of counts, N, has a variance $\sigma^2 = N$. The statistical uncertainty on each bin is therefore $\delta N = \sqrt{N}$.

For a given asymmetry of uncorrelated counts,

$$A = \frac{N^+ - N^-}{N^+ + N^-},$$

the uncertainty on the asymmetry can be written:

$$\delta A = \sqrt{\frac{4N^+N^-}{(N^+ + N^-)^3}} = \sqrt{\frac{1 - A^2}{N}}.$$

Thus, for small asymmetries, $\delta A \propto 1/\sqrt{N}$.

The statistical uncertainty is completely contained in the raw asymmetry. To propagate this to the physical asymmetry, the proper dilution factors are applied,

$$\sigma_{\rm stat} = \frac{\delta A_{\rm raw}}{P_e P_n D_{\rm back} D_{\rm N_2} D_p D_{\rm FSI}}. \tag{6.11}$$

Variable	Value	Uncertainty	Relative Uncertainty
Q^2	1.70 (GeV^2)		
D_{N_2}	0.960	0.008	0.5%
$P_{^3\mathrm{He}}$	0.485	0.02	4.4%
P_e	0.853	0.026	3%
$D_{\mathrm{background}}$	0.925	0.02	2.2%
$D_{p/n}$	0.778	0.014	1.8%
$D_{\mathrm{FSI+P_n}}$	0.9025	0.05	5.3%
G_M^n [46]	-0.1656	0.022	1.7%

TABLE 6.3: **Extraction Factors for $Q^2 = 1.7\ \mathrm{GeV}^2$.** The required dilution factors and theoretical inputs required to extract G_E^n at $Q^2 = 1.7\ \mathrm{GeV}^2$.

The systematic uncertainty is:

$$\begin{aligned}\delta A_{\mathrm{phys}} &= \left(\frac{\delta A_{\mathrm{raw}}^2 + \delta\left(\frac{\Delta_p}{\Sigma}\right)^2}{\left(P_e P_n D_{\mathrm{back}} D_{\mathrm{N}_2} D_p D_{\mathrm{FSI}}\right)^2} + A_{\mathrm{phys}}^2 \left(\left[\frac{\delta P_e}{P_e}\right]^2 + \left[\frac{\delta P_n}{P_n}\right]^2 \right.\right. \\ &+ \left.\left. \left[\frac{\delta D_{\mathrm{N}_2}}{D_{\mathrm{N}_2}}\right]^2 + \left[\frac{\delta D_p}{D_p}\right]^2 + \left[\frac{\delta D_{\mathrm{FSI}}}{D_{\mathrm{FSI}}}\right]^2 \right) + (\delta_{\mathrm{back}})^2 \right)^{1/2}, \end{aligned} \tag{6.12}$$

where δ_{back} is the correlated uncertainty, written as:

$$\begin{aligned}\delta_{\mathrm{back}} &= \left[\left(\frac{A_{\mathrm{phys}}}{D_{\mathrm{back}}} - \frac{1}{P_e P_n D_{\mathrm{back}} D_{\mathrm{N}_2} D_p D_{\mathrm{FSI}}} \right)^2 \left(\frac{\delta N_{\mathrm{back}}^+}{2\Sigma} \right)^2 \right. \\ &+ \left(\frac{A_{\mathrm{phys}}}{D_{\mathrm{back}}} - \frac{1}{P_e P_n D_{\mathrm{back}} D_{\mathrm{N}_2} D_p D_{\mathrm{FSI}}} \right)^2 \left(\frac{\delta N_{\mathrm{back}}^-}{2\Sigma} \right)^2 \\ &+ \left. \left(\left(\frac{A_{\mathrm{phys}}\,(1 - D_{\mathrm{back}})}{D_{\mathrm{back}}} - \frac{\Delta_{\mathrm{back}}}{\Sigma} \frac{1}{D_{\mathrm{back}}} - \frac{1}{P_e P_n D_{\mathrm{back}} D_{\mathrm{N}_2} D_p D_{\mathrm{FSI}}} \right) \frac{1}{\sqrt{12}} \right)^2 \right]^{1/2} \end{aligned} \tag{6.13}$$

6.4 Results

The results of the calculations of the dilution factors and their relative uncetrainties can be found in Tables 6.3 and 6.4.

Variable	Value	Uncertainty	Relative Uncertainty
Q^2	$2.50\ (\mathrm{GeV}^2)$		
D_{N_2}	0.939	0.008	0.9%
$P_{^3\mathrm{He}}$	0.462	0.02	4.4%
P_e	0.848	0.025	3%
$D_{\mathrm{background}}$	0.938	0.018	1.9%
$D_{p/n}$	0.756	0.014	1.9%
$D_{\mathrm{FSI+P_n}}$	0.9229	0.05	5.4%
G_M^n [46]	-0.0961	0.0022	2.3%

TABLE 6.4: **Extraction Factors for $Q^2 = 2.5\ \mathrm{GeV}^2$.** The required dilution factors and theoretical inputs required to extract G_E^n at $Q^2 = 2.5\ \mathrm{GeV}^2$.

$Q^2(\mathrm{GeV}^2)$	A_{raw}	A_{phys}	N_{neutral}
1.70	-0.05263 ± 0.0028	-0.2039 ± 0.00295	118355
2.50	-0.04886 ± 0.0053	-0.2097 ± 0.00552	35122

TABLE 6.5: **Asymmetries and Statistical Errors.** Measured asymmetries presented with uncertainty from counting.

Once the factors required are calculated, the ratio $\Lambda = G_E^N/G_M^n$ is extracted from the physical asymmetry using the extraction outlined in Sec. 5.9.1:

$$A_{\mathrm{phys}} = \bar{T}_0 + \bar{T}_1\Lambda + \bar{T}_2\Lambda^2 + \bar{T}_3\Lambda^3 + \bar{T}_4\Lambda^4 + \bar{T}_5\Lambda^5.$$

The uncertainty in Λ is contained in A_{phys}, and is extracted by:

$$\delta\Lambda = \frac{\delta A_{\mathrm{phys}}}{\left|\sum_{i=n}^{5} n\bar{T}_n\Lambda^{n-1}\right|}. \tag{6.14}$$

Finally, the uncertainty on the neutron form factor comes from the uncertainty in Λ and the uncertainty on G_M^n, obtained at our value of Q^2 from the recent precision measurements at Jefferson Lab [46]:

$$\delta G_E^n = \sqrt{(\delta G_M^n\Lambda)^2 + (G_M^n\delta\Lambda)^2}. \tag{6.15}$$

Q^2(GeV^2)	G_E^n	(stat)	(sys)
1.70	0.0242	0.0020	0.0061
2.50	0.0247	0.0029	0.0031
3.41	0.0156	0.0020	0.0015

TABLE 6.6: **The Electric Form Factor of the Neutron.** The electric form factor of the neutron at three values of momentum transfer. The $Q^2 = 3.41$ GeV^2 result is from Ref. [116].

6.4.1 Note on Preliminary Results

The results present in this dissertation should be considered preliminary. There are several additional analytical methods that will be applied to these data. First, a Monte Carlo simulation of the experiment has been written, primarily to gain a better understanding of the contribution of inelastic events to the final asymmetry. Preliminary results indicate that this is a relatively small effect (negligible for $Q^2 = 1.7$ GeV^2 and approximately 2.5% for $Q^2 = 2.5$ GeV^2)—well within the quoted uncertainty.

Additionally, a closer inspection of the pion events identified as electrons in the electron spectrometer has been performed (Ref. [116]), but not applied to the results in this document. The effect on the asymmetry is less than 1% for our kinematics.

6.5 Conclusion

A plot of new results for $G_E^n(Q^2)$ is shown in Fig. 6.3. In addition to the results of the analysis in this document, a preliminary point at $Q^2 = 3.4$ GeV^2 has been added. The analysis for this point was performed by another member of the collaboration [67].

The determination of G_E^n at $Q^2 = 1.7$ and 2.5 GeV^2 is in excellent agreement with Miller's constituent quark model [34]. Miller's SU(6) wavefunction differs from several other models in the calculation of the neutron's core radius. This region is only experimentally resolvable at higher values of momentum transfer.

Perturbative QCD predicts a scaling function, $F_2/F_1 \propto \ln^2(Q^2/\Lambda^2)/Q^2$ [30]. If

Version	a_G	b_G
Kelly [17]	1.70 ± 0.04	3.30 ± 0.32
E02-013	1.40 ± 0.08	1.89 ± 0.36

TABLE 6.7: **New Galster Parameters from Data.** By fitting existing data and the data from this work, a new set of coefficients for Eq. 2.45: $G_E^n = \frac{a_G \tau}{1+b_G \tau} G_D$ can be established.

this scaling function is normalized to the value of G_E^n measured at $Q^2 = 1.7\ \mathrm{GeV}^2$, the measured value of G_E^n at $Q^2 = 2.5\ \mathrm{GeV}^2$ appears to somewhat agree with this scaling. However, the higher $Q^2 = 3.41\ \mathrm{GeV}^2$ point [116] indicates that this is not the case at higher Q^2.

A continuation of Lomon's vector meson dominance fit to historical data [33] provides a value of G_E^n that is smaller than the measured value at $Q^2 = 2.5\ \mathrm{GeV}^2$; the difference is not statistically significant. This model is a fit to the data published before E02-013 began. While there is little predictive power to such a fit, it is remarkable that an extension of the fit is in good agreement with the data, without re-tuning the fit parameters.

A continuation of the Galster and Kelly parametrizations [113, 17] predicts a smaller G_E^n than measured at $Q^2 = 2.5\ \mathrm{GeV}^2$. Using the same modified dipole form, but including these data points, new modified dipole constants can be established. The fit is included in Fig. 6.3, and the new fitting parameters are included in Table 6.7.

Finally, using the method described by Ref. [17], an improved view of the neutron charge distribution can be seen. As the charge distribution moves from positive to negative, the new uncertainty on the location of the zero crossing is nearly half the old uncertainty. Figure 6.4 shows the new view of the charge density.

An experiment has been approved to run at Jefferson Lab to measure G_E^n at $Q^2 = 10\ \mathrm{GeV}^2$ with similar precision [120]. These experimental values will provide insight into the nuclear models at regions in momentum transfer where the predictions diverge.

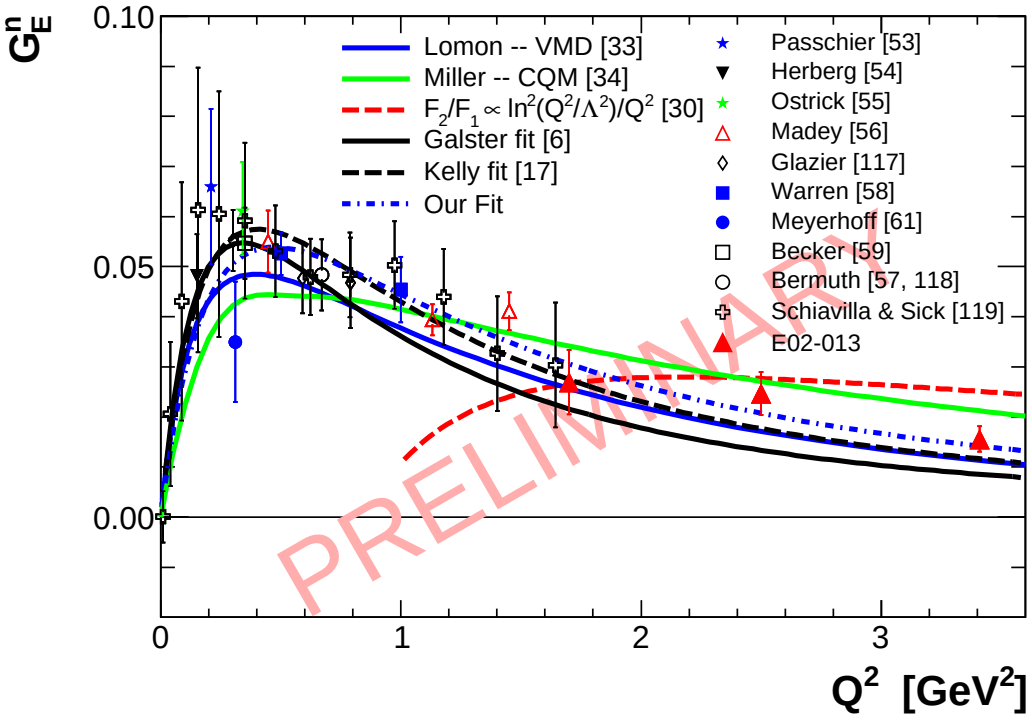

FIG. 6.3: G_E^n **at High** Q^2**.** The electric form factor of the neutron as a function of momentum transfer. Historical data and theoretical curves are included. The value of G_E^n at $Q^2 = 3.4$ GeV^2 from Ref. [116].

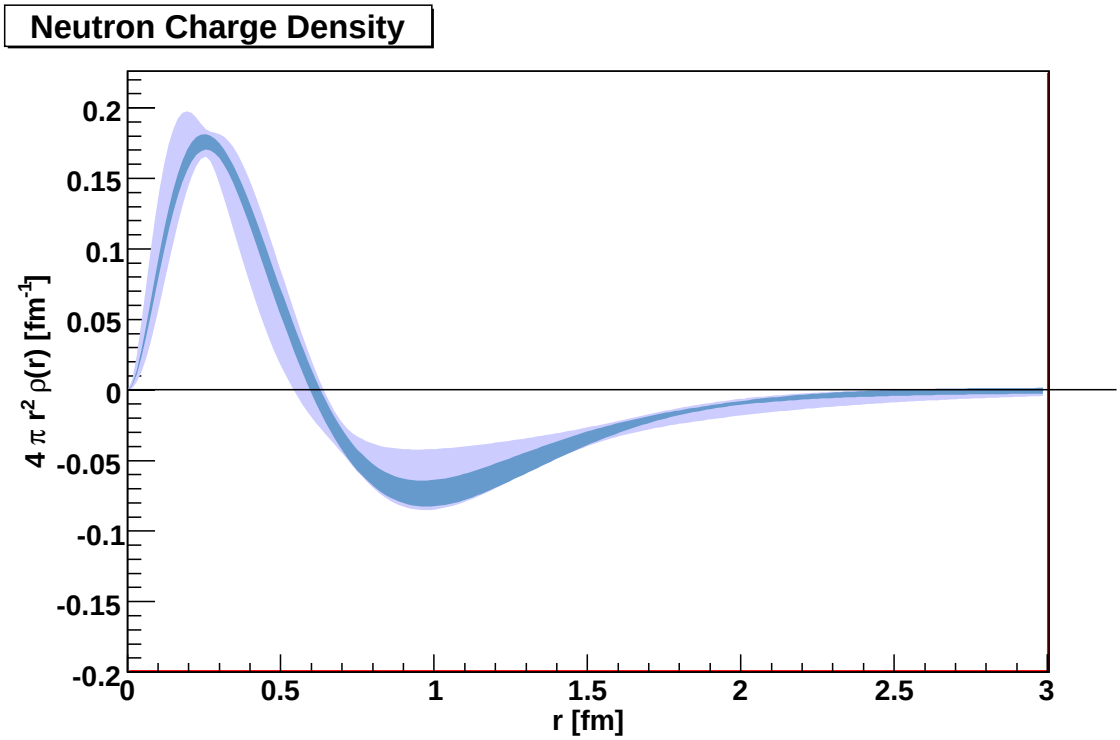

FIG. 6.4: **Neutron Charge Density.** The charge density of the neutron determined from the values of G_E^n. The outer band is the uncertainty before the analysis of E02-013 data. The inner band includes data taken in E02-013.

It will also serve to describe the neutron charge density with even greater precision.

BIBLIOGRAPHY

[1] Goeke, K., Polyakov, M., and Vanderhaghen, M., *Prog. Part. Nucl. Phys*, **47**, 401–515 (2001).

[2] Diehl, M., *Eur. Phys. J. C*, **25**, 223–232 (2002).

[3] Guidal, M., Polyakov, M. V., Radyushkin, A. V., and Vanderhaeghen, M., *Phys. Rev. D*, **72**, 054013 (2005).

[4] Diehl, M., Feldmann, T., Jakob, R., and Kroll, P., *Eur. Phys. J. C*, **39**, 1–39 (2005).

[5] Perdrisat, C., Punjabi, V., and Vanderhaeghen, M., *Prog. Part. Nucl. Phys.*, **59**, 694 – 764 (2007).

[6] Galster, S., et al., *Nucl. Phys. B*, **32**, 221–237 (1971).

[7] Blankleider, B., and Woloshyn, R. M., *Phys. Rev. C*, **29**, 538–552 (1984).

[8] Cates, G., McCormick, K., Reitz, B., and Wojtsekhowski, B., Jefferson lab experiment 02-013 (2002), URL `http://hallaweb.jlab.org/experiment/E02-013/`.

[9] Walker, T. G., and Happer, W., *Rev. Mod. Phys.*, **69**, 629–642 (1997).

[10] Baranga, A. B.-A., Appelt, S., Romalis, M. V., Erikson, C., Young, A., G.D.Cates, and Happer, W., *Phys. Rev. Lett.*, **80**, 2801–2804 (1998).

[11] Happer, W., *Rev. Mod. Phys.*, **44**, 169–249 (1972).

[12] Babcock, E., Nelson, I., Kadlecek, S., Dreihuys, B., Anderson, L., Hersman, F., and Walker, T. G., *Phys. Rev. Lett.*, **91**, 123003 (2003).

[13] Singh, J., et al., "New Directions in Spin-Exchange Optical Pumping in Polarized ^{3}He Targets", in *GDH 2004 Proceedings of the Third International Symposium on the Gerasimov-Drell-Hearn Sum Rule and Its Extenstions*, edited by S. Kuhn and J.-P. Chen, World Scientific Publishing Co., 2005, pp. 196–200.

[14] Hansen, O., ROOT/C++ Analyzer for Hall A (2009), URL `http://hallaweb.jlab.org/root/index.html`.

[15] Frisch, R., and Stern, O., *Zeits. f. Physik*, **85** (1933).

[16] Halzen, F., and Martin, A. D., *Quarks & Leptons: An Introductory Course in Modern Particle Physics*, John Wiley & Sons, Inc., 1984.

[17] Kelly, J. J., *Phys. Rev. C*, **66**, 065203 (2002).

[18] Kelly, J. J., *Phys. Rev. C*, **70**, 068202 (2004).

[19] Mitra, A. N., and Kumari, I., *Phys. Rev. D*, **15**, 261–266 (1977).

[20] Ji, X., *Phys. Rev. Lett.*, **78**, 610–613 (1997).

[21] Gourdin, M., *Nouvo Cimento*, **33**, 533 (1963).

[22] Lomon, E., and Feshbach, H., *Rev. Mod. Phys.*, **39**, 611–621 (1967).

[23] Akhiezer, A. I., Rozentswieg, L. N., and Shmushkevich, I., *Sov. Phys. JETP*, **6**, 588 (1958).

[24] Akhiezer, A. I., and Rekalo, M., *Sov. Phys. Dokl.*, **13**, 572 (1968).

[25] Donnelly, T. W., and Raskin, A. S., *Ann. Phys.*, **169**, 247 – 351 (1986).

[26] Raskin, A. S., and Donnelly, T. W., *Ann. Phys.*, **191**, 78 – 142 (1989).

[27] Bhaduri, R. K., *Models of the Nucleon*, Addison-Wesley, 1988.

[28] Albrecht, W., Behrend, H. J., Brasse, F. W., Flauger, W., Hultschig, H., and Steffen, K. G., *Phys. Rev. Lett.*, **17**, 1192–1195 (1966).

[29] Friedrich, J., and Walcher, T., *Eur. Phys. J. A*, **17**, 607–623 (2003).

[30] Belitsky, A. V., Ji, X., and Yuan, F., *Phys. Rev. Lett.*, **91**, 092003 (2003).

[31] Jones, M. K., et al., *Phys. Rev. Lett.*, **84**, 1398–1402 (2000).

[32] Gayou, O., et al., *Phys. Rev. Lett.*, **88**, 092301 (2002).

[33] Lomon, E. L., *Phys. Rev. C*, **66**, 045501 (2002).

[34] Miller, G. A., *Phys. Rev. C*, **66**, 032201 (2002).

[35] Borkowski, F., et al., *Nucl. Phys. B*, **93**, 461 – 478 (1975).

[36] Sill, A. F., et al., *Phys. Rev. D*, **48**, 29–55 (1993).

[37] Bosted, P. E., et al., *Phys. Rev. C*, **42**, 38–64 (1990).

[38] Walker, R. C., et al., *Phys. Rev. D*, **49**, 5671–5689 (1994).

[39] Andivahis, L., et al., *Phys. Rev. D*, **50**, 5491–5517 (1994).

[40] Rock, S., et al., *Phys. Rev. D*, **46**, 24–44 (1992).

[41] Lung, A., et al., *Phys. Rev. Lett.*, **70**, 718–721 (1993).

[42] Anklin, H., et al., *Phys. Lett. B*, **428**, 248 – 253 (1998).

[43] Kubon, G., et al., *Phys. Lett. B*, **524**, 26 – 32 (2002).

[44] Xu, W., et al., *Phys. Rev. Lett.*, **85**, 2900–2904 (2000).

[45] Xu, W., et al., *Phys. Rev. C*, **67**, 012201 (2003).

[46] Lachniet, J., et al., *Phys. Rev. Lett.*, **102**, 192001 (2009).

[47] Milbrath, B. D., et al., *Phys. Rev. Lett.*, **82**, 2221 (1999).

[48] Punjabi, V., et al., *Phys. Rev. C*, **71**, 055202 (2005).

[49] Dieterich, S., et al., *Phys. Lett. B*, **500**, 47 – 52 (2001).

[50] Arrington, J., et al., A measurement of two-photon exchange in unpolarized elastic electron-proton scattering. (2005), URL `https://hallcweb.jlab.org/experiments/rosen07/`.

[51] Christy, M. E., et al., *Phys. Rev. C*, **70**, 015206 (2004).

[52] Qattan, I. A., et al., *Phys. Rev. Lett.*, **94**, 142301 (2005).

[53] Passchier, I., et al., *Phys. Rev. Lett.*, **82**, 4988–4991 (1999).

[54] Herberg, C., et al., *Eur. Phys. J. A*, **5**, 131–135 (1999).

[55] Ostrick, M., et al., *Phys. Rev. Lett.*, **83**, 276–279 (1999).

[56] Madey, R., et al., *Phys. Rev. Lett.*, **91**, 122002 (2003).

[57] Rohe, D., et al., *Phys. Rev. Lett.*, **83**, 4257–4260 (1999).

[58] Warren, G., et al., *Phys. Rev. Lett.*, **92**, 042301 (2004).

[59] Becker, J., et al., *Eur. Phys. J. A*, **6**, 329–344 (1999).

[60] Zhu, H., et al., *Phys. Rev. Lett.*, **87**, 081801 (2001).

[61] Meyerhoff, M., et al., *Phys. Lett. B*, **327**, 201 – 207 (1994).

[62] Burkardt, M., *Int. J. Mod. Phys. A*, **18**, 173–207 (2003).

[63] Carlson, C. E., and Vanderhaeghen, M., *Physical Review Letters*, **100**, 032004 (2008).

[64] Miller, G. A., *Physical Review Letters*, **99**, 112001 (2007).

[65] Miller, G. A., *Phys. Rev. C*, **80**, 045210 (2009).

[66] Wojtsekhowski, B., "Prospect for Measuring G_E^n at High Momentum Transfer", in *Exclusive Processes at High Momentum Transfer*, edited by A. Radyushkin and P. Stoler, 2002.

[67] Riordan, S., *Measurements of the Electric Form Factor of the Neutron at Q^2 = 1.7 and 3.5 GeV*^{2}, Ph.D. thesis, Carnegie Mellon University (2008).

[68] Leeman, C. W., Douglas, D. R., and Krafft, G. A., *Ann. Rev. Nucl. Part. Sci.*, **51**, 413–450 (2001).

[69] Armstrong, D. S., et al., *Phys. Rev. Lett.*, **95**, 092001 (2005).

[70] Craver, B., Beam position calibration for G_E^n, Tech. rep., University of Virginia (2008), `http://www.jlab.org/~bcraver/docs/pdf/beam_cal.pdf`.

[71] Nanda, S., and Camsonne, A., Compton results (2009), `http://hallaweb.jlab.org/experiment/E02-013/wiki/tiki-index.php?page=Compton+Measurements`.

[72] Solvignon, P., *Measurement of the ^{3}He Spin Structure Functions in the Resonance Region: A test of Quark-Hadron Duality on the Neutron*, Ph.D. thesis, Temple University (2006).

[73] de Lange, D. J. J., Steijger, J. J. M., de Vries, H., Anghinolfi, M., Taiuti, M., Higinbotham, D. W., Norum, B. E., and Konstantinov, E., *Nucl. Instr. and Meth. A*, **406**, 182 – 194 (1998).

[74] Chudakov, E., G_E^n geometry and surveys (2006), http://hallaweb.jlab.org/experiment/E02-013/surveys.html.

[75] Ngo, T., Neutron arm geometry (2009), http://www.jlab.org/~ngo/ND_Geometry.pdf.

[76] Amsler, C., et al., *Physics Letters B*, **667**, 1 – 6 (2008), review of Particle Physics.

[77] Friar, J. L., Tomusiak, E. L., Gibson, B. F., and Payne, G. L., *Phys. Rev. C*, **24**, 677–683 (1981).

[78] Anthony, P. L., et al., *Phys. Rev. D*, **54**, 6620–6650 (1996).

[79] Abe, K., et al., *Physics Letters B*, **404**, 377 – 382 (1997).

[80] Solvignon, P., et al., *Phys. Rev. Lett.*, **101**, 182502 (2008).

[81] Sulkosky, V., *The Spin Structure of (^{3}He) at Low Q^2: A Measurement of the Generalized GDH Integrand*, Ph.D. thesis, The College of William & Mary (2007).

[82] Kramer, K., et al., *Phys. Rev. Lett.*, **95**, 142002 (2005).

[83] Zheng, X., et al., *Phys. Rev. C*, **70**, 065207 (2004).

[84] Anderson, B., et al., *Phys. Rev. C*, **75**, 034003 (2007).

[85] P.Chen, J., Jiang, X., Peng, J. C., et al., Measurement of single target-spin asymmetry in semi-inclusive $n^{\uparrow}(e, e'\pi^-)$ reaction on a transversely polarized ^{3}He target (2006), URL http://hallaweb.jlab.org/experiment/transversity/.

[86] Cisbani, E., Gao, H., Jiang, X., et al., Target single spin asymmetry in semi-inclusive deep-inelastic $(e, e'\pi^-)$ reaction on a transversely polarized ^{3}He target (2006), URL http://hallaweb.jlab.org/experiment/transversity/.

[87] Gilad, S., Higibotham, D., Korsch, W., Sirca, S., Norum, B., et al., Measurement of the A_x and A_z asymmetries in the quasi-elastic $^3\overrightarrow{\mathrm{He}}(\overrightarrow{e}, e'd)$ (2005), URL `http://hallaweb.jlab.org/experiment/E05-102/e05-102/`.

[88] Averett, T., Chen, J. P., Jiang, X., et al., Measurement of the target single-spin asymmetry in quasi-elastic $^3\mathrm{He}\uparrow(e, e'd)$ (2005), URL `http://hallaweb.jlab.org/experiment/E05-102/e05-015/`.

[89] Averett, T., Holmstrom, T., Jiang, X., et al., Target normal single-spin asymmetry in inclusive dis $n^{\uparrow}(e, e')$ with a polarized $^3\mathrm{He}$ target (2007), URL `http://www.jlab.org/exp_prog/proposals/07/PR-07-013.pdf`.

[90] Averett, T., Higinbotham, D., Sulkosky, V., et al., Measurement of the target single-spin asymmetry, A_y, in the quasi-elastic $^3He \uparrow (e, e'n)$ reaction (2008), URL `http://hallaweb.jlab.org/experiment/E05-102/e08-005/`.

[91] Choi, S., Jiang, X., Meziani, Z. E., Sawatzky, B., et al., Measurement of the neutron d_2: Towards the electric χ_E and magnetic χ_M color polarizabilities (2006), URL `http://www.jlab.org/exp_prog/proposals/06/PR06-014.pdf`.

[92] Hrycyshyn, E. S., and Krause, L., *Can. J. Phys.*, **48**, 2761–2768 (1970).

[93] Romalis, M. V., *Laser Polarized ^{3}He Target Used for a Precision Measurement of the Neutron Spin Structure*, Ph.D. thesis, Princeton University (1997).

[94] Bouchiat, M. A., Carver, T. R., and Varnum, C. M., *Phys. Rev. Lett.*, **5**, 373–375 (1960).

[95] Walker, T. G., *Phys. Rev. A*, **40**, 4959–4964 (1989).

[96] Herman, R. M., *Phys. Rev.*, **137**, A1062–A1065 (1965).

[97] Walker, T. G., Bonin, K., and Happer, W., *Phys. Rev. A*, **35**, 3749–3752 (1987).

[98] Happer, W., Cates, G., Romalis, M., and Erikson, C., U.S. Patent No. 6,318,092 (2001).

[99] Baranga, A. B.-A., Appelt, S., Erickson, C., Young, A., and Happer, W., *Phys. Rev. A*, **58**, 2282–2294 (1998).

[100] Kramer, K., *A Search for Higher Twist Effects in the Neutron Spin Structure Function* $g_2^n(x, Q^2)$, Ph.D. thesis, The College of William and Mary (2003).

[101] Abragam, A., *Principles of Nuclear Magnetism*, Oxford University Press, 1961.

[102] Romalis, M. V., and Cates, G. D., *Phys. Rev. A*, **58**, 3004–3011 (1998).

[103] Babcock, E., Nelson, I. A., Kadlecek, S., and Walker, T. G., *Phys. Rev. A*, **71**, 013414 (2005).

[104] Schaefer, S. R., Cates, G. D., Chien, T.-R., Gonatas, D., Happer, W., and Walker, T. G., *Phys. Rev. A*, **39**, 5613–5623 (1989).

[105] Zheng, X., *Precision Measurement fo Neutron Spin Asymmetry* A_1^n *at Large* x_{bj} *Using CEBAF at 5.7 GeV*, Ph.D. thesis, Massachusetts Institute of Technology (2002).

[106] Fuchs, S., and Averett, T., Results of beam window safety research, Tech. rep., The College of William & Mary (2005), URL `http://pol3he_daq.physics.wm.edu/~pol3he/GEN/Beamline.php`.

[107] Kelleher, A., Results of beamwindow safety research, Tech. rep., The College of William & Mary (2003), URL `http://pol3he_daq.physics.wm.edu/~pol3he/GEN/Beamline.php`.

[108] ROOT (2009), URL `http://root.cern.ch`.

[109] Forest, J. L., Pandharipande, V. R., Pieper, S. C., Wiringa, R. B., Schiavilla, R., and Arriaga, A., *Phys. Rev. C*, **54**, 646–667 (1996).

[110] Schiavilla, R., Pandharipande, V. R., and Wiringa, R. B., *Nuclear Physics A*, **449**, 219–242 (1986).

[111] Sargsian, M., *Int. J. Mod. Phys. E*, **10**, 405–457 (2001).

[112] Glauber, R., *Phys. Rev.*, **100**, 242–248 (1955).

[113] Glauber, R., "High-Energy Collision Theory", in *Lectures in Theoretical Physics*, edited by W. Brittin and L. Dunham, Wiley Interscience, 1959, vol. 1, p. 315.

[114] Sargsian, M., Private Communication, (Contact: `sargsian@fiu.edu`) (2009).

[115] Franklin, G. B., GEn asymmetry corrections for finite angular acceptance, Tech. rep., Carnegie Mellon University (2006).

[116] Riordan, S., Private Communication, (Contact: `riordan@jlab.org`) (2009).

[117] Glazier, D. I., et al., *Eur. Phys. J. A*, **24**, 101–109 (2005).

[118] Bermuth, J., et al., *Phys. Lett. B*, **564**, 199 – 204 (2003).

[119] Schiavilla, R., and Sick, I., *Phys. Rev. C*, **64**, 041002 (2001).

[120] Cates, G., Riordan, S., Wojtsekhowski, B., et al., Measurement of the neutron electromagnetic form factor ratio G_E^n/G_M^n at high Q^2 (2009), URL `http://www.jlab.org/exp_prog/proposals/09/PR-09-016.pdf`.

VITA

Aidan Kelleher

Aidan Michael Kelleher was born on August 13, 1975 in Alexandria, Virginia. After kindergarten classes at nearby Woodley Hills Elementary School, he finished grade school and middle school at St. Mary's Elementary in Alexandria. In eighth grade he was exposed to algebra and physical science for the first time, and decided that was what he wanted to study. With this in mind, he attended high school at Bishop Ireton High School, also in Alexandria.

Although studying advanced placement Computer Science and Calculus, he decided to broaden his education and entered St. John's College in Annapolis, Maryland. All St. John's students study the same material, based on primary sources. The equivalent in terms of majors and minors is a double major in Philosophy and History of Math and Science and a double minor in Comparative Literature and Classical Studies.

His first job after St. John's was a direct mail advertising agency in Richmond, Virginia. He started as a creative assistant and soon progressed to list manager. While in Richmond, he read several popular books on quantum physics that remined him of his interest in physics. After long discussions with Prof. Marc Sher, he moved to Williamsburg and took the required undergraduate classes in physics to enter graduate school.

In August of 2002, he entered graduate school at the College of William & Mary. After receiving his Master's degree in December 2004, he started full-time research with Prof. Todd Averett. Upon completion of his doctorate he plans to pursue research full-

time as a post-doctoral associate with the Massachusetts Institute of Technology Laboratory for Nuclear Science.

A MEASUREMENT OF THE NEUTRON ELECTRIC FORM FACTOR AT VERY LARGE MOMENTUM TRANSFER USING POLARIZED ELECTRONS SCATTERING FROM A POLARIZED HELIUM-3 TARGET

ABSTRACT PAGE

Knowledge of the electric and magnetic elastic form factors of the nucleon is essential for an understanding of nucleon structure. Of the form factors, the electric form factor of the neutron has been measured over the smallest range in Q^2 and with the lowest precision. Jefferson Lab experiment 02-013 used a novel new polarized ^{3}He target to nearly double the range of momentum transfer in which the neutron form factor has been studied and to measure it with much higher precision. Polarized electrons were scattered off this target, and both the scattered electron and neutron were detected. G_E^n was measured to be $0.0242 \pm 0.0020(\mathrm{stat}) \pm 0.0061(\mathrm{sys})$ and $0.0247 \pm 0.0029(\mathrm{stat}) \pm 0.0031(\mathrm{sys})$ at $Q^2 = 1.7 \text{ and } 2.5\ \mathrm{GeV}^2$, respectively.

AIDAN M. KELLEHER

DEPARTMENT OF PHYSICS

THE COLLEGE OF WILLIAM AND MARY IN VIRGINIA

TODD D. AVERETT

PROFESSOR OF PHYSICS